UNIVERSIDADE FEDERAL DE SÃO CARLOS
CENTRO DE CIÊNCIAS EXATAS E TECNOLÓGICAS
PROGRAMA DE PÓS-GRADUAÇÃO EM FÍSICA

Transport phenomena in quasi-one-dimensional heterostructures

Mariama Rebello de Sousa Dias

Thesis presented to the Academic Faculty at Universidade Federal de São Carlos in partial fulfillment of the requirements for the Doctoral Degree in the Graduation Physics Course.

Advisor: Prof. Dr. Victor Lopez Richard
Co-adivisor: Prof. Dr. Sergio Ulloa

São Carlos, February 2014.
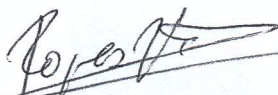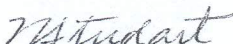
Mariama Rebello de Sousa Dias

Tese de doutorado submetida à Coordenação do Programa de Pós-Graduação em Física, da Universidade Federal de São Carlos, como requisito parcial para a obtenção do título de doutor em ciências.

Aprovado em: 21 de fevereiro de 2014
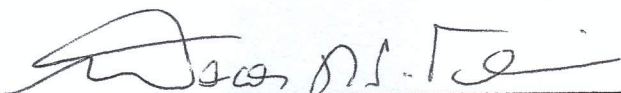
BANCA EXAMINADORA

Prof. Dr. Victor Lopez Richard (Orientador)
Universidade Federal de São Carlos - DF

Prof. Dr. Nelson Studart Filho
Universidade Federal de São Carlos - DF

Prof. Dr. Marcos Roberto da Silva Tavares
Universidade Federal do ABC

Prof. Dr. Yuri Pusep
Universidade de São Paulo

Prof. Dr. Paulo Sérgio Pizani
Universidade Federal de São Carlos - DF

CONTENTS

LIST OF FIGURES

LIST OF TABLES

ACKNOWLEDGMENT

ABSTRACT

The growth and characterization of semiconductor quasi-one-dimensional heterostructure systems have attracted increasing interest due to their potential technological application, like photo-detectors, optoelectronic devices and their promising features for quantum information processing and photonic applications. The goal of this thesis is the study of electronic and spin transport properties on quasi-one-dimensional semiconductor systems; specifically, homogenous nanowires (NWs), coupled NW's, twin-plane (TP) NWs, resonant tunneling diodes (RTDs), and quantum dot chains (QDCs). The $\mathbf{k} \cdot \mathbf{p}$ method, in particular the Luttinger Hamiltonian, was chosen to describe the effects of biaxial confinement and strain. This suggested a modulation of the ground state character that, complemented with the phonon dynamics provided by Molecular Dynamics (MD) simulations, allowed the description of the hole mobility modulation by either phonon emission or absorption.

Regarding the coupled NW's system, the electron and spin transport properties affected by a Rashba spin-orbit interaction (SOI) at the joined region were unveiled through the Transfer Matrix Method (TMM). Various configurations of gate voltages (V_g), applied on the wire structure, were considered. We were able to understand the modulation of the spin transport projected in the z-direction trough the combination of the SOI and the system dimensionalities. Likewise, the combination of SOI and applied V_g gave rise to a modulation of the polarization, when the measured spin is projected in the same direction where the Rashba SOI acts, the y-direction.

The transport properties of a DBS and the effect of a resistance in series was explored within the TMM to prove the nature of a bistability of the $I - V$ characteristics and its enhanced area with temperature provided by the experiment. The model indicates that increasing the resistente by decreasing the temperature, the bistable area enhances. The presence of an additional heterojunction induces a sheet charge at its interfaces. Under this configuration, the total voltage drop of the RTD changes and can be confirmed

experimentally.

The formation of the peculiar strain fields and their influence on the electronic structure and transport properties of a TP superlattice was systematically studied. Hence, the transport properties of both electrons and holes could be effectively tuned even in the case of Γ-electrons of zincblende systems, contrasting to the predicted transparency of Γ-electrons in heterolayered III-V semiconductor superlattices. Also, the transmission probability for holes at valence band could also be effectively modified by applying an external stress.

Finally, using molecular-beam-epitaxy and skillful strain engineering, systems of InGaAs QDCs were successfully synthesized by collaborators. The QDCs with different doping concentrations showed an anisotropic behavior of the conductance, measured along and across the QDCs, with temperature. The theoretical 1D hopping model developed found that the presence of 0D states shapes the anisotropic response of the conductance in this system.

Keywords: transport phenomena, spin-orbit interaction, $\mathbf{k} \cdot \mathbf{p}$ method, transfer matrix method, electron-phonon interaction, semiconductor nanowires, twin-plane nanowires, resonant tunneling diodes, quantum dot chains.

RESUMO

O crescimento e caracterização de sistemas de heteroestruturas semicondutoras quasi-unidimensionais têm atraído grande interesse devido à sua potencial de aplicação tecnológica, como foto-detectores, dispositivos opto-eletrônicos assim como seu para o processamento de informação quântica e aplicações em fotônica. O objetivo desta tese é o estudo das propriedades de transporte eletrônico e de spin em sistemas semicondutores quasi-unidimensionais, especificamente trataremos de nanofios (NWs) homogêneos, NWs acoplados, NWs do tipo plano-geminado (TP), diodos de tunelamento ressonante (RTD) e cadeias de pontos quânticos (QDCS). Escolhemos o método $\mathbf{k} \cdot \mathbf{p}$, particularmente o Hamiltoniano de Luttinger, para descrever os efeitos de confinamento e tensão biaxial. Este sugeriu uma modulação do caráter do estado fundamental que, complementada com a dinâmica fônons fornecidas pelas simulações da Dinâmica Molecular (MD), permitiu a descrição da modulação da mobilidade de buracos por emissão ou absorção de fônons.

Em relação ao sistema de NWs acoplado,estudamos, através do método da matriz de transferência (TMM), as propriedades de transporte de elétrons e spin sob a interação de spin-órbita (SOI) de Rashba, localizada na região de acoplamento entre fios. Foram consideradas várias configurações de tensões de *gate* (V_g) aplicadas nos fios. Desse modo, compreendemos a modulação do transporte de spin quando esse é projetado no direção-z através da combinação do SOI e das dimensionalidades do sistema. Da mesma forma, a combinação de SOI e da V_g aplicada deu origem a modulação da polarização, quando o spin medido é projetado na mesma direção em que o SOI de Rashba atua, a direção y.

Usando o TMM, exploramos as propriedades de transporte de um DBS e o efeito de uma resistência em série com o intuito de provar a natureza da biestabilidade das curvas características $I - V$ bem como o aumento de sua área com temperatura, resultados fornecidos por experimentos. O modelo indicou que aumentando da resistência pela diminuição sa temperatura aumenta a área biestável. A presença de uma hetero-junção adicional ao sistema induz uma densidade de carga nas suas interfaces. De acordo

com esta configuração, a queda de tensão total do RTDS muda, podendo ser confirmada experimentalmente.

A formação dos peculiares campos de deformação e sua influência sobre a estrutura eletrônicas e propriedades de transporte em superredes de TP foi estudada sistematicamente. Assim, as propriedades de transporte, de ambos os elétrons e buracos, pode ser sintonizada eficientemente, mesmo no caso de elétrons Γ em sistemas de blenda de zinco, contrastando com a prevista transparência de elétrons Γ em superredes de semicondutores III-V heteroestruturados. Além disso, constatamos que a probabilidade de transmissão para buracos da banda de valência também poderia ser efetivamente modificada através de uma tensão externa.

Por fim, colaboradores sintetizaram com sucesso sistemas de QDCs de InGaAs através da epitaxia de feixe molecular e engenharia de tensão. Um comportamento anisotrópico da condutância com a temperatura foi observado em QDCs com diferentes concentrações de dopagem, medida realizada ao longo e entre os QDCs. O modelo teórico 1D de *hopping* desenvolvido mostrou que a presença de estados 0D modela a resposta anisotrópica da condutância neste sistemas.

Palavras-chave: fenômenos de transporte, interação spin-órbita, método de matriz transferência, método $\mathbf{k} \cdot \mathbf{p}$, interação elétron-fônon, nanofios semicondutores, nanofios de planos-geminados, diodos de tunelamento ressonante, cadeias de pontos quânticos.

1. INTRODUCTION

In the last decade, the growth technics of quasi-one-dimensional semiconductor structures considerably improved. Such a development in the field allowed the appearance of a great variety of these systems. For example, using molecular-beam epitaxy and strain engineering, a unique system of aligned quantum dots, i.e., quantum dot chains, was successfully synthesized [1, 2] opening up new field of research while new physics is unveiled.

Also, just recently, the controlled synthesis of stacking fault heterostructures of III-V compound semiconductor nanowires (NWs) has been reported [3, 4]. Improvements in NW synthesis, including chemical technics, allow a thorough control of their shape, size, and composition [5, 6, 7, 8, 9]. All these advances led to the discovery of new phenomena, as well as to new outstanding applications in optically active devices [10], as building blocks for nanocircuits [11], electrically driven lasing [12], which can be used in telecommunications, for medical diagnostics and therapeutics [13], and information storage. Likewise, exploring all-electrical spin transport has motivated a search for new configurations of nanostructures [14, 15, 16, 17, 18] in order to make feasible spin-orbit quantum bit devices [19].

The technological advantage of NWs is related to the ability of engineering and controlling their quantum properties which can be achieved, for instance, through the modification of the NW geometry and strain fields, also theoretically predicted [20]. Simultaneously, the development of theoretical models allowed a better understanding of the physics of quasi-one-dimensional heterostructures. For instance, the plausibility of building inhomogeneous heterostructures of a single semiconductor material was long ago theoretically predicted when stacking faults and the creation of layered systems of semiconductor segments between twin-planes were simulated [21].

At the field frontier, the interest in hybrid semiconductor nanostructures based on NWs and heterostructured systems allowed foreseing new physicals phenomena. The prediction of Majorana fermions, "half-fermion" that is its own antiparticle, brought together two

fields in physics: condensed matter and elementary particles [22, 23]. The outstanding synthesis and fabrication techniques of these structures, as well as their reproducibility and capability of electrical modulation properties made possible the observation of this prediction. They also anticipate this kind of state of matter as a building block for quantum computation [24, 25].

The demand for solving challenging questions in this area and the plausibility of experimental testing of theoretical predictions allowed the definition of the objectives tackled in this thesis. That is the main motivation for this work to focus on a sequence of theoretical studies of transport phenomena in quasi-one-dimensional (1D) heterostructures in the quantum regime. The transport regime in semiconductor heterostructures is associated with the time and length scales of the particles in the system. For a semiconductor nanostructure, the de Broglie wavelength of a carrier is comparable with its size, $\mathbf{L}(L_x, L_y, L_z)$, and that is the reason why one should take in consideration quantum phenomena in the transport properties. The combination of both, a strong experimental, supported by collaborators, and theoretical expertise offered the possibility for a roadmap strategy starting from basic fundamental properties of quantum transport phenomena of these structures towards the realization and applications of nano-scale devices. In this way, by building this thesis we have transited throughout established fundamental properties, modeled processes of carrier transport in 1D devices, found optimal regimes to amplify desired responses, and developed new concepts. Some problems have an experimental interface that strengthened the impact of our theoretical endeavors for potential applications.

The thesis has been organized as follows. In Chapter 2 the model for the electronic structure calculations of two semiconductor systems, cylindrical and semi-cylindrical NWs is presented. The study that correlates transport behavior and structural properties, as geometry and composition, through the electronic structure of NWs, allows a better understanding of electromagnetic field and strain effects. [26, 9, 27]

The previous knowledge about the NWs morphological details is important for the electronic structure description and we have illustrated this by using the example of available data of InP NWs. These structures can be grown via the vapor-liquid-solid method in a CBE ("*Chemical Beam Epitaxy*") machine and the verification that the NWs are strained can be done through the Fourier transform analysis of scanning electron microscopy (SEM) and transmission electron microscopy (TEM). [9] The reported values

of the deformation are: $\epsilon_{\parallel} = -0.9\%$, biaxial strain, and $\epsilon_{zz} = 1.00\%$, strain along the axis of the wire. [26]

Given its versatility, the formalism chosen to calculate the electronic structure of these systems is based on the $\mathbf{k} \cdot \mathbf{p}$ method. This method is grounded on the idea that the influence of a periodic potential over an electron in a crystal lattice can be taken into account through the concept of effective mass. [28] The presence of a periodic crystalline potential makes the Bloch theorem valid which describes, in first approximation, the electron state as a charge carrier with effective mass m^*, differing from the free electron mass. This approach allows exploring the confinement effects, strain modulation, and elector-phonon interactions within the same theoretical framework.

The Chapter 3 describes the transport mechanisms in place within the systems under consideration: ballistic transport, quantum tunneling, and hopping. The ballistic transport regime is available when the sample dimensionality is much smaller than the electron mean free. In this regime, the conductance depends on the band structure and on the device geometry. According to Landauer, [29] the current is proportional to the transmission probability of an electron [30], related to the linear response of the conductance. A ballistic conductor has its transmission probability close to the unity value which could lead to an infinite current, not observed in experiments.

In turn, the Quantum Mechanics wave-like description of carriers provides conditions for the tunneling effect of an electron through potential barriers. This Quantum Mechanical effect made possible the discovery of the tunnel diode by L. Esaki [31], which gave rise to a revolution in electronics and many other theoretical fields. Our goal was to analyze the quantum tunneling impact in the carriers transport through 1D layered systems and describe how this can be tuned by external fields, strain and temperature.

A model based on hopping transport can also describe the temperature dependence of the carriers mobility through a system involving localized states. This approach is suitable for simulating charge transfer in quantum dot chains [32, 33, 34, 35, 36] and we have provided a description motivated by experimental evidences available for this kind of structure. This is a semiclassical theory determined by inelastic transitions of electrons from full states to neighboring empty states assisted by phonons.

Subsequently, specific problems are tackled. The knowledge of the valence band structure combined with Molecular Dynamic (MD) simulations, performed by the group of

Prof. Jose P. Rino at UFSCar, enabled the transport calculation of an homogeneous NW. Thus, Chapter 4 describes the effects of shape and temperature on the hole wavefunction and mobility taking into account the phonon occupation and strain effects. This choice was based on the fact that considerable efforts have been devoted to the description of carriers in the conduction band of NWs, [37, 38, 39, 40, 41, 42, 43] while similar endeavors are not so common for holes in the valence band. [44] As the mobility is inversely proportional to the carrier effective mass, one may naturally expect that considering carriers in the valence band may result in a drop in mobility when compared to the light electrons in the conduction band. This could certainly be the case for heavy-holes (HH) transport; however, light-holes (LH) under certain conditions may be promoted to be the top valence band by tuning structural parameters of NWs. [27] This atypical circumstance is the result of confinement effects and HH-LH mixing, affected as well by strain and the presence of surfaces. [9, 27] As one will see, this results in significant mobility enhancement for LH in suitable NWs. We can also take advantage of valence band mass anisotropy to attain resonant conditions that allow sharp variations of the hole mobility with external parameters, especially when the leading scattering process involve LO-phonons through the deformation potentials. [45] In order to provide realistic estimates of the expected mobility changes in the NWs of interest, we consider the effects of dimensionality reduction on the LO-phonon dispersion and lifetime, using MD simulations for different NWs size and at various temperatures. These latter effects were characterized by our collaborators and the results used by us as input parameters for the subsequent calculation of the hole-phonon interaction terms. Subsequently, we find that for certain widths, resonant behaviors are triggered that reduce the hole mobility and can be strongly affected by temperature and strain. Moreover, the mobility changes in a non-monotonic fashion according to the NW width, strain fields, and temperature.

The nature of processes that combine both electron and spin transport mechanisms was explored in Chapter 5. In particular, we report the spin transport properties of parallel NWs, in a directional "H-shape" coupler connected through a region of the same material but locally gated, as displayed in Fig. 1.1(a). The realization of a directional coupler in the early 90's gave rise, through proximity and tunneling effects,[46, 47] to the modulation of quantum transport in a phase-coherent system.[48] Also, the spin modulation in a single NW via spin-orbit interaction (SOI) has been proposed [49] and refined [50, 51, 52, 53, 54]
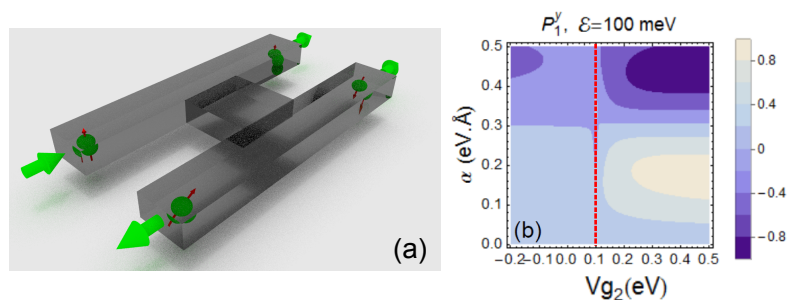
Fig. 1.1: (a) Scheme of the proposed system where we have two parallel nanowires connected in a middle region by the same material.(b) Polarization in the y-direction vs the SOI strength, α, and applied gate voltage on the bottom right wire, (Vg_2), for the top right wire (P_1^y) with incident energy from the top left wire of $\mathcal{E} = 100$ meV.

to achieve a spin-orbit quantum bit device. [19] Exploring all-electrical spin transport has motivated a search for new configurations of nanostructures [14, 15, 16, 17, 18]. Thus, exploring the properties of coupled NWs in order to unveiled the nature of electron and spin transport mechanisms, a spin-wave guide directional coupler appears as a promising device geometry.

Therefore, the application of a gate field in the connecting region generates a Rashba spin-orbit interaction, which breaks spin degeneracy. We find that, while being able to control the electronic flux through the different wires across the mixing region, as expected, it is also possible to electrically control the *spin flux* across the device whenever spin-polarized injection is considered. Moreover, we find that there is a net spin-polarized flux perpendicular to the current, which can be controlled by the gate potential in the mixing region, as well as by local gates at the NWs, as illustrated in Fig. 1.1(b). This overall control of charge and spin flux in a directional coupler appears promising for spintronics, as well as in hybrid devices combined with superconducting or magnetic materials.

Chapter 6 is devoted to the description of 1D transport through hetero-layered systems. The transfer matrix formalism will be applied to two different problems and the modulation of the transport response to structural factors and charge confinement will be analyzed. Describing the 1D transport in resonant tunneling diodes (RTDs) requires the use of some of the main concepts condensed within this thesis. Additionally, it has been demonstrated the relevance of such structures as sensors with characteristics such as high internal gain and aptitude for single photon detection. [55, 56, 57] The basic principle of these detectors is the local and sensitive variation of the electric field, caused by accumulated carriers at the intrinsic tunneling structure. [58, 59, 60] Effectively, the transmission

probability of majority carriers can be also altered by accumulation of photo-generated ones.

To exploit the RTDs full potential, the best working point has to be identified, which is a highly complex matter that correlates efficiency, carrier accumulation dynamics, and system gain. Recently, AlGaAs/GaAs based double barrier structure (DBS) with a nearby and lattice matched GaInNAs absorption layer was proposed for high sensitive photo detection at the telecommunication wavelength $\lambda = 1.30$ μm [61, 62]. These devices are the inspiration of the studied subject presented here. The experimental results on the RTD's provided by the group of Prof. Lukas Worschech from University of Wuerzburg, showed a bistability of the $I - V$ characteristics and its enhanced area with temperature, as well as its linear threshold shift whenever a nearby and latticed matched GaInNAs absorption layer was considered. In the first case, the theoretical model, based on the TMM, indicates that by increasing the resistente, while decreasing the temperature, the bistable area enhances. In the latter case, the presence of a GaInNAs layer lead to a additional sheet charge formed at the GaInNAs/GaAs interface. Under this configuration, the total voltage drop of the RTD changes due to a charge accumulation increase.

The plausibility of building inhomogeneous heterostructures of a single semiconductor material was long ago theoretically predicted when stacking faults and the creation of layered systems of semiconductor segments between twin-planes were simulated. [21] There is however a major shortcoming in the effective use of twin-planes for quantum effects in zincblende heterostructures: the mere presence of a twin stacking fault would not practically affect the transmission of Γ-electrons and these interfaces would remain mostly transparent. [63, 64] Just recently, the controlled synthesis of stacking fault heterostructures of III-V compound semiconductor NWs has been reported. [3, 4] It was shown that by controlling either the growth temperature and diameter of InAs NWs [3] or the amount of impurity dopants in analogous InP systems [4], a twin-plane superlattice can be experimentally realized. Such a microscopic control of the crystalline structure during the NW synthesis would open up opportunities for a thorough modulation of their electronic structure, thus increasing the potential use of these NWs as quantum heterodevices.

A systematic study about the microscopic structure of twin-plane NWs, Fig. 1.2(a), the formation of their peculiar strain fields affected by the surface and twin-plane interfaces, and how they influence the electronic structure and transport properties of Γ-electrons
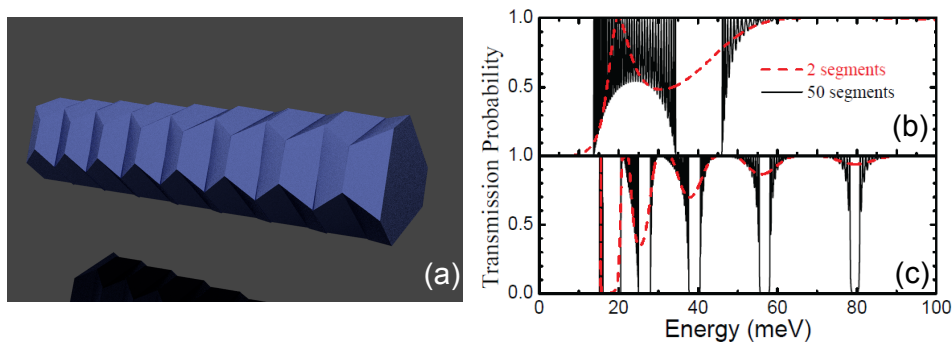
Fig. 1.2: (a) Scheme of the twin-plane nanowire. (a) and (b) Transmission probability for carriers at the top of the valence band as a function of the hole energy for relaxed NWs or under tension. The dashed (solid) line is the transmission for a NW composed of 2 (50) segments. The full transparency condition occurs when the transmission probability is equal to 1. In all cases the energy has been measured from the corresponding band minimum.

and holes will also be described here, as exemplified in Fig. 1.2(b) and (c). In collaboration with the group of Prof. Jose P Rino, we studied the properties of InP zincblende type NWs by employing their MD simulations combined with a multiband electronic structure calculation. The electronic transport was analyzed within the envelope function approximation. We show that exploring twin-plane superlattices as active part of nanocircuits can be successfully achieved if the external control of such strain dependency is mastered.

Finally, Chapter 7, in direct connection with experimental results, provided by collaborators, presents the study of electron transport in a system of quantum dot chains within the framework of 1D hopping model. The progress in nano-scale electronics architecture and the continuous search for ultra-small circuit components have resulted in increased interest in the unique properties of low-dimensional systems such as coupled quantum dots (QDs) and quantum dot chains (QDCs) [1, 2]. In previous reports, using structural and optical characterization techniques, it was shown that the QDC systems have a complex band structure caused by the combination of two-dimensional (2D), one-dimensional (1D) and zero-dimensional (0D) densities of states [65, 66]. In this regard, systems of 1D coupled QDs have attracted much attention both in order to understand the underlying physics [67] and to develop novel devices. The co-existence of 2D and 1D states, that are important for enhanced electrical conductivity, as well as 1D and 0D states, that can play a role in the suppression of thermal conductivity, also makes this system a potential target for development of thermoelectric applications [68].

In collaboration with the experimental group of Prof. Greg Salamo from University of

Arkansas, where electron mobility in a system of QDCs was investigated, we developed a 1D hopping model in order to characterize the carrier transport is this kind of system. The presence of 0D states on top of a 1D wetting layer makes the electron transport in QDCs different from a system of continuous wires. This results in a different anisotropic response as well as enhanced hopping at low temperatures. Detailed studies of the mechanisms of conductance in a system of quantum dot chains as a function of temperature and under the influence of a remote doping level was performed by collaborators where they demonstrated that the behavior of the conductance is complex due to the availability of states of different dimensionalities. Thus, we find that the presence of 0D states plays a key role in the anisotropic behavior of the conductance in this system and compare the experimental response to a 1D hopping model.

In all the problems tackled, our contribution was to provide theoretical predictions or answer to challenging questions posed by experimental evidences. Original results were attained in every topic and the work resulted in the following publications:

(1) H. Tsuzuki, D. F. Cesar, M. Rebello de Sousa Dias, L. K. Castelano, V. Lopez-Richard, J. P. Rino, G. E. Marques, Tailoring Electronic Transparency of Twin-Plane 1D Superlattices. **ACS Nano**, v. 5, p. 5519, 2011.

(2) M. Rebello Sousa Dias, A. Picinin, V. Lopez-Richard, S. E. Ulloa, L. K. Castelano, J. P. Rino, G. E. Marques, Tuning hole mobility in InP nanowires. **Applied Physics Letters**, v. 101, p. 182104, 2012.

(3) V. P. Kunets, M. Rebello Sousa Dias, T. Rembert, M. E. Ware, Y. I. Mazur, V. Lopez-Richard, H. A. Mantooth, G. E. Marques, G. J. Salamo, Electron transport in quantum dot chains: Dimensionality effects and hopping conductance, **Journal of Applied Physics**, v. 113, p. 183709, 2013.

(4) M. Rebello Sousa Dias, V. Lopez-Richard, G. E. Marques, S. E. Ulloa, Spin filtering in nanowire directional coupler, **Europhysics Letters**, v. 106, p. 17002, 2014.

2. ELECTRONIC STRUCTURE OF SEMICONDUCTOR NANOWIRES

2.1 The 1D confinement and strain effects within the $\mathbf{k} \cdot \mathbf{p}$ model

The study that correlates transport behavior and structural properties, as geometry and composition, through the electronic structure of NWs, allows a better understanding of electromagnetic field and strain effects. [26, 9, 27] The 1D confinement in this system leads to quantum peculiarities that become clear in this type of analysis.

The knowledge about morphological details of NWs is very important for the electronic structure description and we will illustrate this by using the example of available data of InP NWs. These structures have been grown via the vapor-liquid-solid method in a CBE ("*Chemical Beam Epitaxy*") machine. Fig. 2.1(a) shows the morphology and crystal structure of a sample through scanning electron microscopy (SEM) and Fig. 2.1(b) shows the corresponding transmission electron microscopy (TEM) results. [9] The verification that the NWs are strained was done through the Fourier transform analysis of the high resolution images (Fig. 2.1(c)) with the electron diffraction of a selected area (Fig. 2.1(d)). The reported values of the deformation are: $\epsilon_{\parallel} = -0.9\%$, biaxial strain, and $\epsilon_{zz} = 1.00\%$, strain along the axis of the wire. [26]

In the following section, the electronic structure calculations of the valence band, which take into account the effects detected of confinement and strain, are going to be discussed.

2.1.1 $\mathbf{k} \cdot \mathbf{p}$ model: Luttinger Hamiltonian

The theoretical simulation of electronic and transport properties of semiconductor materials is always subjected to approximations due to the difficulty of treating systems of many particles. The band structure calculation of semiconductor systems follows this standard. The formalism chosen in this work is based on the idea that the influence of a periodic potential over an electron in a crystal lattice can be taken into account through the concept of effective mass. [28] The presence of a periodic crystalline potential makes
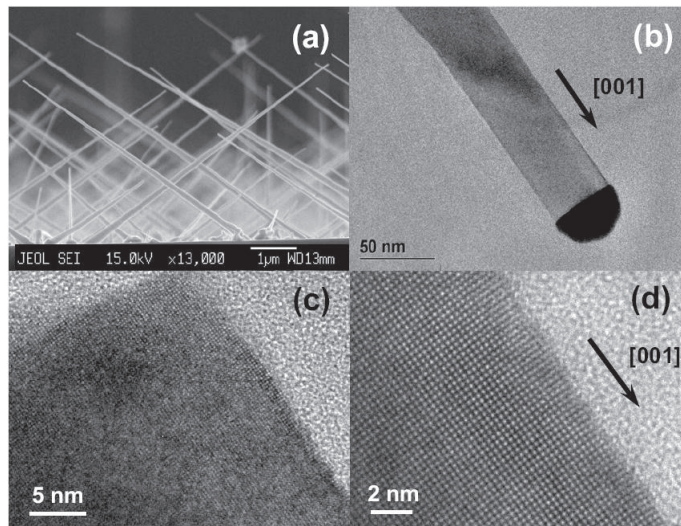
Fig. 2.1: (a) Scanning Electron Microscopy (SEM) of InP nanowires (NWs) on [001] direction. (b) Transmission Electron Microscopy (TEM) image of a InP NW. (c) High resolution TEM image of the NW base corner. (d) High resolution TEM image of the NW parte side [9].

the Bloch theorem valid which describes, in first approximation, the electron state as a charge carrier with effective mass m^*, differing from the free electron mass. This approach is based on a Hamiltonian model called the $\mathbf{k} \cdot \mathbf{p}$ method and various approximations can be used according to the electronic state and the semiconductor materials. In this thesis, we have used two kinds: the parabolic approximation and the Luttinger model.

The $\mathbf{k} \cdot \mathbf{p}$ method allows the band structure calculation in a vicinity of symmetry points of the Brillouin zone. For semiconductors with zinc blende type symmetry, an important point is located at $\mathbf{k} = 0$ (Γ-point) which is the reciprocal lattice center where the states responsible for the optical recombination belong. In summary, we followed three steps for the effective band structure calculations of the systems of interest: (i) transformation of the crystal Hamiltonian to the $\mathbf{k} \cdot \mathbf{p}$ representation, (ii) reduction of the problem to the eigenvalues calculation, and (iii) introduction of approximations.

In order to accomplish the first step, we started from the Schrödinger equation

$$\mathcal{H}_0 \Psi(\mathbf{r}) = \mathcal{E}\Psi(\mathbf{r}), \tag{2.1}$$

where the Hamiltonian that determines the total charge carrier energy has the kinetic and the potential ($U(\mathbf{r})$) energy terms. The latter has the crystal lattice periodicity

$$\mathcal{H}_0 = \frac{p^2}{2m_0} + U(\mathbf{r}). \tag{2.2}$$

In this equation, $p = -i\hbar\nabla$ is the linear momentum operator and m_0 is the free electron mass.

The Bloch theorem can be used due to the periodicity of $U(\mathbf{r})$. [69] This allows the restriction of the eigenvalue spectrum of p which characterize the carrier in the first Brillouin zone of the reciprocal space. Being $\mathcal{E}_n(\mathbf{k})$ the total particle energy for a certain wave vector $\mathbf{k}$, where n enumerates the possible energy bands, we can write the wave functions of the Eq. (2.1) as

$$\Psi_{n\mathbf{k}}(\mathbf{r}) = e^{i\mathbf{k}.\mathbf{r}} u_{n\mathbf{k}}(\mathbf{r}), \tag{2.3}$$

where $u_{n\mathbf{k}}(\mathbf{r})$ are functions with the same periodicity of $U(\mathbf{r})$. The system has translational symmetry which allowed the canonical transformation of $\mathcal{H}_0$,

$$\mathcal{H}(\mathbf{k}) = e^{-i\mathbf{k}.\mathbf{r}} \mathcal{H}_0 e^{i\mathbf{k}.\mathbf{r}}. \tag{2.4}$$

Expanding the Hamiltonian above in Taylor series, we have

$$\mathcal{H}(\mathbf{k}) = \mathcal{H}_0 - i\mathbf{k}.[\mathbf{r}, \mathcal{H}_0] - \frac{1}{2}\sum_{ij} k_i k_j [r_i, [r_j, \mathcal{H}_0]] + ... \tag{2.5}$$

Using the commutation relation between the position and momentum operators, $[\mathbf{r}, \mathcal{H}_0] = i\hbar\mathbf{p}/m_0$ and $[\mathbf{r}, [\mathbf{r}, \mathcal{H}_0]] = -i\hbar^2\delta_{ij}/m_0$, one can write the Hamiltonian as

$$\mathcal{H}(\mathbf{k}) = \frac{p^2}{2m_0} + U(\mathbf{r}) + \frac{\hbar^2 k^2}{2m_0} + \frac{\hbar}{m_0}\mathbf{k} \cdot \mathbf{p}, \tag{2.6}$$

which is the operator where eigenfunctions and eigenvalues are defined for the Bloch function of the periodic part, $u_{n\mathbf{k}}(\mathbf{r})$. In this way, Eq. (2.1) becomes

$$\left[\frac{p^2}{2m_0} + U(\mathbf{r}) + \frac{\hbar^2 k^2}{2m_0} + \frac{\hbar}{m_0}\mathbf{k} \cdot \mathbf{p}\right] u_{n\mathbf{k}} = \mathcal{E}_{n\mathbf{k}} u_{n\mathbf{k}}. \tag{2.7}$$

The terms $\mathbf{k}$-dependent in Eq. (2.7) vanishes at $\mathbf{k} = 0$. Thus, the solution for $\mathbf{k}$ close to the Γ-point can be described as

$$u_{n\mathbf{k}} = \sum_m C_m(\mathbf{k}) u_{m\mathbf{0}}. \tag{2.8}$$

Inserting the solution (2.8) in Eq. (2.7), multiplying by the complex conjugated, $u_{m0}*$,

and integrating over the unitary cell volume, one has

$$\sum_m \left[\left(\mathcal{E}_{n0} - \mathcal{E}_{n\mathbf{k}} + \frac{\hbar^2 k^2}{2m_0} \delta_{nm} \right) + \frac{\hbar\mathbf{k}}{2m_0} \cdot \langle n0|\mathbf{p}|m0 \rangle \right] C_m(\mathbf{k}) = 0. \tag{2.9}$$

The diagonalization of Eq. (2.9) gives the dispersion relation, $\mathcal{E}_n(\mathbf{k})$, and the expansion coefficients, $C_m(\mathbf{k})$, for all $\mathbf{k}$ in all energy bands n.

Using perturbation theory on the non-degenerated n^{th} band with energy equal to $\mathcal{E}_{n0}$, for small values of $\mathbf{k}$, one has

$$C_n \sim 1; \;\; C_m = \frac{\hbar\mathbf{k}}{2m_0} \cdot \frac{\mathbf{p}_{nm}}{\mathcal{E}_{n0} - \mathcal{E}_{m0}}. \tag{2.10}$$

Inserting this result in Eq. (2.9), the energy second order correction can be obtained as

$$\mathcal{E}_{n\mathbf{k}} = \mathcal{E}_{n0} + \frac{\hbar^2 k^2}{2m_0} + \frac{\hbar^2}{m_0^2} \sum_{m \neq n} \frac{|\mathbf{p}_{nm} \cdot \mathbf{k}|^2}{\mathcal{E}_{n0} - \mathcal{E}_{m0}}. \tag{2.11}$$

The non-degenerated band dispersion relations are parabolic for $\mathbf{k} \sim 0$. Close to the Γ-point, one has

$$\mathcal{E}_{n\mathbf{k}} = \mathcal{E}_{n0} + \frac{\hbar^2}{2} \sum_{i,j} ki \frac{1}{m_n^{ij}} k_j, \tag{2.12}$$

where i, j indexes are the cartesian coordinates x, y, z, and m_n^{ij} is the effective mass tensor. Using Eq. (2.11), m_n^{ij} is defined as [69]

$$\frac{1}{m_n^{ij}} = \frac{1}{m0} \delta_{ij} + \frac{2}{m_0^2} \sum_{n \neq m} \frac{p^i p^j}{\mathcal{E}_{n0} - \mathcal{E}_{m0}} \tag{2.13}$$

Notice that the effective mass tensor obtained takes in consideration only the kinetic and the periodic potential of the system. However, one can introduce the spin-orbit relativistic correction. This new term replaces the operator $\mathbf{p}$ with

$$\boldsymbol{\pi} = \mathbf{p} + \frac{\hbar}{4m_0 c^2} (\boldsymbol{\sigma} \times \nabla U), \tag{2.14}$$

where $\boldsymbol{\sigma}$ are the Pauli matrices. [69, 70]

The simplest model for the structure of both conduction (c) and valence (v) bands of

a semiconductor is the parabolic one. Here, the effective mass tensor is isotropic

$$\mathcal{E}_{c/v}(\mathbf{k}) = \pm \left(\frac{\mathcal{E}_g}{2} + \frac{\hbar^2 k^2}{2m^*_{(c/v)}} \right), \tag{2.15}$$

where $\mathbf{k}$ is the wave vector from the Brillouin zone center, $\mathcal{E}_g$ is the energy gap, and $m^*_{c/v}$ are the effective masses of the conduction and valence bands. [71]

For the conduction band of wide gap semiconductors ($\mathcal{E}_g \geq 500$ meV), such approximation is reasonable and was used in our approach to calculate the electronic structure of electrons. However, the effective mass tensor in the valence band of these semiconductor materials has a marked anisotropic character and such approximation cannot be considered. Therefore, effects of non-parabolicity, anisotropy, and coupling between light holes (LH) and heavy holes (HH) must be taken into account.

The description of the electronic structure above is based on the Bloch theorem, relevant to volumetric systems (bulk). In this case, due to translational invariance, the wave vector components (linear momentum) are good quantum numbers. Nevertheless, its scope can be extended to nanoscopic systems, such as quantum wells, nanowires and quantum dots, where the crystal symmetry properties still exist. In these systems, the wave vector components (linear momentum) become differential operators.

To study the valence band, the Luttinger model is going to be used [72]. The Eq. (2.9) has infinite dimension and it is impossible to solve it exactly. However, our region of interest is restricted to the energy states in the vicinity of $\mathbf{k} = 0$ where $\mathbf{k} \cdot \mathbf{p}$ method is suitable. In order to solve the Eq. (2.9), the method developed by Löwdin [73] was used. This method use perturbation theory and exact diagonalization. Luttinger [72], using this approach, derived an effective Hamiltonian ($\mathcal{H}_L$) for the valence band calculation considering only symmetry aspects. [74] In this case, one can write the representation of the Hamiltonian (2.9) on the basis of the total angular momentum eigenstates, $|J, m_J\rangle$ $|3/2, +3/2\rangle = \frac{1}{2}|(x+iy)\uparrow\rangle$, $|3/2, +1/2\rangle = \frac{1}{\sqrt{6}}|(x+iy)\downarrow -2z\uparrow\rangle$, $|3/2, -3/2\rangle = \frac{1}{2}|(x-iy)\downarrow\rangle$,

$|3/2, -1/2\rangle = \frac{1}{\sqrt{6}}|(x - iy) \uparrow +2z \downarrow\rangle$, as

$$\mathcal{H}_L \Psi_{n',p}(\rho, \theta, z) = \frac{\hbar^2}{m_0} \begin{pmatrix} D_{HH}^+ & A_- & 0 & B_- \\ & D_{LH}^+ & B_- & 0 \\ & & D_{HH}^- & A_+ \\ & & & D_{LH}^- \end{pmatrix} \sum_{p,n'} \begin{pmatrix} C_{1,n'}\Phi_{n',p}(\rho, \theta, z) \left|\frac{3}{2}, +\frac{3}{2}\right\rangle \\ C_{2,n'}\Phi_{n',p}(\rho, \theta, z) \left|\frac{3}{2}, +\frac{1}{2}\right\rangle \\ C_{3,n'}\Phi_{n',p}(\rho, \theta, z) \left|\frac{3}{2}, -\frac{3}{2}\right\rangle \\ C_{4,n'}\Phi_{n',p}(\rho, \theta, z) \left|\frac{3}{2}, -\frac{1}{2}\right\rangle \end{pmatrix}$$

$$= \mathcal{E} \sum_{n',p} \begin{pmatrix} C_{1,n'}\Phi_{n',p}(\rho, \theta, z) \left|\frac{3}{2}, +\frac{3}{2}\right\rangle \\ C_{2,n'}\Phi_{n',p}(\rho, \theta, z) \left|\frac{3}{2}, +\frac{1}{2}\right\rangle \\ C_{3,n'}\Phi_{n',p}(\rho, \theta, z) \left|\frac{3}{2}, -\frac{3}{2}\right\rangle \\ C_{4,n'}\Phi_{n',p}(\rho, \theta, z) \left|\frac{3}{2}, -\frac{1}{2}\right\rangle \end{pmatrix}, \tag{2.16}$$

where

$$D_{HH}^{\pm} = -\left(\frac{\gamma_1 + \gamma_2}{2}\right)\{\hat{k}_+, \hat{k}_-\} - \left(\frac{\gamma_1 - 2\gamma_2}{2}\right)\hat{k}_z^2, \tag{2.17}$$

$$D_{LH}^{\pm} = -\left(\frac{\gamma_1 - \gamma_2}{2}\right)\{\hat{k}_+, \hat{k}_-\} - \left(\frac{\gamma_1 + 2\gamma_2}{2}\right)\hat{k}_z^2, \tag{2.18}$$

$$A_{\pm} = -\sqrt{3}\gamma_3\hat{k}_{\pm}\hat{k}_z, \tag{2.19}$$

$$B_{\pm} = -\frac{\sqrt{3}}{2}\frac{\gamma_2 + \gamma_3}{2}\hat{k}_{\pm}^2, \tag{2.20}$$

and γ_α ($\alpha = 1, 2, 3$) are the Luttinger parameters, responsible for the effective mass anisotropy of holes, and coupling between the light and heavy holes, $\{A, B\} = \frac{1}{2}(AB + BA)$, and $\hat{k}_{\pm} = \hat{k}_x \pm i\hat{k}_y$. The values used for the effective valence band calculations of an InP NW were $\gamma_1 = 4.95$, $\gamma_2 = 1.65$, and $\gamma_3 = 2.35$. [75]

The description of NWs with cylindrical and semi-cylindrical 1D confinement is more suitable in polar coordinates, where

$$\hat{k}_{\pm} = -ie^{\pm i\theta}\left(\frac{\partial}{\partial\rho} \pm \frac{i}{\rho}\frac{\partial}{\partial\rho}\right), \tag{2.21}$$

$$\hat{k}_{\pm}^2 = e^{\pm 2i\theta}\left(-\frac{\partial^2}{\partial\rho^2} \pm \frac{2i}{\rho^2} \mp \frac{2i}{\rho}\frac{\partial}{\partial\rho}\frac{\partial}{\partial\theta} + \frac{1}{\rho}\frac{\partial}{\partial\rho} + \frac{1}{\rho^2}\frac{\partial^2}{\partial\theta^2}\right), \tag{2.22}$$

and

$$\{\hat{k}_+, \hat{k}_-\} = -\left[\frac{\partial^2}{\partial\rho^2} + \frac{1}{\rho}\frac{\partial}{\partial\rho} + \frac{1}{\rho^2}\frac{\partial^2}{\partial\theta^2}\right]. \tag{2.23}$$

Using hard wall confinement for the boundary conditions, one can expand the wave function in the basis of eigenfunctions of the infinite cylinder with radius a (Fig. 2.2 (a)). Thus, for a cylinder

$$\Phi_{n,p}(\rho, \theta) = \frac{J_n\left(\frac{\mu_{np}\rho}{a}\right)e^{in\theta}}{\sqrt{\pi}a|J_{n+1}(\mu_{np})|}, \text{ with } n = \pm 1, \pm 2, \pm 3, ..., \tag{2.24}$$

and for a semi-cylinder (Fig. 2.2 (b))

$$\Psi_{n,p}(\rho, \theta) = \frac{2J_n\left(\frac{\mu_{np}\rho}{a}\right)\sin(n\theta)}{\sqrt{\pi}a|J_{n+1}(\mu_{np})|}, \text{ with } n = 1, 2, 3, ..., \tag{2.25}$$

where J_n are the Bessel functions and μ_{np} is the p-th zero of the Bessel function with order n.
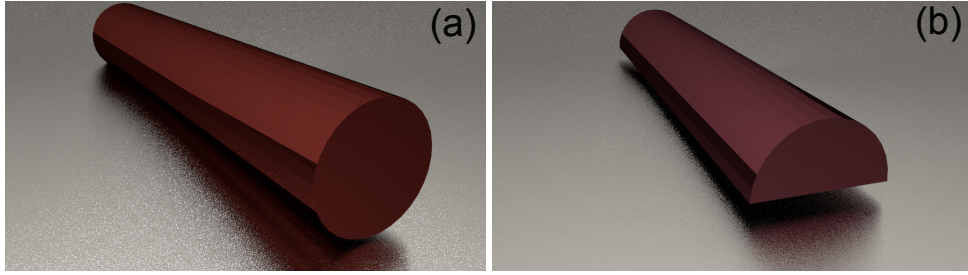
Fig. 2.2: (a) Cylindrical InP NW with radius a. (b) Semi-cylindrical InP NW with radius a.

To build the Hamiltonian matrix it is necessary calculate the terms $\langle n, p | \{\hat{k}_+, \hat{k}_-\} | n', p' \rangle$, $\langle n, p | \hat{k}_\pm | n', p' \rangle$ and $\langle n, p | \hat{k}_\pm^2 | n', p' \rangle$. Using the wavefunction (2.24) one can demonstrate that

$$\langle n, p | \{\hat{k}_+, \hat{k}_-\} | n', p' \rangle = \frac{\mu_{n,p}^2}{a^2} \delta_{n',n} \delta_{p',p}, \tag{2.26}$$

$$\langle n, p | \hat{k}_\pm | n', p' \rangle = \mp \frac{2i}{a} T_{n',p'}^{n,p} \delta_{n',n\mp 1} \text{ , and}$$

$$\langle n, p | \hat{k}_\pm^2 | n', p' \rangle = \mp \frac{4(n \mp 1)}{a^2} T_{n',p'}^{n,p} \delta_{n',n\mp 2}$$

with

$$\lim_{n \longrightarrow \mp 1} \{\pm(n+1)T_{n\pm 2,p'}^{n,p}\} = 2\mu_{n,p}^2 \delta_{p',p}, \tag{2.27}$$

where $T_{n',p'}^{n,p} = \frac{\mu_{n,p}/\mu_{n',p'}}{(\mu_{n,p}/\mu_{n',p'})^2 - 1}$.

In a similar way, using the wavefunction (2.25) one have

$$\langle n, p | \hat{k}_+ | n', p' \rangle = i \text{sgn}(n - n') T_{n'\pm 1,p'}^{n,p} \quad \text{if } n' = n \pm 1, \text{ and} \tag{2.28}$$

$$\langle n,p|\hat{k}_+|n',p'\rangle = \frac{2n}{\mu_{n,p}\pi} \frac{1+(-1)^{n+n'}}{J_{n'+1}(\mu_{n',p'})J_{n'+1(\mu_{n,p})}} F_{n',p'}^{n,p} \quad \text{if } n' \neq n \pm 1$$

where $\text{sgn}(x) = 1$ if $x > 0$ and $\text{sgn}(x) = -1$ if $x < 0$, and $F_{n',p'}^{n,p}$ is given by

$$F_{n',p'}^{n,p} = \int_0^{\mu_{n',p'}} z J_n\left(\frac{\mu_{n,p}z}{\mu_{n',p'}}\right)\left[\frac{J_{n'-1(z)}}{(1-n')^2-n^2} - \frac{J_{n'+1(z)}}{(1+n')^2-n^2}\right] dz. \qquad (2.29)$$

for $n = n'$ and $p = p'$ one have $F_{n',p'}^{n,p} = \frac{2n}{(2n)^2-1}\int_0^{\mu_{n,p}}\frac{d}{dz}zJ_n(z)^2dz$. Also, $\langle n,p|\hat{k}_-|n',p'\rangle = (-1)^{n'+n+1}\langle n,p|\hat{k}_+|n',p'\rangle$. The other matrix elements are evaluated numerically.

The analytical solution of the Luttinger Hamiltonian matrix elements, showed above, in the function basis of Eq. (2.24) and Eq. (2.25) allowed a compact representation of the Hamiltonian and its separation into orthogonal Hilbert subspaces. This facilitates the representation of eigenfunctions and the application of numerical methods for the eigenvalue problem diagonalization. [27]

Besides the quantization effects, the strain produced by the presence of surfaces, interfaces, and/or external stress, contributes to the electronic structure of quantum wires and requires its inclusion within the Hamiltonian model. These effects will be detailed in the next section.

2.1.2   Strain

Taking into account the deformation of the crystalline structure, due to tensions, like the ones observed experimentally, [26] one must add terms to the Hamiltonian $\mathcal{H}_L$ that consider these effects. In the case of a biaxial deformation on structures grown along to the [001] direction, such as NWs, the strain effect appear as displacements of the top of the bands modified by parameters associated with the deformation potentials. [76]

Using a diagonal Hamiltonian, one can write $\mathcal{H}_L$ with the strain displacement

$$\mathcal{H}_L^D = \frac{\hbar^2}{m_0}\begin{pmatrix} D_{HH}^+ + \Delta\mathcal{E}_{HH} & 0 & 0 & 0 \\ & D_{LH}^+ + \Delta\mathcal{E}_{LH} & 0 & 0 \\ & & D_{HH}^- + \Delta\mathcal{E}_{HH} & 0 \\ & & & D_{LH}^- + \Delta\mathcal{E}_{LH} \end{pmatrix}.$$

For the HH subband the displacement is given by,

$$\Delta \mathcal{E}_{HH} = -P - Q, \tag{2.30}$$

and for the LH,

$$\Delta \mathcal{E}_{LH} = -P + Q + \frac{2(Q)^2}{\Delta_{SO}}, \tag{2.31}$$

where $P = 2(a_v + a_c)(\frac{c_{11}-c_{12}}{c_{11}})\epsilon_{\parallel}$, and $Q = -b(\frac{c_{11}+2c_{12}}{c_{11}})\epsilon_{\parallel}$. The parameters required for the displacement calculation are displayed in Table 2.1.

Tab. 2.1: Parameters for $\Delta \mathcal{E}_{LH}$, and $\Delta \mathcal{E}_{HH}$. [77, 78]

Deformation potential (dyn cm^{-2})	
c_{11}	10.11×10^{11}
c_{12}	5.61×10^{11}
Elastic modulus (eV)	
a_c	-7.0
a_v	-0.6
Δ_{SO} (eV)	
0.108	

Introducing the stain effects, one may notice that a negative energy displacement for both LH and HH subbands occurs. The valence band ground state has a LH character for a system with no stain, whereas a biaxial strain can change this character to HH. [27]

2.1.3 InP nanowire valence band calculation

Based on the analytical results for the matrix elements we proceed and set the complete Hamiltonian, $\mathcal{H}_L$. The valence band energy levels of a cylindrical InP NW with no strain effects are shown in Fig. 2.3(a)

Figure 2.3(b) shows the valence band energy levels including strain effects, where the biaxial strain, $\epsilon_{\parallel} = -0.9\%$, is in agreement with experimental results. [9] The difference in energy, at $k_z = 0$, between the HH and LH subbands is $|\Delta \mathcal{E}_{HH-LH}| = 73,87$ meV with strain and $|\Delta \mathcal{E}_{HH-LH}| = 28,61$ meV, with no strain.

Through the coefficient calculation of the expansion of the wave function one can assess the character of the valence band. [27] As one can see, for a NW with no strain,
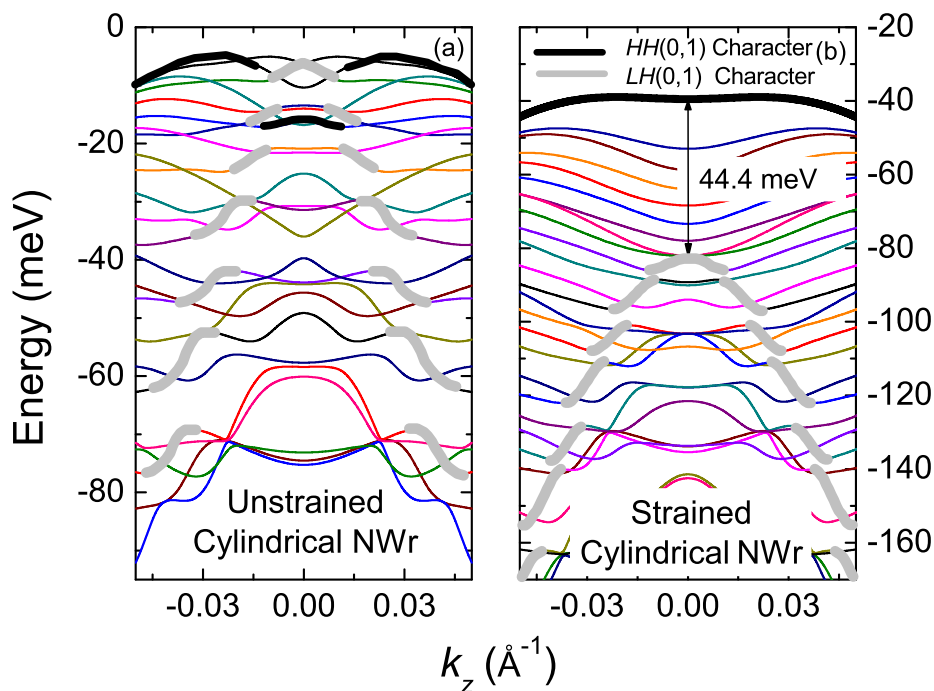
Fig. 2.3: Energy dispersion for a cylindrical InP NW with radius $a = 185$Å. (a) Without strain and (b) with strain. [9]

Fig. 2.3(a), the LH(0,1) character is highlighted in gray while the HH(0,1) is in black (the notation corresponds to the quantum numbers (n,p) described above). Considering strain effects, a reordering takes place in the ground states. The HH(0,1) becomes an almost pure state and appears at the top of the band (black line on Fig. 2.3(b)), while the LH(0,1) character is still present in many excited states (grey line on Fig. 2.3(b)).

These results show the main confinement effect in a quasi-one-dimensional system. With no strain, the ground state has a LH character, close to $k_z = 0$, as opposed to the quasi-bi-dimensional (quantum well) nanostructures, where the ground state has a HH character. This peculiar result on the effective mass anisotropy of the valence band, pointed in the diagonal elements of the Luttinger Hamiltonian, are related with the effective masses of the HH and LH in the plane perpendicular to the NW axis, proportional to $(\gamma_1 + \gamma_2)^{-1}$ and $(\gamma_1 - \gamma_2)^{-1}$ respectively. Thus, the smaller mass in this plane is the one from the HH, and this is more sensitive to the confinement effects, as shown in Figs. 2.3(a) and (b). The strain effects provoke the inversion of this behavior.

Following the same procedure as in the cylindrical case, one can write all matrix elements in the function basis of Eq. (2.25) in order to obtain analytical expressions that allow a compact Hamiltonian representation for the semi-cylinder. The valence band

energy levels of a semi-cylindrical InP NW with no strain effects are shown in Fig. 2.4(a).
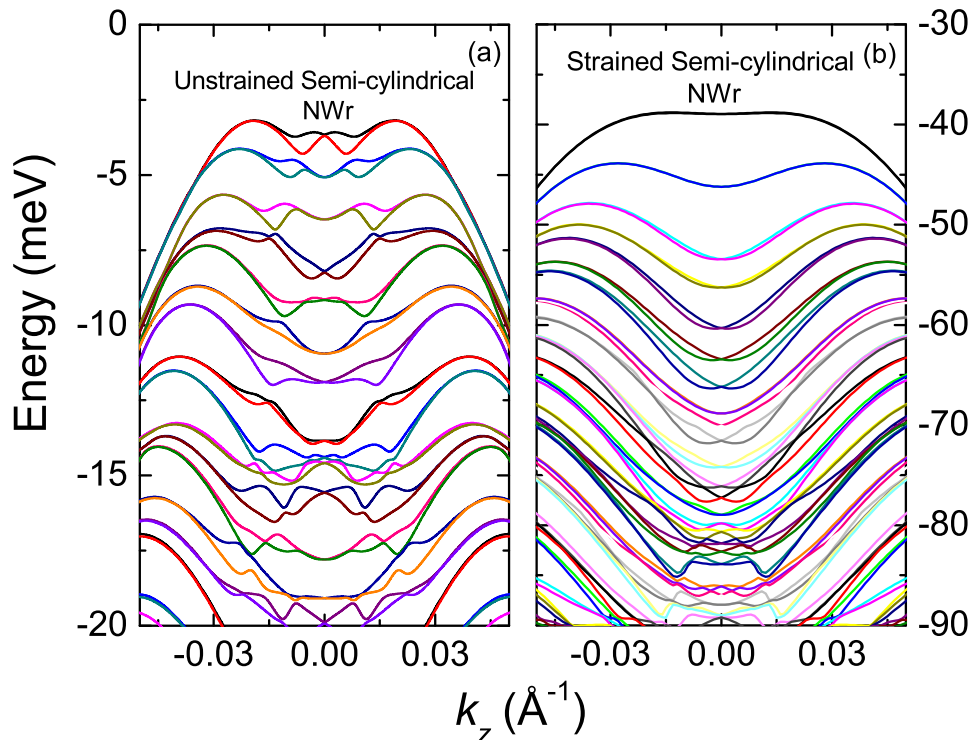
Fig. 2.4: Energy dispersion for a semi-cylindrical InP NW without strain (a) and with strain (b)

Figure 2.4(b) shows the valence band energy levels including strain effects, where $\epsilon_{||} = -0.9\%$. The difference in energy, at $k_z = 0$, between the HH and LH subbands is $|\Delta\mathcal{E}_{HH-LH}| = 39.85$ meV with stain and $|\Delta\mathcal{E}_{HH-LH}| = 5.4$ meV with no strain. In comparison with the cylindrical case, one can see the same behavior but the confinements effects are more evident, higher density of state in a smaller energy window, this is due to the rotational symmetry breakdown.

The next step will introduce the electron-phonon interaction. This scattering mechanism may play a crucial role in the modulation of carrier transport. Although the carrier-phonon interaction can be of various natures, we will consider the effects of the hole coupling with longitudinal-optical (LO) phonons via deformation potentials.

2.2   *Electron-phonon interaction*

The mobility is a quantity that depends on the charge carrier lifetime,$\mu = \frac{e}{m^*}\tau$, that is affected by the electron-phonon scattering and defined as,

$$\frac{1}{\tau(k)} = \sum_q S(k,q), \qquad (2.32)$$

with the transition rate given by

$$
S(k, k') = \frac{2\pi}{\hbar} \left[|\langle \Psi_{l'} | \mathcal{H}^a_{e-p} | \Psi_l \rangle|^2 \delta(\mathcal{E}_f(k') - \mathcal{E}_i(k) - \hbar\omega_{\mathbf{q}}) + \right.
$$
$$
\left. |\langle \Psi_{l'} | \mathcal{H}^e_{e-p} | \Psi_l \rangle|^2 \delta(\mathcal{E}_f(k') - \mathcal{E}_i(k) + \hbar\omega_{\mathbf{q}}) \right], \tag{2.33}
$$

where k and k' refer to the initial and final states responsible for the transition probability of the scattering processes, $\mathcal{H}^a_{e-p}$ and $\mathcal{H}^e_{h-p}$ refer to the phonon absorption and emission processes, characterized by the phonon energy $\hbar\omega_{\mathbf{q}}$, and $\mathcal{E}_f(k')$ and $\mathcal{E}_i(k)$ correspond to the energy of the inicial (i) state and final (f), respectively.

The hole-phonon interaction Hamiltonian is given by

$$
\mathcal{H}_{e-p} = \sum_{\mathbf{q}} M_{\mathbf{q}} U_{e-i}(\mathbf{q})[\hat{a}_{\mathbf{q}} e^{i\mathbf{r}\cdot\mathbf{q}} + \hat{a}^\dagger_{\mathbf{q}} e^{-i\mathbf{r}\cdot\mathbf{q}}], \tag{2.34}
$$

with $M_{\mathbf{q}} = (\mathbf{q} \cdot \varepsilon_q) \left(\frac{\hbar}{2\rho\omega_{\mathbf{q}}V} \right)^{\frac{1}{2}}$, where $\mathbf{q}$ is the phonon wave vector for polarization vector ε_q, ρ is the mass density, V is the system volume, and $U_{e-i}(\mathbf{q})$ is given in terms of the deformation potential, [79, 80] where a_0 is the lattice parameter. Thus,

$$
\langle \Psi_{l'} | \mathcal{H}^a_{e-p} + \mathcal{H}^e_{e-p} | \Psi_l \rangle = \sum_{\mathbf{q}} M_{\mathbf{q}}[\langle \Psi_{l'} | U_{e-i}(\mathbf{q})\hat{a}_{\mathbf{q}} e^{i\mathbf{r}\cdot\mathbf{q}} | \Psi_l \rangle + \langle \Psi_{l'} | U_{e-i}(\mathbf{q})\hat{a}^\dagger_{\mathbf{q}} e^{-i\mathbf{r}\cdot\mathbf{q}} | \Psi_l \rangle]. \tag{2.35}
$$

Considering an infinite NW, the wave function has the form

$$
|\Psi_l\rangle = |\psi_l\rangle |n_{\mathbf{q}}\rangle |J, m_j\rangle \tag{2.36}
$$

where $|\psi_l\rangle$ is the envelope function, which depends on the cross section, $|n_{\mathbf{q}}\rangle$ is the phonon eigenstate, and $|J, m_j\rangle$ is the total angular momentum eigenstate. The following Table shows the envelope functions for the three cases considered in this work.

Tab. 2.2: Envelope function for three different cross sections: circular (c) and semicircular (sc) of radius a, and square (s) of width W. $\mu_{n,p}$ is the p-th zero of the n-th order Bessel function and $C = (\sqrt{\pi}a|J_{n+1}(\mu_{n,p})|)^{-1}$.

$\psi^{(c)}_{n,p,k} = C J_n(\mu_{n,p}\frac{r}{a})e^{in\theta}e^{ikz}, \quad n = 0, \pm 1, \pm 2...$
$\psi^{(sc)}_{n,p,k} = 2C J_n(\mu_{n,p}\frac{r}{a})\sin(n\theta)e^{ikz}, \quad n = 1, 2...$
$\psi^{(s)}_{n_x,n_y,k} = \frac{2}{W}\sin(\frac{n_x\pi x}{W})\sin(\frac{n_y\pi y}{W})e^{ikz}, \quad n_x, n_y = 1, 2...$

In order to calculate the matrix element displayed on Eq. (2.35), one can use Eq. (5.2)and obtain $\langle \Psi_{l'} | \mathcal{H}^a_{e-p} + \mathcal{H}^e_{e-p} | \Psi_l \rangle =$

$$
\sum_{\mathbf{q}} M_{\mathbf{q}} [\langle \psi_{n',p',k'} | e^{i\mathbf{r}.\mathbf{q}} | \psi_{n,p,k} \rangle \langle n_{\mathbf{q}-1} | \hat{a}_{\mathbf{q}} | n_{\mathbf{q}} \rangle \langle J', m'_j | U_{e-i}(\mathbf{q}) | J, m_j \rangle
$$
$$
+ \langle \psi_{n',p',k'} | e^{-i\mathbf{r}.\mathbf{q}} | \psi_{n,p,k} \rangle \langle n_{\mathbf{q}+1} | \hat{a}^{\dagger}_{\mathbf{q}} | n_{\mathbf{q}} \rangle \langle J', m'_j | U_{e-i}(\mathbf{q}) | J, m_j \rangle] \tag{2.37}
$$

The annihilation and creation operators act into the phonon eigenstate as $\hat{a}_{\mathbf{q}} | n_{\mathbf{q}} \rangle = \sqrt{n_{\mathbf{q}}} | n_{\mathbf{q}-1} \rangle$ and $\hat{a}^{\dagger}_{\mathbf{q}} | n_{\mathbf{q}} \rangle = \sqrt{n_{\mathbf{q}}+1} | n_{\mathbf{q}+1} \rangle$, where the phonon occupation factor depends on temperature like, $n_q = (e^{\hbar \omega_q / k_B T} - 1)^{-1}$. The matrix elements, in terms of the envelope wave function, for a NW with cylinder cross section are

$$
\langle \psi_{n',p',k'} | e^{i\mathbf{r}.\mathbf{q}} | \psi_{n,p,k} \rangle = \int_{-\infty}^{\infty} \int_0^{2\pi} \int_0^a \frac{J_{n'}(\mu_{n',p'} \frac{\rho}{a}) e^{-in'\theta} e^{-ik'z}}{\sqrt{\pi} a | J_{n'}(\mu_{n',p'})|} e^{i\mathbf{r}.\mathbf{q}} \times
$$
$$
\frac{J_n(\mu_{n,p} \frac{\rho}{a}) e^{in\theta} e^{ikz}}{\sqrt{\pi} a | J_n(\mu_{n,p})|} \rho d\rho d\theta dz, \tag{2.38}
$$

where $e^{i\mathbf{r}.\mathbf{q}} = e^{i\rho.q_t} e^{i\mathbf{z}.\mathbf{q}_z}$, q_t being the transversal component of the phonon wave vector and $\mathbf{q}_z$ the component along the z direction. Therefore,

$$
\langle \psi_{n',p',k'} | e^{i\mathbf{r}.\mathbf{q}} | \psi_{n,p,k} \rangle = 2\delta_{n',n} I_{p',p} \delta_{k',k+q_z}, \tag{2.39}
$$

where

$$
I_{p',p} = \int_0^a \frac{J_{n'}(\mu_{n',p'} \frac{\rho}{a})}{a | J_{n'}(\mu_{n',p'})|} e^{i\rho.q_t} \frac{J_n(\mu_{n,p} \frac{\rho}{a})}{a | J_n(\mu_{n,p})|} \rho d\rho. \tag{2.40}
$$

Equation (2.40) has analytical solution for $q_t = 0$, $I_{p',p} = \frac{1}{2}\delta_{p',p}$. Within the range $q_t \simeq 1/a$, where $q_t \neq 0$, the matrix element does not change significantly. Hence, one can approximate this result by the analytical one, obtained for $q_t = 0$.

The deformation potential operator for electrons (e) and holes (h) is given by [79, 80]

$$
U_{e-i}(\mathbf{q}) = \frac{\sqrt{3}}{2a_0} [D_e(z) - D_h(z)]. \tag{2.41}
$$

Considering long wavelength processes where $\mathbf{q}$ is small and the interaction is in the short range regime, we have $U_{h-i}(\mathbf{q}) \propto \mathbf{u}$, where $\mathbf{u}$ is the relative displacement between atoms inside the primitive unit cell. By symmetry, there are no allowed transitions due to interaction with LO-phonons in conduction band via deformation potential. On the other

hand, in the valence band, states with HH character couple with those of LH character along the direction [001] [80, 79]. As this coincides with the wire axis, along which the carrier transport takes place, we find

$$\langle HH^\pm|U_{h-i}(z)|LH^\mp\rangle = \langle LH^\mp|U_{h-i}(z)|HH^\pm\rangle = \frac{\pm id_0}{2a_0}, \tag{2.42}$$

where $d_0 = 35\,eV\mathring{A}$ is the deformation constant, $a_0 = 5.87\mathring{A}$, and $\rho = \frac{26.98}{c^2}\,10^{11}meV/\mathring{A}^3$. [81]

Rewriting the complete matrix element, we have

$$\langle\Psi_{l'}|\mathcal{H}^a_{e-p} + \mathcal{H}^e_{e-p}|\Psi_l\rangle = \sum_{\mathbf{q}} M_{\mathbf{q}}\delta_{n',n}\delta_{p',p}\frac{\mp id_0}{2a_0}\left[\sqrt{n_{\mathbf{q}}}\delta_{k',k+q_z} + \sqrt{n_{\mathbf{q}}+1}\delta_{k',k-q_z}\right]. \tag{2.43}$$

The compact form of the matrix element on Eq. (2.43) is the first step to calculate carrier life time. As follows, the transition rate calculation will be shown in order to calculate the life time.

2.2.1 Lifetime calculation

The transition probability per unit time from one energy eigenstate of a quantum system is given by Eq. (2.33), the Fermi golden's rule. The phonon density is assumed to be given by a Lorentzian centered at ω_{LO} with width Γ. Thus, the Dirac delta function can be replaced by a Lorentzian,

$$\delta(\Delta\mathcal{E}\pm\hbar\omega_{\mathbf{q}}) \rightarrow \frac{1}{\pi}\frac{\Gamma/2}{(\Delta\mathcal{E}\pm\hbar\omega_{\mathbf{q}})^2 + (\Gamma/2)^2}. \tag{2.44}$$

In the limit where $\Gamma \rightarrow 0$ the delta function is recovered. According to the energy conservation selection rules described on Eq. (2.43), $\Delta\mathcal{E}\pm\hbar\omega_{\mathbf{q}} = \mathcal{E}_f(k\pm q_z) - \mathcal{E}_i(k)\pm\hbar\omega_{\mathbf{q}}$, where se subindex f and i refer to the final and inicial states, respectively. Therefore, the valence band transition energy conservation, in units of $\frac{\hbar^2}{2m_0}$, is given by

$$c_{a,e}\frac{2m_0}{\hbar^2} = \Lambda\left(\frac{1}{\lambda_f} - \frac{1}{\lambda_i}\right) + k^2\left(\frac{1}{\lambda_{zf}} - \frac{1}{\lambda_{zi}}\right) + \frac{q_z^2}{\lambda_{zf}} \pm \frac{2kq_z}{\lambda_{zf}} \mp \frac{\hbar\omega_{\mathbf{q}}}{\sigma}, \tag{2.45}$$

where $\Lambda_c = \frac{\mu_{n,p}^2}{a^2}$, $\Lambda_{sc} = \frac{\mu_{n,p}^2}{a^2}$, and $\Lambda_s = \frac{2\pi^2 n^2}{W^2}$. λ_β and $\lambda_{z\beta}$ are the effective hole masses for the transverse and z-direction, respectively. The mass factors are given by the Luttinger parameters, with $\lambda_{LH}^{-1} = \gamma_1 - \gamma_2$, $\lambda_{zLH}^{-1} = \gamma_1 + 2\gamma_2$, $\lambda_{HH}^{-1} = \gamma_1 + \gamma_2$, and $\lambda_{zHH}^{-1} = \gamma_1 - 2\gamma_2$.

Replacing Eq. (2.44) into Eq. (2.33), we have

$$S(k, q_z) = \frac{\pi d_0^2 q_z^2}{\rho \omega_q V 4 a_0^2} \left[\frac{n_q}{\pi} \frac{\Gamma/2}{(\Delta \mathcal{E} + \hbar \omega_{\mathbf{q}})^2 + (\Gamma/2)^2} + \frac{(n_q + 1)}{\pi} \frac{\Gamma/2}{(\Delta \mathcal{E} - \hbar \omega_{\mathbf{q}})^2 + (\Gamma/2)^2} \right] (2.46)$$

The carrier lifetime, which enables the description of the mobility in semiconductor NWs with cylindrical cross section is given by,

$$\frac{1}{\tau(k)} = \sum_q S(k, q_z) = \frac{V}{(2\pi)^3} \int_0^{2\pi} \int_0^{\frac{1}{a}} \int_{-\infty}^{\infty} S(k, q_z) q_t dq_z . dq_t d\theta \qquad (2.47)$$

Using Eq. (2.46), and performing the integration over q_t and θ direction, the integral along q_z remains as

$$\frac{1}{\tau(k)} = \frac{d_0^2}{\rho \omega_q V 4 a_0^2} \frac{V}{a^2 8\pi^2} \left[n_q \int_{-\infty}^{\infty} \frac{q_z^2 \Gamma/2}{(\Delta \mathcal{E} + \hbar \omega_{\mathbf{q}})^2 + (\Gamma/2)^2} dq_z + \right.$$
$$\left. (n_q + 1) \int_{-\infty}^{\infty} \frac{q_z^2 \Gamma/2}{(\Delta \mathcal{E} - \hbar \omega_{\mathbf{q}})^2 + (\Gamma/2)^2} dq_z \right]. \qquad (2.48)$$

The procedure above is analogous for the two remanent cross sections, semi-cylindrical and squared. Fortunately these cases have analytical solutions. Hence,

$$\frac{1}{\tau(k)} = \frac{d_0^2}{\rho \omega_q V 4 a_0^2} \frac{V}{a^2 8\pi^2} d \left[n_q \Xi_a + (n_q + 1) \Xi_e \right], \qquad (2.49)$$

where

$$\Xi_{a,e} = \frac{\pi}{2 a_{a,e}} \left(\frac{b_{a,e}^2 + i 2 a_{a,e} d - 2 a_a c_{a,e}}{\sqrt{b_{a,e}^2 - 4 a_{a,e} c_{a,e} + 4 i a_{a,e} d}} + \frac{b_{a,e}^2 - i 2 a_{a,e} d - 2 a_a c_{a,e}}{\sqrt{b_{a,e}^2 - 4 a_{a,e} c_{a,e} - 4 i a_{a,e} d}} \right), \qquad (2.50)$$

with $a_{a,e} = \frac{\hbar^2}{2m_0} \frac{1}{\gamma z f}$, $b_{a,e} = \pm \frac{\hbar^2}{2m_0} \frac{2k}{\gamma z f}$, and $d = \frac{\Gamma}{2}$.

This study made possible the characterization of the mobility, mostly defined by the carrier-phonon interaction and phonon-lifetime, through structural parameters. Tuning NW structural properties may result in the possibility of finding optimal conditions for carrier transport. This will be discussed in more detail in the Chapter 4. The next Chapter is devoted to the description of transport mechanisms analyzed in this thesis.

3. TRANSPORT MECHANISMS

The transport regime in semiconductor heterostructures is associated with the fundamental time and length scales available in the system and those attained by the carriers. The wave-particle duality behavior of the carriers defines the regime where the transport takes place, from the quantum to the classical limit. As already stated, for a semiconductor nanostructures the de Broglie wavelength (λ_{db}) of an electron can be comparable with the system length. The value of λ_{db} for a carrier in a semiconductor material also depends on the effective mass, m^*, usually smaller than the free electron mass. [82] In other words, a three dimensional material with all three geometrical dimensions much larger than λ_{db} will have its carrier behaving as a free electron. The reduction of the geometrical length below the value of λ_{db} results in the quantization of the carrier motion. The quasi-one-dimensional heterostructures belong to this limit; sometimes with only one length quantized, quantum wells (QW), other with 2D quantization, nanowires (NWs), and when all the three directions are quantized one has the quantum dots (QDs).

The transport taking place along the direction of quantized dimensions requires a quantum approach, as one will see in Section 3.2. Also, in the case where the carrier does not lose its wavelike behavior, due to electron scattering for example, one still keeps the quantum approach and this is characterized by the ballistic transport regime (Section 3.1). The lost of the carrier wavelike behavior leads to a classical transport approach, where the carrier has a particle-like behavior.

The transition between these two regimes can be characterized by the time and length scales of processes present in a real material, as the electron scattering mentioned above. The scattering processes occur due to impurities, defects, lattice vibration, etc. One can classify them as elastic, when there is a change in momentum conserving energy, or inelastic, involving energy change. The mean time between elastic scattering processers, τ_e, determines the mean free path, $l_e = v\tau_e$, where v is the average electron velocity. Hence, the quantum transport regime has $l_e >> \lambda_{db}$. In the ballistic regime, l_e is greater

than the dimension of the system. In other words, the particle moves with no collisions during its way through the structure. On the opposite side, a diffusive regimes takes place when the dimension of the system is much greater than l_e.

The system can also be characterized by a coherence length, l_ϕ, where the wave-function phase is preserved and the quantum mechanical description endures. If it is smaller than the dimension of the system, the coherence is lost during the carrier transport and the classical picture is recovered.

3.1 Ballistic transport

The sample dimensionality being much smaller than l_e characterizes a ballistic transport regime. In this regime, the conductance depends on the band structure and on the device geometry. According to Landauer, [29] the current is proportional to the transmission probability of an electron [30], related to the linear response of the conductance. A ballistic conductor has its transmission probability close to the unity value which could lead to an infinite current, not observed in experiments. In what follows, we are going to discuss this controversial result and also derive the conductance formula for this regime.

Lets consider a quantum point contact, i. e. a conductor between two contacts, with length L and width d. Assuming a conductor operating in the Ohmic regime, the reduction of L would generate a infinite conductance, G. However, experiments show that G has a limited value when $L << l_e$. This resistance is explained due to the interface between the conductor and the contacts. The contacts have infinite transverse modes while the conductor has only a few modes. At the interface, a redistribution to balance this difference appears as a resistance.

The states that characterize the conductor belong to different subbands $(\mathcal{E}(n,k))$, where $\mathcal{E}_n = \mathcal{E}(n,0)$ is the minimum of the subband n. Thus, below $\mathcal{E}_1$, the channel is closed and $G = 0$. At a given energy, $\mathcal{E}$, the number of subbands is

$$N(\mathcal{E}) = \sum_N \vartheta(\mathcal{E} - \mathcal{E}_n). \tag{3.1}$$

Evaluating the current for only one band with an occupation function $f(\mathcal{E})$, yields

$$I = \frac{e}{L} \sum_k v f(\mathcal{E}), \tag{3.2}$$

where $\frac{f(\mathcal{E})}{L}$ is related to electron density. Then, replacing $v = \frac{1}{\hbar}\partial\mathcal{E}/\partial k$, assuming periodic boundary conditions, and converting the sum over k to an integral, $\sum_k \to 2\int \frac{L}{2\pi}dk$, one has

$$I = \frac{2e}{h}\int_{\mathcal{E}_n}^{\infty} f(\mathcal{E})d\mathcal{E}. \tag{3.3}$$

For one occupied state, $I = \frac{2|e|}{h}$, and for a multi-mode system

$$I = \frac{2e}{h}\int_{-\infty}^{\infty} f(\mathcal{E})N(\mathcal{E})d\mathcal{E}. \tag{3.4}$$

In order to calculate the conductance of the system with an applied voltage, $\Delta V = (\mu_1 - \mu_2)$, between the contacts where $\mu_1 > \mathcal{E} > \mu_2$, and assuming $N(\mathcal{E})$ constant, the current becomes

$$I = \frac{2e^2}{h}N\frac{\Delta V}{e}, \tag{3.5}$$

which leads to

$$G = \frac{2e^2}{h}N. \tag{3.6}$$

The result above provides a resistance, G^{-1} that, as an extensive magnitude, is inversely proportional to the number of modes N (or the lateral size of the system). For a infinity number of modes in the conductor $G^{-1} \to 0$, while for one mode $G^{-1} = 12.9K\Omega$.

The Landauer formula includes the fact that small conductors have a resistance due to interfaces and that the conductance depends on the transverse modes, number of subbands, but also on the average probability of the electron to be transmitted, T, $G = \frac{2e^2}{h}N \cdot T$. When $T = 1$, the conductance of the ballistic regime is recovered.

3.2   Quantum tunneling

The Quantum Mechanics wave-like description provides information about the probability amplitude of position, momentum, and other physical properties of a particle. This probabilistic nature predicts the tunneling effect of an electron through a potential barrier; in other words, there is a non zero probability for this effect happened. On the contrary, in the Classical Mechanics, a confined electron does not pass a potential barrier unless its energy overcomes the latter.

This Quantum Mechanical effect made possible the discovery of the tunnel diode by L. Esaki [31], which gave rise to a revolution in electronic and theoretical fields. In what

follows, a theoretical description of these systems will be presented.

3.2.1 Transfer Matrix Method

To characterize carrier transport properties in 1D superlattices, a method based on the formalism of multibarrier tunneling was developed: the Transfer Matrix Method (TMM) [83]. Therefore, the 1D time-independent Schrödinger equation must be solved for the the rectangular potential profile, V, as shown in Fig. 3.1, ergo

$$-\frac{\hbar^2}{2m^*(x)}\frac{d^2\Psi(x)}{dx^2} + V(x)\Psi(x) = \mathcal{E}\Psi(x), \tag{3.7}$$

where m^* is the effective mass and $\mathcal{E}$ is the energy. The general solution of Eq. (3.7) can be expressed as

$$\Psi_j(x) = A_j e^{ik_j x} + B_j e^{-ik_j x}, \tag{3.8}$$

where $k_j = \sqrt{2m^*(\mathcal{E} - V)}/\hbar$ is imaginary inside the barriers and real within the wells regions.
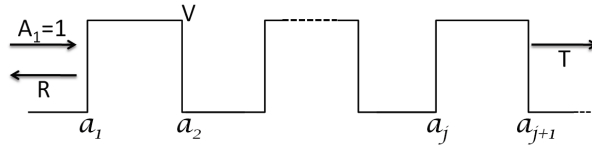
Fig. 3.1: Schema of the potential profile.

Considering the boundary conditions at the a_j interface and rewritten the solution of Eq. (3.8) as a vector product one have

$$M_j(a_j)\begin{pmatrix} A_j \\ B_j \end{pmatrix} = M_{j+1}(a_j)\begin{pmatrix} A_{j+1} \\ B_{j+1} \end{pmatrix}, \tag{3.9}$$

where

$$M_j(a_j) = \begin{pmatrix} e^{ik_j a_j} & e^{-ik_j a_j} \\ \frac{ik_j}{m_j^*}e^{ik_j a_j} & \frac{-ik_j}{m_j^*}e^{-ik_j a_j} \end{pmatrix}$$

.

Thus, one can relate the particle flux that leaves an interface with the flux of incident

particles for any number of barriers, through the transmission coefficient,

$$
\begin{pmatrix} A_1 \\ B_1 \end{pmatrix} = \prod_{j=1}^{n} M_j(a_j)^{-1} M_{j+1}(a_j) \begin{pmatrix} A_{n+1} \\ B_{n+1} \end{pmatrix} \tag{3.10}
$$

where n is the number of the interfaces (twice the number of barriers) and the product is the Transfer Matrix

$$
\mathbf{M} = \frac{1}{2} \prod_{j=1}^{n} \begin{pmatrix} e^{-ia_j(k_j-k_{j+1})}v_+ & e^{-ia_j(k_j+k_{j+1})}v_- \\ e^{ia_j(k_j+k_{j+1})}v_- & e^{ia_j(k_j-k_{j+1})}v_+ \end{pmatrix},
$$

where $v_\pm = \left(1 \pm \frac{k_j m_{j+1}^*}{m_j^* k_{j+1}}\right)$. Considering just the left to right incident wave, where the incident amplitude is $A_1 = 1$, the reflection amplitude is $B_1 = R$, and the right-left incident amplitude is $B_{n+1} = 0$; one can calculate the transmission coefficient, T, related to the transmitted amplitude A_{n+1} by $T = |A_{n+1}|^2$, $T = \frac{1}{|M_{11}|^2}$, and the reflection coefficient, $R = \frac{|M_{21}|^2}{|M_{11}|^2}$.

The net tunneling current can be calculate through

$$
J = \frac{e}{4\pi^3\hbar} \int_0^\infty dk_l \int_0^\infty dk_t [f(\mathcal{E}) - f(\mathcal{E}')] T \frac{\partial \mathcal{E}}{\partial k_l}, \tag{3.11}
$$

where $k_{t/l}$ is the transverse/longitudinal momentum. Due to the system planar geometry the transmitted coefficient depends only on k_t, since k_t is conserved. Thus, performing the integral over k_t, one have

$$
J = \frac{em^*}{\beta 2\pi^2\hbar^3} \int_0^\infty d\mathcal{E}_l Ln \left[\frac{1 + e^{\beta(\mathcal{E}_f - \mathcal{E}_l)}}{1 + e^{\beta(\mathcal{E}_f - \mathcal{E}_l - eV)}} \right] T, \tag{3.12}
$$

where $\mathcal{E}_f$ is the fermi energy and V is the bias voltage applied in the system. For $\beta \to \infty$ (temperature$\to 0$),

$$
J = \frac{em^*}{\beta 2\pi^2\hbar^3} \int_0^{\mathcal{E}_f} d\mathcal{E}_l (\mathcal{E}_f - \mathcal{E}_l) T, \qquad eV \geq \mathcal{E}_f \tag{3.13}
$$

$$
J = \frac{em^*}{\beta 2\pi^2\hbar^3} \left(\int_0^{\mathcal{E}_f - eV} d\mathcal{E}_l(eV) T + \int_{\mathcal{E}_f - eV}^{\mathcal{E}_f} d\mathcal{E}_l(\mathcal{E}_f - \mathcal{E}_l) T \right), \quad eV \leq \mathcal{E}_f \tag{3.14}
$$

3.3 Hopping

A model based on hopping transport can describe the temperature dependence of the carriers mobility through a system involving localized states, suitable for describing charge transfer in quantum dot chains. [32, 33, 34, 35, 36] This is a semiclassical theory determined by inelastic transitions of electrons from full states to neighboring empty states assisted by phonons. Localized states are centered on fixed sites between which the transitions take place. In what follows, a rate equation formalism will be developed that accounts for this kind of process.

Assuming an array on N sites occupied by one electron in an applied electric field, where n_k is the probability of the site k being occupied, one can write the system of rate equations

$$\frac{dn_k}{dt} = \sum_n [n_l(1 - n_k)R_{lk} - n_k(1 - n_l)R_{kl}], \tag{3.15}$$

where R_{kl} in the transition rate from a full site, k, to an empty site, l.

In a system on uniform thermal equilibrium, the occupation density is given by the Fermi-Dirac distribution

$$n_k^0 = \frac{1}{1 + e^{\beta(\mathcal{E}_k - \zeta)}}, \tag{3.16}$$

where $\beta = (k_b T)^{-1}$, k_B is Boltzmann's constant, $\zeta = \mu + k_b T \ln(2)$, $\ln(2)$ due to spin degeneracy, $\mathcal{E}_k$ is the hopping energy state, and μ the Fermi energy. Moreover, in Eq. (3.15) at equilibrium, $\frac{dn_k}{dt} = 0$, in this way,

$$\frac{R_{kl}^0}{R_{lk}^0} = e^{\beta(\mathcal{E}_k - \mathcal{E}_l)}. \tag{3.17}$$

Applying a small external potential field, $U(\mathbf{r}, t)$, one can rewrite the energies as $\mathcal{E}_{k,l} = \mathcal{E}_{k,l} + U_{k,l}$, where

$$\frac{R_{kl}}{R_{lk}} = \frac{R_{kl}^0}{R_{lk}^0}(1 + \beta(U_k - U_l)). \tag{3.18}$$

In this approach, n_k suffers a perturbation, $n_k = n_k^0 + n_k^1$, leading to a linearized system of rate equations

$$\frac{dn_k^1}{dt} = \sum_n [n_l^1 R_{lk}^e - n_k^1 R_{kl}^e] + \beta \sum_n [F_l U_l R_{lk}^e - F_k U_k R_{kl}^e], \tag{3.19}$$

where $R_{kl}^e = \Gamma_{kl}/F_k$ with $\Gamma_{kl} = n_k^0(1 - n_l^0)R_{kl}^0$, and $F_k = n_k^0(1 - n_k^0)$.

According to Miller and Abrahams [32], the transition rate for hops from one site to another with relative position vector $\mathbf{r}_{kl}$ is given by

$$R_{kl} = \left\{ \begin{array}{l} \nu_0 e^{-a|\mathbf{r}_{kl}|-\beta(\mathcal{E}_l-\mathcal{E}_k)}, \mathcal{E}_l > \mathcal{E}_k \nu_0 e^{-a|\mathbf{r}_{kl}|}, \qquad\qquad \mathcal{E}_l < \mathcal{E}_k \end{array} \right. \qquad (3.20)$$

where ν_0 is an intrinsic transition rate, $a = 2/\alpha$ with α being the localization radius, and $\mathcal{E}$ is the energy which includes the contribution of U. Therefore, the mobility can be calculated as

$$\mu_\xi \quad = \quad \frac{r_0}{\mathbf{E} < n_k^0 >} \sum_k \sum_l \left[\mathbf{r}_{kl} R_{kl}^{(\xi)} n_k (1 - n_l) + \mathbf{r}_{kl} R_{kl}^{(\xi)} n_l (1 - n_k) \right], \qquad (3.21)$$

where $\mathbf{E}$ is an applied electric field, r_0 is the lattice constant, and n_k^0 is the equilibrium Fermi-Dirac distribution (r_{kl} and α are given in units of r_0).

The quantum and semiclassical models developed here will be fundamental for the electronic transport description in quasi-1D heterostructures problems described below.

4. HOMOGENEOUS NANOWIRES

The importance of semiconductor NWs is related to their appearance as building blocks in a wide range of nanoscopic devices. As described before, progress in NW synthesis, including chemical technics, allows a thorough control of their shape, size, and composition [5, 6, 7, 8, 9] along with detailed microscopic characterization of built-in strain fields. [9, 84] As the conductivity is mostly defined by the carrier-phonon interaction and phonon-lifetime, tuning the NW structural properties could result in the possibility of finding optimal conditions for carrier transport.

Considerable efforts have been devoted to the description of carriers in the conduction band of NWs, [37, 38, 39, 40, 41, 42, 43] while similar endeavors are not so common for holes in the valence band. [44] As the mobility is inversely proportional to the carrier effective mass, one may naturally expect that considering carriers in the valence band may result in a drop in mobility when compared to the light electrons in the conduction band. This could certainly be the case for heavy-holes (HH) transport; however, light-holes (LH) under certain conditions may be promoted to be the top valence band by tuning structural parameters of NWs, as calculated on Chapter 2. [27] This atypical circumstance is the result of confinement effects and HH-LH mixing, affected as well by strain and the presence of surfaces. [9, 27] As we will show here, this results in significant mobility enhancement for LH in suitable NWs. We can also take advantage of valence band mass anisotropy to attain resonant conditions that allow sharp variations of the hole mobility with external parameters, especially when the leading scattering process involve LO-phonons through the deformation potentials. [45] Additional hole-phonon interactions, [85] such as deformation potential and piezoelectric coupling to acoustic phonons and polar coupling to optical phonons, [86] have weaker effects and will not be considered here. [85, 80] In order to provide realistic estimates of the expected mobility changes in the NWs of interest, we consider the effects of dimensionality reduction on the LO-phonon dispersion and lifetime, using MD simulations for different NWs size and at various temperatures.

Tab. 4.1: The parameters of the InP interaction potential. Z_i is the effective ionic charge, and α_i the electronic polarizability. η is the steric repulsion exponent, W_{ij} is the van der Waals strength, and H_{ij} is the strength of the steric repulsion. $B_{jik} = 4.1744$ is the three-body strength, $\lambda_1 = 4.5\mathring{A}$ and $\lambda_4 = 2.75\mathring{A}$ are the screening lengths for Coulomb and charge-dipole interactions, while $r_c = 6\mathring{A}$ is the two-body cutoff radius; $r_0 = 3.55\mathring{A}$, $\theta_{jik} = 109.47°$, and $C_{jik} = 10$ are the three-body range, bond angle and saturation parameter, respectively.

	$Z_i\,(e)$	$\alpha_i\left(\mathring{A}^3\right)$
In	1.1575	0
P	-1.1575	6

	η	$W_{ij}\left(eV\mathring{A}^6\right)$	$H_{ij}\left(eV\mathring{A}^\eta\right)$
In-In	7	0	97.6585
In-P	9	251.4607	5009.8747
P-P	7	0	3830.8784

These latter effects were characterized by the group of Prof. Jose P. Rino from UFSCar, and the results used as input parameters for the subsequent calculation of the hole-phonon interaction terms.

To describe the effect of NW shape on the hole wavefunction, we consider different cross sections, shapes, while temperature effects are included in the mobility calculation through the phonon occupation and strain effects in a multiband Luttinger Hamiltonian.

4.1 Molecular dynamics simulations

The interaction potentials used in the MD simulations consist of two- and three-body interaction terms, as described by Branicio *et al.* [87, 88, 89, 90, 91] The two-body term is composed of the Coulomb interaction due to charge transfer between ions, a steric repulsion due to size effects, a charge-induced dipole due to the electronic polarizability of ions, and a van der Waals attraction. The three-body contribution is necessary to describe the covalent character of the bonds and applies to groups of atoms which are connected by cohesive interaction. The parameters of the interatomic potential are determined using the cohesive energy, density, bulk modulus and elastic constant C_{11} of the material as described before, [91] with some slight adjustments, as presented in Table 4.1.

This potential provides excellent estimates for melting temperature, structural phase transformation induced by pressure, and specific heat [88] and it is also suitable to describe

the vibrational density of states of the material, as one will see below. Within this model the phonon density of states in InP NWs at different temperatures was obtained. The NWs are simulated cutting a block of a perfect crystal with the z-axis along the [001] direction; periodic boundary conditions are applied in the z-direction. The x- and y-directions are surrounded by a vacuum region much larger than r_c. The system consisted typically of nine unit cells along x- and y-directions and forty unit cells along the z-direction ($53\text{\AA} \times 53\text{\AA} \times 234.5\text{\AA}$); the total number of atoms is 25,920 (12,960 In + 12,960 P) (Fig. 5.1). The NW is allowed to relax during a long simulation run (25,000 time steps, one time step=1.5fs) at each temperature. After this relaxation time, a few surface defects can be observed (Fig. 5.1(b)).
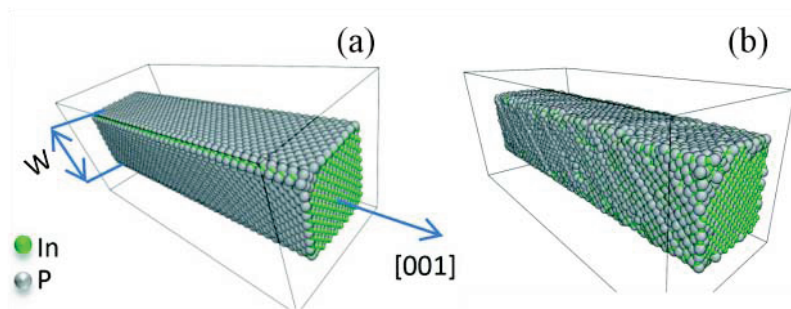
Fig. 4.1: Simulated InP NW structure by molecular dynamics. Green (grey) dots represent Indium (Phosphorous) atoms and W is the NW width. (a) T=10 K and (b) $T = 300$ K.

The velocity-velocity auto correlation function is defined by

$$Z_i\left(t\right) = \frac{\langle \vec{v}_i\left(t\right).\vec{v}_i\left(0\right)\rangle}{\langle \vec{v}_i\left(0\right).\vec{v}_i\left(0\right)\rangle}, \tag{4.1}$$

where $\vec{v}_i\left(t\right)$ is the velocity of particle i at time t and the brackets are averages over ensembles and particles. The vibrational phonon density of states (VDOS) is determined through the Fourier transform [92]

$$G_i\left(\omega\right) = \frac{6N_i}{\pi} \int_0^\infty Z_i\left(t\right) \cos\left(\omega t\right) dt, \tag{4.2}$$

where the subindex i is the atom In or P.

Figure 4.2(a) compares the VDOS computed from MD calculations for a bulk system (solid curve) to the VDOS extracted from the rigid ion model (dashed curve) based on experimental results [93, 94]. As one can observe in Fig. 4.2(a), the results from MD reproduce very well the main characteristics of the experimental results by predicting

the existence of the transversal optical (TO, $\sim$ 43 meV) and longitudinal optical (LO, $\sim$ 38 meV) modes, and a gap between 22 meV and 36 meV.

The effect of the surfaces on the VDOS of the NW is also shown in Fig. 4.2. The main NW characteristics in the VDOS resemble the bulk results; however, some differences can be observed. The NW surfaces appreciably increases the amount of modes in the gap region, between 22 meV and 36 meV. Although the TO and LO modes are the dominant ones, the NW surface play an important role by inducing surface modes that appear in the gap region. To extract more information about the origin of the modes, the VDOS contribution from different atoms was separated. Thus, in Fig. 4.2(b) (Fig. 4.2(c)) the partial VDOS for bulk and the NW, considering the Indium (Phosphorus) contribution, are depicted. By comparing Fig. 4.2(b) to Fig. 4.2(c), we notice that the P atoms give the main contribution to the optical modes in the gap, a larger VDOS, and an overall large mode width for the NW. The optical modes are characterized by the relative displacement between ions and the lighter atoms usually dominate such modes, as shown in Figs. 4.2(b)-(c). Moreover, one can observe in Fig. 4.2 a slight blue shift of the LO mode ($\sim$ 1 meV) with respect to the bulk.

The effect of temperature on the VDOS for both NW and bulk structure is shown in Fig. 4.3. A general broadening of the modes and a shift in the peaks position to lower frequencies with increasing temperature can be observed. Although the gap region keeps a similar profile, the VDOS in the gaps increase with temperature. We notice also that the temperature affects the contrast between LO and TO modes, especially in the NW, Fig. 4.3(b), by slightly increasing the LO width.

Notice that the mode broadening is slightly weaker for the NW than for the bulk. Based on the MD results, one verifies that the TO and the LO modes are the most important vibrational modes and the surface modes can be disregarded in a first approximation to the mobility calculation. Also, the effects of the temperature in the NW reveal a shift in the LO mode, which is an important fact to be considered when calculating the contribution of hole-phonon scattering to the mobility.
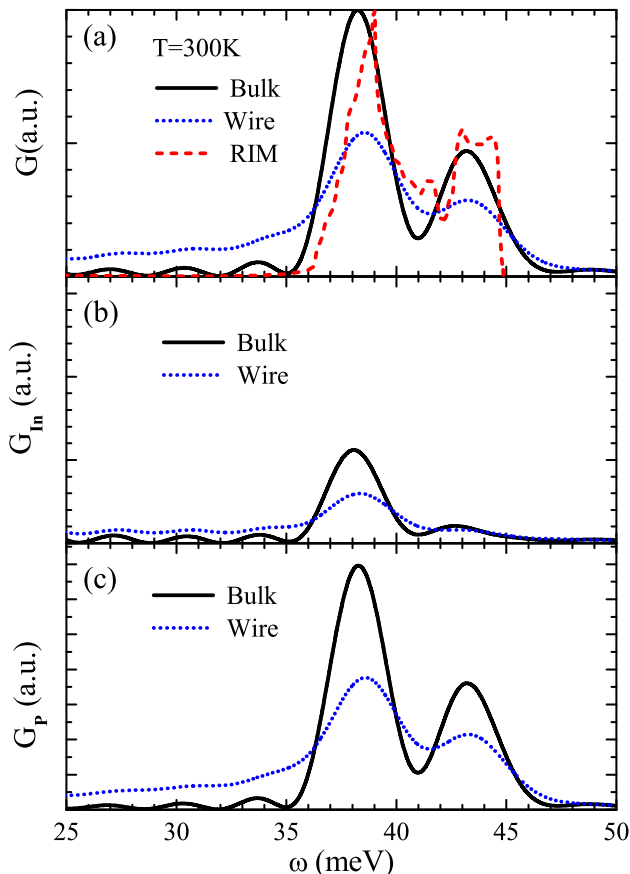
Fig. 4.2: VDOS for NW and bulk InP. (a) Total VDOS; rigid ion model (RIM) VDOS for bulk from data.[94] (b) and (c) Partial VDOS for bulk and NW at 300 K: (b) indium contribution and (c) phosphorus contribution

4.2 The valence band calculation and hole mobility

As already discussed, the valence band Hamiltonian for the NW can describe confinement effects, mass anisotropy, and strain fields within the same framework, with [72]

$$\mathcal{H}_{HH} = -\left(\frac{\gamma_1 + \gamma_2}{2}\right)\{\hat{k}_+, \hat{k}_-\} - \left(\frac{\gamma_1 - 2\gamma_2}{2}\right)\hat{k}_z^2, \qquad (4.3)$$

and

$$\mathcal{H}_{LH} = -\left(\frac{\gamma_1 - \gamma_2}{2}\right)\{\hat{k}_+, \hat{k}_-\} - \left(\frac{\gamma_1 + 2\gamma_2}{2}\right)\hat{k}_z^2, \qquad (4.4)$$

for the heavy- and light-holes, where γ_α ($\alpha = 1, 2, 3$) are the Luttinger parameters, $\{A, B\} = \frac{1}{2}(AB + BA)$, and $\hat{k}_\pm = \hat{k}_x \pm i\hat{k}_y$. Notice that the subband with HH character along the wire has a *low* effective mass in the transverse direction $\approx (\gamma_1 + \gamma_2)^{-1}$, while the LH subband has a *large* transverse mass $\approx (\gamma_1 - \gamma_2)^{-1}$; as described before, the different transverse masses result in the possible inversion of the LH and HH sub-
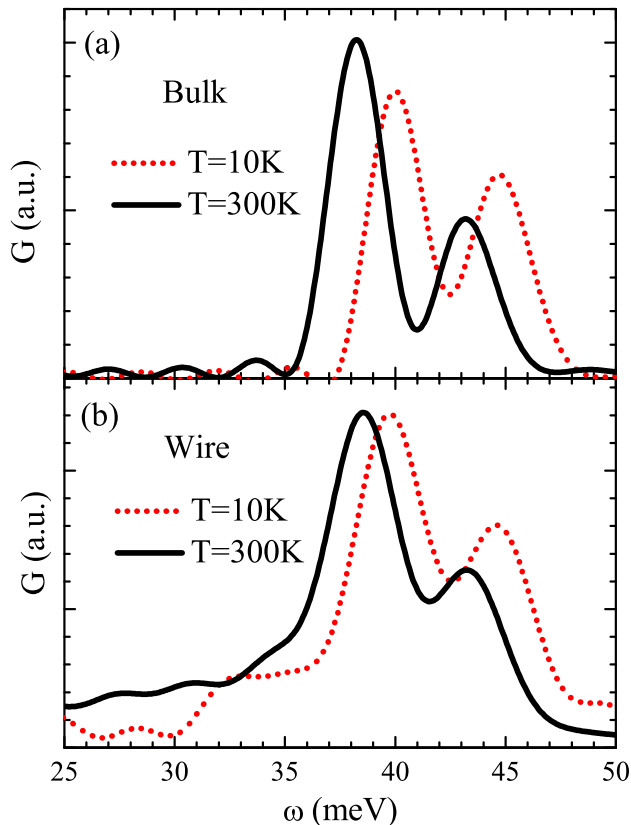
Fig. 4.3: VDOS for bulk and NW at 10 K and 300 K. In (b) the NW results at T=10 K shown
that surfaces introduce new states in the region of gap and at T=300 K further increases
new states.

band ordering, due to the NW confinement effects. Strain effects lead to modulation of
the valence subbands, [9] introducing a subband displacement given by Eq. (2.30) and
Eq. (2.30). [76]

The mobility is given by $\mu = \frac{e}{m_0 \lambda_{z\beta}} \tau$, in terms of the hole-phonon scattering time, τ,
obtained on Eq. (2.49). The phonon density was assumed to be given by a Lorentzian
centered at ω_{LO} with width Γ. Both of these values shift with temperature, as discussed
in the first section of this Chapter and we may now analyze the effects of strain and
temperature on the hole mobility.

4.3   Results and discussion

To characterize the initial and final states involved in the scattering processes that
affect the mobility, Fig. 4.4 shows the relevant valence band structure for two different
cases. For thin NWs, with or without strain, the finite NW width leads to a picture similar
to Fig. 4.4(a), where the LH subband is promoted to the top given its higher transverse
effective mass, as discussed before. Thus, under such conditions, a HH can be scattered

to the subband with LH character through phonon emission (process E_1), and at $T > 0$ the LH can be excited to the HH subband via phonon absorption (process A_1). In the presence of lateral compressive strain, the subbands may switch their relative positions with the HH assuming the top at large NW width. Then, a LH might be scattered via phonon emission (process E_2) while a HH can be affected by phonon absorption at $T > 0$ (process A_2). Fig. 4.4(c) shows the energy difference between the ground state and the first excited state ($\Delta\mathcal{E}_{vb}$) without strain, this remains for intersubband transitions with the profile in Fig. 4.4(a), where the ground state is always the LH subband. In this sense, by changing the wire radius one can reach a resonant condition ($\Delta\mathcal{E}_{vb} = \hbar\omega_{LO}$). On the other hand, with strain, depending on the value of the NW width, the ground state can have a character LH (thin NW) or HH (thick). This may result in reaching the resonant condition twice (Fig. 4.4(d)). This behavior is similar for all NW cross sections since it affects the transversal quantization.
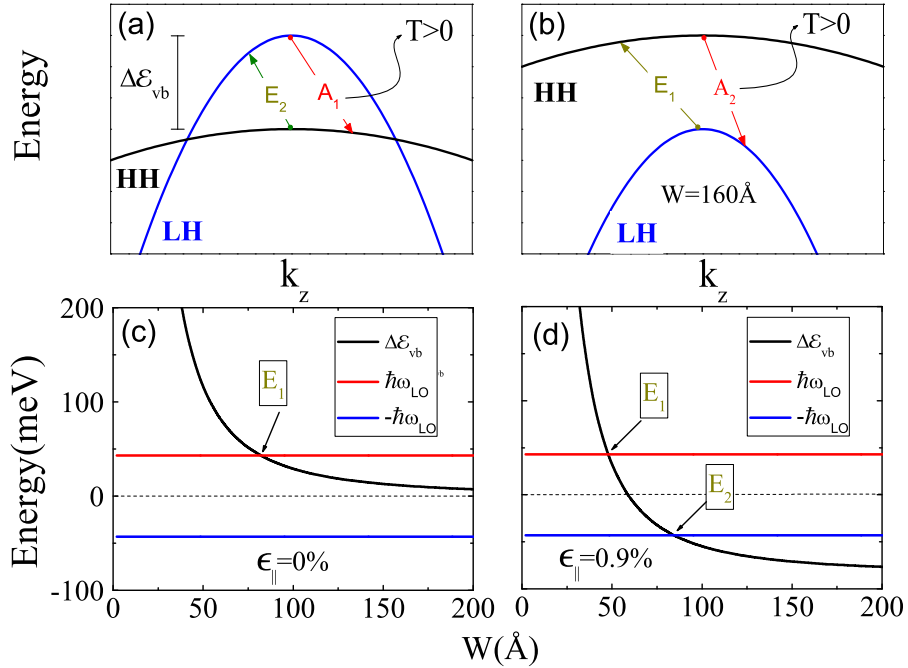
Fig. 4.4: Valence band ground states for square cross section NW of width W. (a) When the LH occupies the ground state, a HH is scattered by phonon emission (process E_1) while a LH is affected by phonon absorption at $T > 0$ (process A_1). (b) When the HH occupies the ground state, a LH is scattered by phonon emission (process E_2) and the HH is affected by phonon absorption at $T > 0$ (process A_2). (c) Energy difference between the ground state and the first excited state ($\Delta\mathcal{E}_{vb}$), at $k_z = 0$, versus NW width without strain, $\Delta\mathcal{E}_{vb} = \mathcal{E}_{LH} - \mathcal{E}_{HH}$; in this case the ground state is always the LH subband. (d) System with strain; depending on the value of the NW width, the ground state is the LH (thin NW) or HH (thick NW) subband.
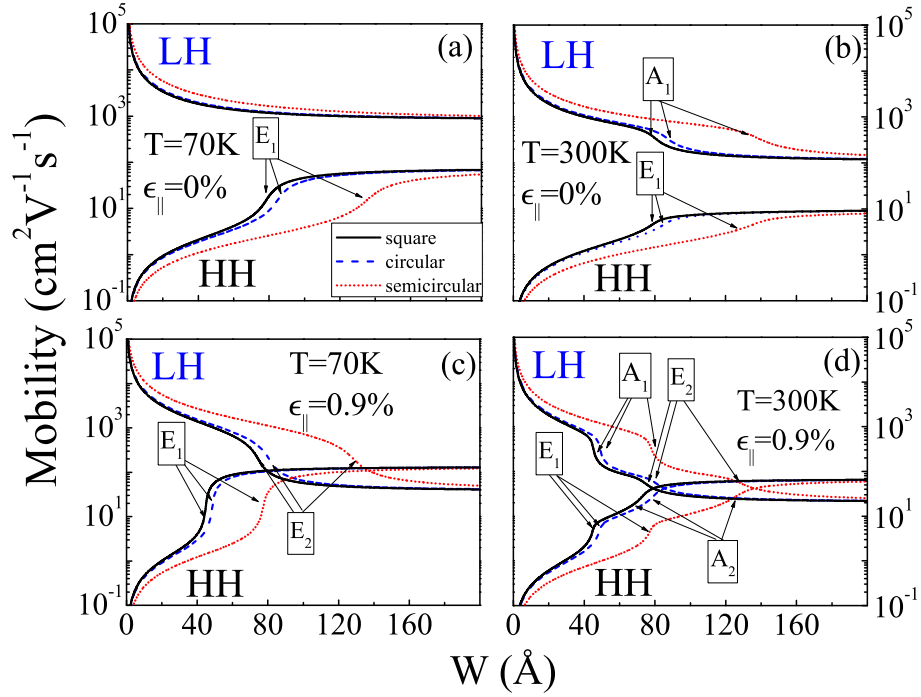
Fig. 4.5: Hole mobility versus NW width W for states with $k_z = 0$. (a) System at T= 70 K without strain. (b) System at T= 300 K without strain. (c) System at T= 70 K with strain ($\epsilon_{||} = 0.9\%$). (d) System at T= 300 K with strain ($\epsilon_{||} = 0.9\%$). Notice, the onset of resonant A and E processes results in sharp changes in mobility with W.

The relative position of the valence subbands is extremely important for the carrier transport in NWs. Given the mobility dependence on the longitudinal effective mass, which modulates the hole-phonon interaction, valence subbands shifts may produce sharp fluctuations of the mobility as temperature or structural parameters change. Fig. 4.5 shows the mobility for different strain and temperature values as function of the NW width. In Figs. 4.5(a) and (b), the mobility reflects a band configuration similar to the one depicted in Fig. 4.4(a). At T= 70 K, in Fig. 4.5(a), the enhanced effect of phonon absorption leads to the monotonic decrease of the LH mobility with increasing NW width. In turn, the HH displays a monotonic mobility increase, as the intersubband separation decreases with increasing NW width. Also, a sharp variation near the region where $\Delta\mathcal{E}_{vb} \sim \hbar\omega_{LO}$ is seen, the resonant condition greatly enhances the LO-phonon emission by a HH in Panel (a). At higher temperatures, Fig. 4.5(b), when thermal phonons are present in large numbers, the resonant condition also affects the carriers in the LH subband, producing a sharp drop in mobility (triggered by A_1 processes).

Given the band structure modulation with strain, the condition $|\Delta\mathcal{E}_{vb}| \sim \hbar\omega_{LO}$ can be attained twice by varying the NW width (corresponding to the cases displayed in

Figs. 4.4(a) and (b)). Thus, two resonant regions appear in Fig. 4.5(c) where phonons can be emitted by both the HH and LH subbands (E_1 an E_2 processes, respectively). At higher temperatures, the phonon absorption features appear as additional jumps in the mobility picture shown in Fig. 4.5(d), processes A_1 and A_2. Notice that the LH and HH subband inversion with increasing NW width, in the presence of strain, is accompanied by crossing of the mobility curves, Figs. 4.5(c) and (d).
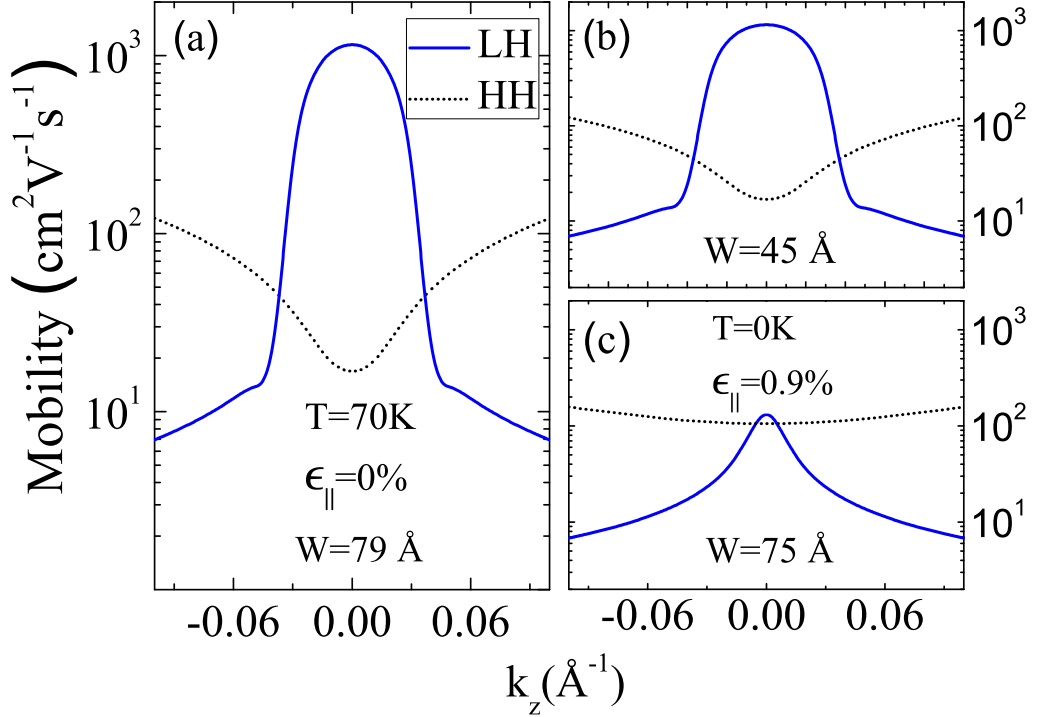
Fig. 4.6: Hole mobility in a square cross section NW versus hole momentum at T= 70 K. (a) without strain. (b) and (c) with strain . In each case, the NW width was chosen so as to provide the resonant condition when $\Delta\mathcal{E}_{vb} = \hbar\omega_{LO}$.

The results shown so far describe the mobility of carriers at the center of the Brillouin zone, with $k_z = 0$. However, transport carriers may have finite k_z values, corresponding to higher Fermi energies. To explore the effect of increasing hole momentum, Fig. 4.6 shows the hole mobility as function of k_z for two values of strain. The NW width has been chosen to meet the resonant condition, where the subband tops are separated by the energy of one LO-phonon ($\Delta\mathcal{E}_{vb} = \hbar\omega_{LO}$). Thus, the minimum obtained for the HH mobility in Figs. 4.6(a) and (b) and the maximum for the LH in Fig. 4.6(c) are induced by resonant phonon emission processes. Notice, in Fig.s 4.6(a) and (b), that the carrier mobility changes rapidly for a certain value of k_z, corresponding to the subband crossing where the valence band ground state changes character. Under strain, at the NW size in Fig. 4.6(c), the crossing results in much smoother variation of the mobility with k_z.

Although it is interesting to consider the possibility of tuning the mobility of a hole system via in-situ changes of the NW strain fields, this is not an easy experimental task. As we will see below, however, one can achieve drastic in-situ mobility changes for NWs close to the resonance condition by suitable changes in temperature.
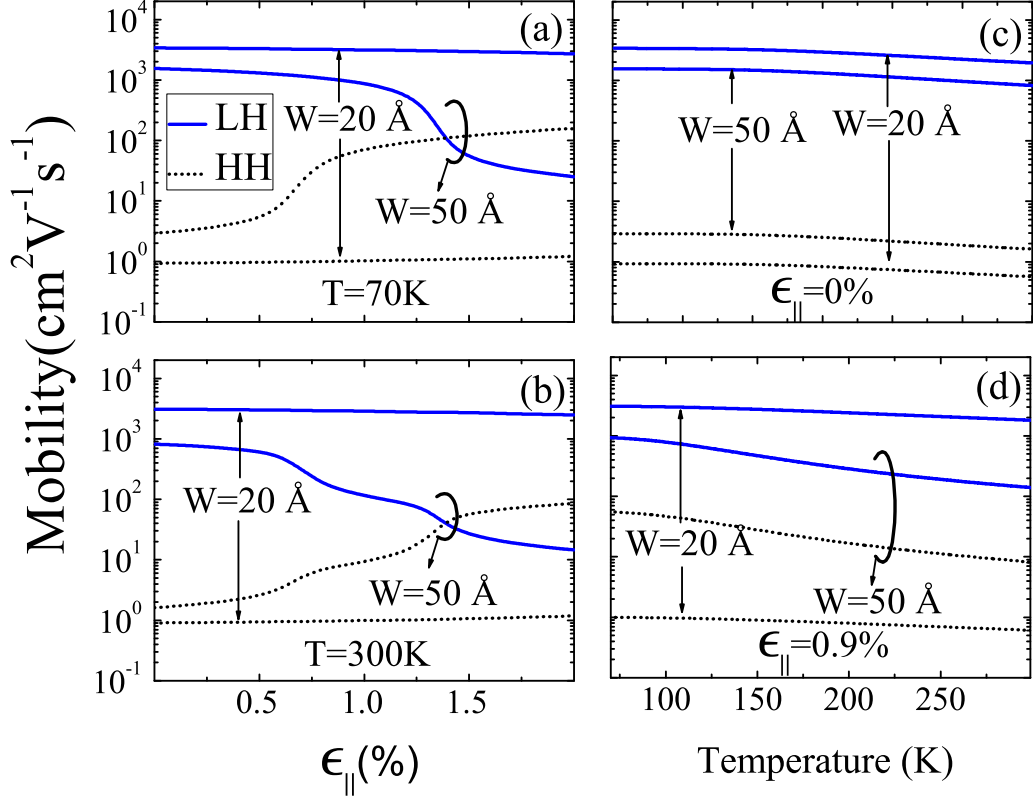
Fig. 4.7: Hole mobility for two values of NW width for states with $k_z = 0$: (a) and (b) as function of strain for T= 70K and T= 300K, respectively, and (c) and (d), as function of temperature for $\epsilon_{||} = 0\%$ and $\epsilon_{||} = 0.9\%$, respectively.

To study how the carrier mobility changes due to the continuous variations of strain and temperature, we show results for two values of the NW width. In Fig. 4.7 for a square NW width of W= 20Å, no resonant signatures appear in the strain and temperature range analyzed, while for thicker NWs such conditions become evident for both kind of holes. This situation follows the trends described in Fig. 4.4, since for thinner NWs, the valence band configuration corresponds to that presented in Fig. 4.4(a), with $\Delta\mathcal{E}_{vb} > \hbar\omega_{LO}$. In turn, by rising the temperature, the process of phonon absorption becomes more efficient, reducing the LH mobility at higher temperatures; as displayed in Figs. 4.7(c) and (d), such effect is present for all the NWs, although with different features for various W values, as we now discuss.

Figure 4.8 shows the strong non-monotonic mobility variation with temperature for

certain NW widths with energies close to the resonant condition, $\Delta\mathcal{E}_{vb} \simeq \hbar\omega_{LO}$. This figure shows the LH mobility ratio of high and low temperatures, $\Delta\mu_{LH}/\mu_{LH}[70\ \text{K}]$, where $\Delta\mu_{LH} = (\mu_{LH}[70\ \text{K}] - \mu_{LH}[300\ \text{K}])$, as function of the NW width for different values of strain. For LH, the mobility at low temperatures is high (Fig. 4.7(c)-(d)) and according to the radius and strain one can observe a drastic or minimal change at high temperatures. For a system with no strain, for example, a large but monotonic change in the mobility is seen for NWs with large width (larger than 100Å). In real systems, however, free standing NWs grow with built-in strain, [9] which has a direct impact on the dependence of μ on the temperature and width. As the strain increases, the LH-HH subband reversal is possible as the NW width grows, resulting in highly sensitive mobility on temperature and/or width. For example, for the reported value, $\epsilon_{\parallel} = 0.9\%$ [9], one can see that a range of ideal width values, between 50Åand 60Å, exhibits a sharp change in the mobility with temperature.
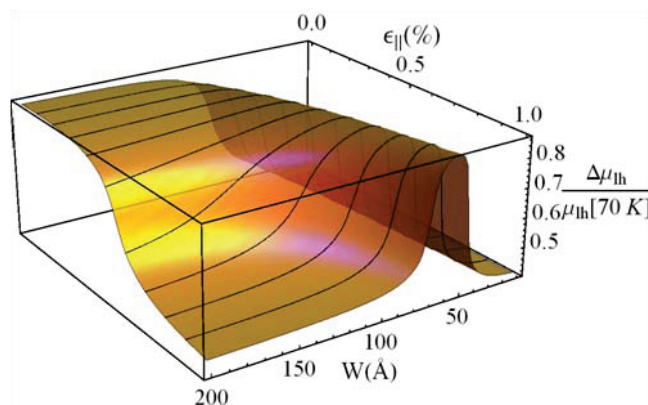
Fig. 4.8: Light hole mobility ratio, where $\Delta\mu_{LH} = (\mu_{LH}[70\ \text{K}] - \mu_{LH}[300\ \text{K}])$, versus wire width for different values of strain at $k_z = 0$.

4.4   Conclusions

In summary, we have presented the results of hole mobility behavior in InP semiconductor NWs for different geometries and under various strain and temperature conditions affected by the hole-phonon interaction. Using molecular dynamics with realistic force potentials, we simulated NW structures and calculated the associated phonon density of states. This allowed the characterization of the LO phonon energy renormalization due to the reduced dimensionality and variations of the phonon lifetimes at different temperatures, essential ingredients for the evaluation of carrier mobility. We have also emulated

the valence band structure with a model that includes the confinement and strain conditions, calculated on Chapter2.

We showed that the mobility changes according to the NW width, strain fields, and temperature in a non-monotonic fashion for certain parameters. In particular, we show that for certain NW widths, one finds resonant behavior that greatly suppresses the hole mobility. This is explained by the fact that the electronic structure changes drastically with strain and/or size, with the ground state switching character between heavy and light hole, while the temperature changes of the LO peak position and size are also important. Furthermore, we have characterized the resonant behavior of the mobility when the energy separation between the two valence subbands equals the optical phonon energy. These conditions can be tuned by size variation or strain fields and are also affected by temperature, and should be taken into careful consideration when designing possible NW-based device.

5. PARALLEL COUPLED NANOWIRES AND SPIN TRANSPORT

The realization of a directional coupler in the early 90's gave rise, through proximity and tunneling effects,[46, 47] to the modulation of quantum transport in a phase-coherent system.[48] Likewise, the spin modulation in a single NW via spin-orbit interaction (SOI) has been proposed [49] and refined [50, 51, 52, 53, 54] to achieve a spin-orbit quantum bit device. [19] Exploring all-electrical spin transport has motivated a search for new configurations of nanostructures [14, 15, 16, 17, 18]. Therefore, exploring the properties of coupled NWs in order to unveiled the nature of electron and spin transport mechanisms, a spin-wave guide directional coupler appears as a promising device geometry.

In this Chapter, we study the spin transport properties of parallel NWs, in a directional "H-shape" coupler geometry, connected through a region of the same material but locally gated, Fig. 5.1. The application of a gate field ($\mathbf{E}$) in the connecting region generates a Rashba SOI, which breaks spin degeneracy, [95] Fig. 5.2. While the Rashba field does not break time reversal symmetry, the symmetries of the configuration impose additional constraints on the transport characteristics. [54, 17, 96]

We find that, while being able to control the electronic flux through the different wires across the mixing region, as expected (section 2.4.1), it is also possible to electrically control the *spin flux* across the device, whenever spin-polarized injection is considered. Moreover, we find that there is a net spin-polarized flux perpendicular to the current, which can be controlled by the gate potential in the mixing region, as well as by local gates at the NWs. This overall control of charge and spin flux in a directional coupler appears promising for spintronics, as well as in hybrid devices composite with superconducting or magnetic materials. Furthermore, the transmission and reflection amplitudes (the entire scattering matrix) will be shown below and exhibit oscillations arising from the expected interference among the various channels, as they mix in the coupling region. This interference has characteristic energy (or length) scales associated with the different effects producing it. We will also see that the onset of spin-orbit coupling in the mixing

region further complicates the pattern of oscillations as SOI effectively duplicates the number of available channels at a given energy.
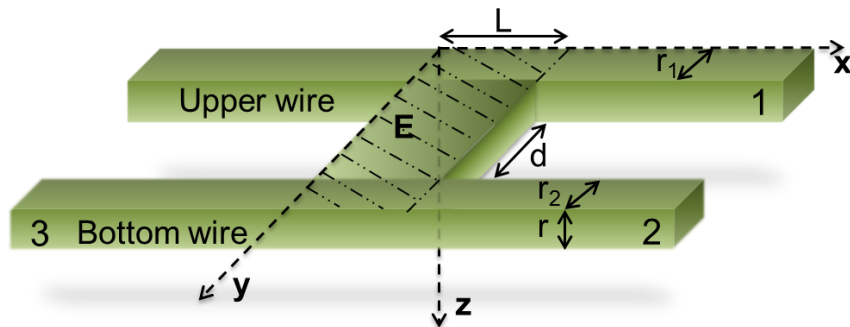
Fig. 5.1: Scheme of the proposed system where we have two parallel nanowires connected in a middle region by the same material. r_1 is the radius on the upper wire, r_2 in the radius of the bottom wire, d is the distance between the wires, L is the width of the middle region, and $\mathbf{E}(z)$ it is a electric fiel on the z-direction applied only in the middle region.

The Chapter is organized in the following way. The first section presents the exact solution for the electronic structure of confined states in the middle region with Rashba SOI. The second one, the solution for the whole system in terms of a Perturbation Theory is developed. The third section, the transmission end reflection probabilities of the system via the transfer matrix method, described before, are calculated. Finally, the results and discussion are presented in the last section.

5.1 Exact solution with Rashba interaction

The single-particle Hamiltonian with SOI on the (x, y) plane can be written as

$$\mathcal{H} = \frac{p^2}{2m^*} + V_c(y, z) + \frac{1}{2\hbar}[\alpha(\mathbf{r}) \cdot (\sigma_x p_y - \sigma_y p_x)]_{\hat{z}}, \qquad (5.1)$$

where $p_i = -i\hbar\nabla_j$, σ_i are the components of the Pauli matrices, $\alpha(\mathbf{r})$ is the SOI constant, and $V_c(y, z)$ is the hard wall confined potential in the y- and z-direction. This configuration can be achieved by applying external gates on the z-direction, perpendicular to the effective SOI plane.

Searching for solutions, the systems displayed in Fig. (5.1) required two different Hamiltonians. The first one refers to the wires with no SOI, since for vanishing $\alpha(\mathbf{r})$ the Hamiltonian (5.10) eigenvalue problem can be exactly solved. Thus, the solution for

a squared NW cross section is

$$|\phi_j^\sigma\rangle = \sqrt{\frac{2}{r_{1,2}}} \sin\left(\frac{n_y^j \pi y}{r_{1,2}}\right) \sqrt{\frac{2}{r}} \sin\left(\frac{n_z \pi z}{r}\right) e^{ik_x x} |\sigma\rangle, \tag{5.2}$$

where the index j refers to the upper (bottom) left wire UL (BL) or right UR (BR) branch, and $|\sigma\rangle$ is the spin.

In this section, the solution within the region which is referred as middle part, is sought. This region is similar to a Rashba 2D electron gas (2DEG) except for the fact that we do have a confinement in both directions, x and y. The strategy adopted here is finding the solution for the case with no confinement (Rashba 2DEG), then a hard wall boundary conditions will be considered. Consequently, for a system with no confinement, the wave-function with positive energy is

$$|\psi\rangle = e^{i(k_x x + k_y y + k_z z)} \begin{pmatrix} C^\uparrow \\ C^\downarrow \end{pmatrix}, \tag{5.3}$$

where $C^{\uparrow,\downarrow}$ are the spinors. Applying the Hamiltonian (5.10) in the non confined wave-function (5.2), $\hat{H}|\psi\rangle = \mathcal{E}|\psi\rangle$, leads to

$$\begin{pmatrix} \frac{\hbar^2}{2m}(k_x^2 + k_y^2 + k_z^2) - \mathcal{E} & \frac{i\alpha}{2}(-k_x + ik_y) \\ \frac{-i\alpha}{2}(k_x + ik_y) & \frac{\hbar^2}{2m}(k_x^2 + k_y^2 + k_z^2) - \mathcal{E} \end{pmatrix} \begin{pmatrix} C^\uparrow \\ C^\downarrow \end{pmatrix} e^{i(k_x x + k_y y)} = 0. \tag{5.4}$$

One can notice that the z-component of the wave-function is separable. Hence, the solution in the z-direction remains the same as with no SOI. To simplify the notation, the z-component solution will be omitted.

In other to solve the eigenvalue problem of Eq. (5.4) for the remaining components, more assumptions should be taken into account. Thus, considering the system energy constant and the x-component of the wave-vector positive (Fig. 5.2), two eigenvalues are obtained

$$\mathcal{E}_\pm = \frac{\hbar^2}{2m}(k_x^2 + k_y^2) \pm \frac{\alpha}{2}\sqrt{k_x^2 + k_y^2}, \tag{5.5}$$

with their correspondent eigenvectors being

$$|\psi\rangle = \frac{1}{\sqrt{2}} e^{ik_x x} \left[A e^{ik_+ \sin(\theta)y} \begin{pmatrix} 1 \\ -ie^{i\theta} \end{pmatrix} + B e^{ik_- \sin(\phi)y} \begin{pmatrix} 1 \\ ie^{i\phi} \end{pmatrix} + \tag{5.6}$$
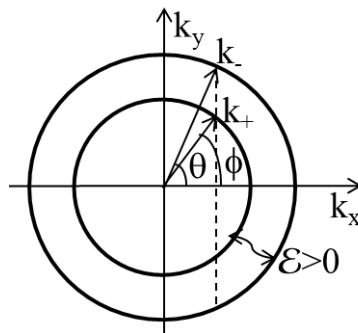
Fig. 5.2: Spectrum of the 2DEG with SOI at fixed positive energy ($\mathcal{E}$). For positive fixed x-component we address the four possible values of k_y ($k_- \sin(\theta)$, $k_+ \sin(\phi)$, $k_- \sin(-\theta)$, $k_+ \sin(-\phi)$).

$$Ce^{-k_+ \sin(\theta)y} \begin{pmatrix} 1 \\ -ie^{-i\theta} \end{pmatrix} + Be^{-ik_- \sin(\phi)y} \begin{pmatrix} 1 \\ ie^{-i\phi} \end{pmatrix} \Bigg].$$

The solution (5.6) is written in terms of the two spin modes ($+$ and $-$), where $k_y = k_- \sin(\theta) = k_+ \sin(\phi) = k_- \sin(-\theta) = k_+ \sin(-\phi)$. In a similar way, a solution for the negative x-component can also be obtained but for the case with hard wall confinement we might assume the case with positive x-component only. The next step will be the introduction of boundary conditions.

The hard wall boundary condition imposes that the wave-function is zero on the borders ($y = 0$ and $y = r_1 + d + r_2 = L$). Thus, the exact eigenvalue equation for the Rashba NW is

$$\left[e^{2ik_+ \sin(\theta)L} + e^{2ik_- \sin(\phi)L}\right] \cos(\theta + \phi) - \left[1 + e^{2iL(k_+ \sin(\theta)+k_- \sin(\phi))}\right] \cos(\theta - \phi) + \quad (5.7)$$

$$4 \left[\sin(\theta)\sin(\phi) + \sin(k_+ L \sin(\theta)) \sin(k_- L \sin(\phi))\right]$$

$$\left[\cos(L(k_+ \sin(\theta) + k_- \sin(\phi))) + i \sin(L(k_+ \sin(\theta) + k_- \sin(\phi)))\right] = 0.$$

Unfortunately, no explicit selection rules for the quantum numbers can be extracted from this equation but in the limit where $\theta = \phi$ and $k_+ = k_-$, in case of no SOI, the well known solution is recovered

$$\sin(k_- L \sin(\phi)) = 0. \quad (5.8)$$

This leadis to $k_- L \sin(\phi) = n\pi$, where n it is a positive integer number.

5.2 Perturbation theory

Since the exact solution for a NW with no SOI is known, Eq. (5.2), with their correspondent eingenvalues

$$\mathcal{E}^0_{k_x,n_y,n_z,\sigma} = \frac{\hbar^2}{2m} \left(k_x^2 + \frac{\pi^2 n_y^2}{(r_1 + r_2 + d)^2} + \frac{\pi^2 n_z^2}{r^2} \right), \tag{5.9}$$

one can consider the part of the Hamiltonian (5.10) proportional to α as a perturbation,

$$\mathcal{H} = \mathcal{H}_0 + \alpha(\mathbf{r})\mathcal{H}_1 = \frac{p^2}{2m^*} + V_c(y,z) + \frac{1}{2\hbar}[\alpha(\mathbf{r}) \cdot (\sigma_x p_y - \sigma_y p_x)]_{\hat{z}}. \tag{5.10}$$

Once again, the z-component does not change due to the applied gate, and it is not going to be explicitly shown in the next steps. Performing a first order correction on the eigenenergies and eigenvectors of the unperturbed system, we obtain

$$\alpha \mathcal{H}_1 |\psi\rangle = \frac{-i\alpha}{2} \sqrt{\frac{2}{r_1 + r_2 + d}} \sum_{k_x,n_y,\sigma} \left[\left(\frac{n_y \pi}{r_1 + r_2 + d} \right) \cos \left(\frac{n_y \pi y}{r_1 + r_2 + d} \right) e^{ik_x x} |-\sigma\rangle - \right. \tag{5.11}$$
$$\left. \sin \left(\frac{n_y \pi y}{r_1 + r_2 + d} \right) (ik_x) e^{ik_x x} (i\sigma) |-\sigma\rangle \right],$$

and

$$\langle \psi'|\alpha \hat{H}_1 |\psi\rangle = \frac{-i\alpha}{(r_1 + r_2 + d)} \sum_{n_y' n_y} \left[\frac{n_y', n_y (\cos(n_y \pi) \cos(n_y' \pi) - 1)}{(n_y - n_y')(n_y + n_y')} + \right. \tag{5.12}$$
$$\left. \frac{\sigma k_x (r_1 + r_2 + d)}{2} \delta_{n_y',n_y} \right] \delta_{\sigma',-\sigma},$$

where, $\sigma = \pm 1$ for spin up and down respectively.

The matrix element calculated above is the first order perturbation correction of the eigenenergy. The term where $n_y' = n_y$ is the intra-level correction,

$$\frac{-i\sigma \alpha k_x}{2} \delta_{n_y',n_y} \delta_{\sigma',-\sigma}, \tag{5.13}$$

whereas the inter-level correction term, $n_y' \neq n_y$, is given by

$$\frac{i\alpha n_y' n_y \left(1 - (-1)^{|n_y' - n_y|} \right)}{(r_1 + r_2 + d)(n_y^2 - n_y'^2)} \delta_{\sigma',-\sigma} \tag{5.14}$$

The inter-level correction is negligible in comparison to the intra-level one. Hence, taking into account only Eq.(5.13), the eigenvalue equation becomes

$$
\begin{pmatrix} 0 & \frac{i\alpha k_x}{2} \\ \frac{-i\alpha k_x}{2} & 0 \end{pmatrix} \begin{pmatrix} C^{\uparrow} \\ C^{\downarrow} \end{pmatrix} = \mathcal{E}^{(1)} \begin{pmatrix} C^{\uparrow} \\ C^{\downarrow} \end{pmatrix},
\tag{5.15}
$$

which gives the first order correction to the energy levels

$$
\mathcal{E}_{\pm}^{(1)} = \frac{\pm \alpha k_x}{2},
\tag{5.16}
$$

and their eigenvectors

$$
|\psi_n^{\sigma}\rangle_+^{(0)} = \frac{1}{\sqrt{2}} \left[|\psi_n^{\sigma}\rangle + i|\psi_n^{-\sigma}\rangle \right]
\tag{5.17}
$$
$$
|\psi_n^{\sigma}\rangle_-^{(0)} = \frac{1}{\sqrt{2}} \left[|\psi_n^{\sigma}\rangle - i|\psi_n^{-\sigma}\rangle \right].
$$

Therefore, the wave number component in the mixing region for the x-direction at a given energy $\mathcal{E}$ can be written as

$$
k_n^{\pm} = \sqrt{\frac{2m\mathcal{E}}{\hbar^2} - \frac{\pi^2 n^2}{(d + r_1 + r_2)^2} - \frac{\pi^2}{r^2} + \frac{\alpha^2 m^2}{4\hbar^4}} \mp \frac{\alpha m}{2\hbar^2}.
\tag{5.18}
$$

Since all wave functions were well defined through the perturbation theory, the Transfer Matrix Method presented in Chapter 3 [83] will be employed in order to study the transport properties of the system described in Fig. (5.1).

5.3 Transport

The system was divided in three regions: (i) the regions where $x < 0$ (left), (ii) $x > L$ (right), both with no SOI, $\alpha = 0$, and (iii) in the middle region $0 < x < L$, with $\alpha \neq 0$. The interfaces between these regions are considered sharp walls with finite potential steps. Thus, one must calculate the current relation between the regions. [100] The system Schrödinger equation has the form

$$
\frac{\hbar^2}{2m} \frac{\partial^2 \Psi}{\partial x^2} - \frac{\imath}{2} \left[\alpha(x) \left(-\sigma_y \frac{\partial}{\partial x} \right) + \left(-\sigma_y \frac{\partial}{\partial x} \right) \alpha(x) \right] \Psi = \mathcal{E}\Psi.
\tag{5.19}
$$

Integrating at the boundary

$$\int_{-\epsilon_0}^{\epsilon_0} \frac{\partial^2 \Psi}{\partial x^2} dx + \int_{-\epsilon_0}^{\epsilon_0} \frac{m\imath\sigma_y}{\hbar^2} \left[\alpha(x)\frac{\partial}{\partial x} + \frac{\partial \alpha(x)}{\partial x} \right] \Psi dx = \int_{-\epsilon_0}^{\epsilon_0} \mathcal{E}\Psi dx, \qquad (5.20)$$

where the second term of the left side will be integrated by parts

$$\frac{\partial \Psi}{\partial x}\Big|_{-\epsilon_0}^{\epsilon_0} + \frac{m\imath\sigma_y}{\hbar^2} \left[(\alpha(x)\Psi)_{-\epsilon_0}^{\epsilon_0} - \int_{-\epsilon_0}^{\epsilon_0} \frac{\partial \alpha(x)}{\partial x}\Psi dx + \int_{-\epsilon_0}^{\epsilon_0} \frac{\partial \alpha(x)}{\partial x}\Psi dx \right] = 0, \qquad (5.21)$$

the current relation between regions with and without SOI is

$$\frac{\partial \Psi(\epsilon_0)}{\partial x} - \frac{\partial \Psi(-\epsilon_0)}{\partial x} + \frac{m\imath\sigma_y}{\hbar^2} \left[\alpha(\epsilon_0)\Psi(\epsilon_0) - \alpha(-\epsilon_0)\Psi(-\epsilon_0) \right] = 0 \qquad (5.22)$$

Schematically, in order to build the Transfer Matrix, the set of matrices (Eq. (3.9)) at $x = 0$ (Fig. (5.1)) will follow the conditions below: the eigenstates for the left and middle region are continuous and their first derivative are governed by the relation given in Eq. (5.22), where $\alpha(-\epsilon_0) = 0$. The mass on both sides are the same since they are constituted by the same material. Therefore,

$$\mathbf{M}_{Left}(0) \begin{pmatrix} \mathbf{I} \\ \mathbf{R} \end{pmatrix} = \mathbf{M}_{Middle}(0) \begin{pmatrix} \mathbf{A} \\ \mathbf{B} \end{pmatrix}, \qquad (5.23)$$

where $\mathbf{A} = A_n^{\sigma'\sigma}$ and $\mathbf{B} = B_n^{\sigma'\sigma}$ are the four vector components of the the energy level $(n = \{n_y, n_z\})$, with incident spin σ' and outgoing spin σ. In turn, $\mathbf{I} = I_j^{\sigma'\sigma}$, and $\mathbf{R} = R_j^{\sigma'\sigma}$ are the four dimensional vectors for the transmitted and incident amplitudes at different NW branches, with incident spin σ' and outgoing spin σ.

$$\mathbf{M}_{Left}(0) = \begin{pmatrix} 1 & 1 & 0 & 0 & 0 & 0 & 0 & 0 \\ ik_{UL}^{\uparrow} & -ik_{UL}^{\uparrow} & 0 & 0 & 0 & 0 & 0 & 0 \\ 0 & 0 & 1 & 1 & 0 & 0 & 0 & 0 \\ 0 & 0 & ik_{BL}^{\uparrow} & -ik_{BL}^{\uparrow} & 0 & 0 & 0 & 0 \\ 0 & 0 & 0 & 0 & 1 & 1 & 0 & 0 \\ 0 & 0 & 0 & 0 & ik_{UL}^{\downarrow} & -ik_{UL}^{\downarrow} & 0 & 0 \\ 0 & 0 & 0 & 0 & 0 & 0 & 1 & 1 \\ 0 & 0 & 0 & 0 & 0 & 0 & ik_{BL}^{\downarrow} & -ik_{BL}^{\downarrow} \end{pmatrix},$$

and $\mathbf{M}^{\sigma}_{Middle}(0) =$.

$$
\begin{pmatrix}
\overset{(0)}{\pm}\langle\psi_1^{\sigma}|\phi_{UL}^{\sigma'}\rangle & \overset{(0)}{\pm}\langle\psi_1^{\sigma}|\phi_{UL}^{\sigma'}\rangle & \overset{(0)}{\pm}\langle\psi_2^{\sigma}|\phi_{UL}^{\sigma'}\rangle & \overset{(0)}{\pm}\langle\psi_2^{\sigma}|\phi_{UL}^{\sigma'}\rangle \\
\overset{(0)}{\pm}\langle\psi_1^{\sigma}|\phi_{UL}^{\sigma'}\rangle i(k_1^{\sigma}+\frac{m\alpha\sigma}{\hbar^2}) & \overset{(0)}{\pm}\langle\psi_1^{\sigma}|\phi_{UL}^{\sigma'}\rangle i(\frac{m\alpha\sigma}{\hbar^2}-k_1^{\sigma}) & \overset{(0)}{\pm}\langle\psi_2^{\sigma}|\phi_{UL}^{\sigma'}\rangle i(k_2^{\sigma}+\frac{m\alpha\sigma}{\hbar^2}) & \langle\phi_{UL}^{\sigma'}|\psi_2^{\sigma}\rangle\overset{(0)}{\mp}i(\frac{m\alpha\sigma}{\hbar^2}-k_2^{\sigma}) \\
\overset{(0)}{\pm}\langle\psi_1^{\sigma}|\phi_{BL}^{\sigma'}\rangle & \overset{(0)}{\pm}\langle\psi_1^{\sigma}|\phi_{BL}^{\sigma'}\rangle & \overset{(0)}{\pm}\langle\psi_2^{\sigma}|\phi_{BL}^{\sigma'}\rangle & \overset{(0)}{\pm}\langle\psi_2^{\sigma}|\phi_{BL}^{\sigma'}\rangle \\
\overset{(0)}{\pm}\langle\psi_1^{\sigma}|\phi_{BL}^{\sigma'}\rangle i(k_1^{\sigma}+\frac{m\alpha\sigma}{\hbar^2}) & \overset{(0)}{\pm}\langle\psi_1^{\sigma}|\phi_{BL}^{\sigma'}\rangle i(\frac{m\alpha\sigma}{\hbar^2}-k_1^{\sigma}) & \overset{(0)}{\pm}\langle\psi_2^{\sigma}|\phi_{BL}^{\sigma'}\rangle i(k_2^{\sigma}+\frac{m\alpha\sigma}{\hbar^2}) & \overset{(0)}{\pm}\langle\psi_2^{\sigma}|\phi_{BL}^{\sigma'}\rangle i(\frac{m\alpha\sigma}{\hbar^2}-k_2^{\sigma})
\end{pmatrix}
$$

At $x = L$, one has a similar condition for Eq. (3.9) but, unlike the previous current continuity condition, now $\alpha(\epsilon_0) = 0$. Thus,

$$
\mathbf{M}_{Middle}(L)\begin{pmatrix}\mathbf{A}\\\mathbf{B}\end{pmatrix} = \mathbf{M}_{Right}(L)\begin{pmatrix}\mathbf{T}\\\mathbf{I'}\end{pmatrix}, \tag{5.24}
$$

where $\mathbf{T} = T_j^{\sigma'\sigma}$, and $\mathbf{I'} = I_j'^{\sigma'\sigma}$ are all four dimensional vectors for the transmitted, and incident amplitudes at different NW branches, with incident spin σ' and outgoing spin σ.

$$\mathbf{M}^{\sigma}_{Middle}(L) =
\begin{pmatrix}
\pm\,{}^{(0)}\langle\psi_1^{\sigma}|\phi_{UR}^{\sigma'}\rangle e^{ik_1^{\sigma}L} & \mp\,{}^{(0)}\langle\psi_1^{\sigma}|\phi_{UR}^{\sigma'}\rangle e^{-ik_1^{\sigma}L} & \pm\,{}^{(0)}\langle\psi_2^{\sigma}|\phi_{UR}^{\sigma'}\rangle e^{ik_2^{\sigma}L} & \mp\,{}^{(0)}\langle\psi_2^{\sigma}|\phi_{UR}^{\sigma'}\rangle e^{-ik_2^{\sigma}L} \\[6pt]
\pm\,{}^{(0)}\langle\psi_1^{\sigma}|\phi_{UR}^{\sigma'}\rangle i\!\left(k_1^{\sigma}-\tfrac{m\alpha\sigma}{\hbar^2}\right)e^{ik_1^{\sigma}L} & \mp\,{}^{(0)}\langle\psi_1^{\sigma}|\phi_{UR}^{\sigma'}\rangle i\!\left(\tfrac{m\alpha\sigma}{\hbar^2}+k_1^{\sigma}\right)e^{-ik_1^{\sigma}L} & \pm\,{}^{(0)}\langle\psi_2^{\sigma}|\phi_{UR}^{\sigma'}\rangle i\!\left(k_2^{\sigma}-\tfrac{m\alpha\sigma}{\hbar^2}\right)e^{ik_2^{\sigma}L} & \mp\,{}^{(0)}\langle\psi_2^{\sigma}|\phi_{UR}^{\sigma'}\rangle i\!\left(\tfrac{m\alpha\sigma}{\hbar^2}+k_2^{\sigma}\right)e^{-ik_2^{\sigma}L} \\[6pt]
\pm\,{}^{(0)}\langle\psi_1^{\sigma}|\phi_{BR}^{\sigma'}\rangle e^{ik_1^{\sigma}L} & \mp\,{}^{(0)}\langle\psi_1^{\sigma}|\phi_{BR}^{\sigma'}\rangle e^{-ik_1^{\sigma}L} & \pm\,{}^{(0)}\langle\psi_2^{\sigma}|\phi_{BR}^{\sigma'}\rangle e^{ik_2^{\sigma}L} & \mp\,{}^{(0)}\langle\psi_2^{\sigma}|\phi_{BR}^{\sigma'}\rangle e^{-ik_2^{\sigma}L} \\[6pt]
\pm\,{}^{(0)}\langle\psi_1^{\sigma}|\phi_{BR}^{\sigma'}\rangle i\!\left(k_1^{\sigma}-\tfrac{m\alpha\sigma}{\hbar^2}\right)e^{ik_1^{\sigma}L} & \mp\,{}^{(0)}\langle\psi_1^{\sigma}|\phi_{BR}^{\sigma'}\rangle i\!\left(\tfrac{m\alpha\sigma}{\hbar^2}+k_1^{\sigma}\right)e^{-ik_1^{\sigma}L} & \pm\,{}^{(0)}\langle\psi_2^{\sigma}|\phi_{BR}^{\sigma'}\rangle i\!\left(k_2^{\sigma}-\tfrac{m\alpha\sigma}{\hbar^2}\right)e^{ik_2^{\sigma}L} & \mp\,{}^{(0)}\langle\psi_2^{\sigma}|\phi_{BR}^{\sigma'}\rangle i\!\left(\tfrac{m\alpha\sigma}{\hbar^2}+k_2^{\sigma}\right)e^{-ik_2^{\sigma}L}
\end{pmatrix},$$

and

$$\mathbf{M}_{Right}(L) =
\begin{pmatrix}
e^{ik_{UR}^{\uparrow}L} & e^{-ik_{UR}^{\uparrow}L} & 0 & 0 & 0 & 0 & 0 & 0 \\[4pt]
ik_{UR}^{\uparrow}e^{ik_{UR}^{\uparrow}L} & -ik_{UR}^{\uparrow}e^{-ik_{TR}^{\uparrow}L} & 0 & 0 & 0 & 0 & 0 & 0 \\[4pt]
0 & 0 & e^{ik_{BR}^{\uparrow}L} & e^{-ik_{BR}^{\uparrow}L} & 0 & 0 & 0 & 0 \\[4pt]
0 & 0 & ik_{BR}^{\uparrow}e^{ik_{BR}^{\uparrow}x} & -ik_{BR}^{\uparrow}e^{-ik_{BR}^{\uparrow}L} & 0 & 0 & 0 & 0 \\[4pt]
0 & 0 & 0 & 0 & e^{ik_{UR}^{\downarrow}L} & e^{-ik_{UR}^{\downarrow}L} & 0 & 0 \\[4pt]
0 & 0 & 0 & 0 & ik_{UR}^{\downarrow}e^{ik_{UR}^{\downarrow}L} & -ik_{UR}^{\downarrow}e^{-ik_{UR}^{\downarrow}L} & 0 & 0 \\[4pt]
0 & 0 & 0 & 0 & 0 & 0 & e^{ik_{BR}^{\downarrow}L} & e^{-ik_{BR}^{\downarrow}L} \\[4pt]
0 & 0 & 0 & 0 & 0 & 0 & ik_{BR}^{\downarrow}e^{ik_{BR}^{\downarrow}x} & -ik_{BR}^{\downarrow}e^{-ik_{BR}^{\downarrow}L}
\end{pmatrix}$$

As one can see, the functions overlaps in the $y-$ and $z-$directions at the boundaries were taken into account in the matrix elements of the Transfer Matrix, since the transport takes place along the x-direction. Hence, in what follows we will show their calculation.

The similarity of our model with the one dimensional transport case ends with the inclusion of the remaining two dimensions in the overlap terms. This may result in a quasi-one-dimensional system. The spin degenerated overlaps, presented in the matrices $\mathbf{M}^\sigma_{Middle}(0)$ and $\mathbf{M}^\sigma_{Middle}(L)$, are responsible for a full 8×8 non-singular matrix.

The wire eigenvector has the form of Eq. (5.2) while in the middle region assumes the form of Eq. (5.17). The overlaps can be calculated as

$$
{}^{(0)}_{\pm}\langle\psi_n^\sigma|\phi_j^{\sigma'}\rangle = \int_0^r \int_C^D \sqrt{\frac{2}{r_{1,2}}}\sin\left(\frac{n_y^j\pi y}{r_{1,2}}\right)\sqrt{\frac{2}{r}}\sin\left(\frac{n_z^j\pi z}{r}\right)\times \tag{5.25}
$$

$$
\frac{1}{\sqrt 2}\sqrt{\frac{2}{r_1+r_2+d}}\sin\left(\frac{n_y\pi y}{r_1+r_2+d}\right)\sqrt{\frac{2}{r}}\sin\left(\frac{n_z\pi z}{r}\right)\langle\sigma'|\sigma\rangle dydz.
$$

Integrating along the z-direction, one obtain $\delta_{n_z^j,n_z}$. Depending on the wire branch, the integration limits in the y-direction changes. For the upper wire, $C = 0$ and $D = r_1$, and for the bottom wire $C = r_1 + d$ and $D = r_1 + r_2 + d$. The inner product between the latter case and the first level is equal

$$
{}^{(0)}_{\pm}\langle\psi_1|\phi_U^{\sigma'}\rangle = \frac{\frac{\sin\left(\frac{\pi(d+r_2)}{d+r_1+r_2}\right)}{d+r_2} - \frac{\sin\left(\frac{\pi(d+2r_1+r_2)}{d+r_1+r_2}\right)}{d+2r_1+r_2}}{\pi\sqrt{\frac{1}{r_1}}\sqrt{\frac{1}{d+r_1+r_2}}}\frac{1}{\sqrt 2}\left[\uparrow \mp i\downarrow\right], \tag{5.26}
$$

and between the second level

$$
{}^{(0)}_{\pm}\langle\psi_2|\phi_U^{\sigma'}\rangle = \frac{\frac{\sin\left(\frac{\pi(d-r_1+r_2)}{d+r_1+r_2}\right)}{d-r_1+r_2} - \frac{\sin\left(\frac{\pi(d+3r_1+r_2)}{d+r_1+r_2}\right)}{d+3r_1+r_2}}{\pi\sqrt{\frac{1}{r_1}}\sqrt{\frac{1}{d+r_1+r_2}}}\frac{1}{\sqrt 2}\left[\uparrow \mp i\downarrow\right]. \tag{5.27}
$$

Likewise, the inner product between last case and the first level equals

$$
{}^{(0)}_{\pm}\langle\psi_1|\phi_B^{\sigma'}\rangle = \frac{\frac{\sin\left(\frac{\pi r_2}{d+r_1+r_2}\right)}{d+r_1+2r_2} - \frac{\sin\left(\frac{\pi(2d+2r_1+r_2)}{d+r_1+r_2}\right)}{d+r_1}}{\pi\sqrt{\frac{1}{r_2}}\sqrt{\frac{1}{d+r_1+r_2}}}\frac{1}{\sqrt 2}\left[\uparrow \mp i\downarrow\right], \tag{5.28}
$$

and between the second level,

$$
\begin{array}{c}
{}^{(0)}_{\pm}\langle\psi_2|\phi_B^{\sigma'}\rangle = \dfrac{\dfrac{\sin\left(\frac{\pi(-d-r_1+r_2)}{d+r_1+r_2}\right)}{d+r_1+3r_2} - \dfrac{\sin\left(\frac{\pi(3d+3r_1+r_2)}{d+r_1+r_2}\right)}{d+r_1-r_2}}{\pi\sqrt{\frac{1}{r_2}}\sqrt{\frac{1}{d+r_1+r_2}}}\dfrac{1}{\sqrt{2}}\left[\uparrow \mp i\downarrow\right].
\end{array}
\tag{5.29}
$$

Therefore, an 8×8 Transfer Matrix relating the 16 coefficients (incident waves, transmissions, and reflections), spin up and down, from the bottom and upper wire, was built in a similar way to Eq. (3.10). The results are going to be presented in the next section.

5.4   Results and discussion

5.4.1   With no spin orbit interaction

Figure 5.3 shows the transmission (T_1, T_2, and T_3) and reflection (R) probabilities versus the incident particle energy ($\mathcal{E}$) for wires with the same radius ($r_1 = r_2 = 100$ Å), $L = 400$ Å, and $d = 100$ Å. The incident wave is on the right side of the upper wire. T_1 is the transmission on the upper wire right side, T_2 is the transmission on the bottom wire right side, T_3 is the transmission on the bottom wire left side, and R is the reflection.
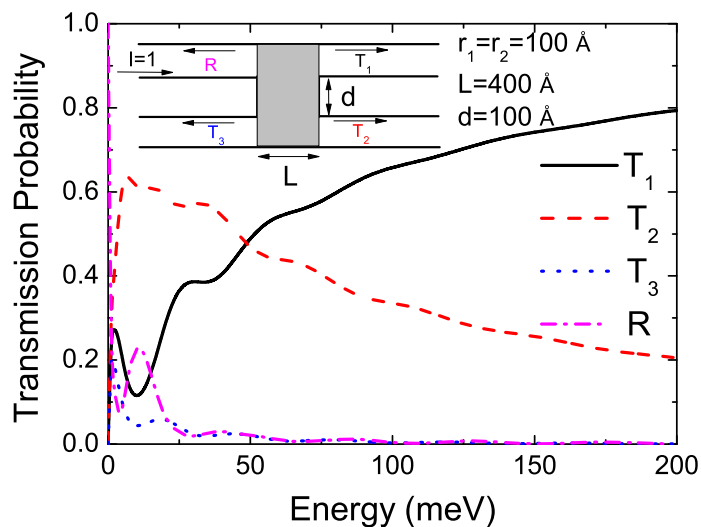
Fig. 5.3: Transmission probability versus energy for wires with same radius ($r_1 = r_2 = 100$ Å), $L = 400$ Å, and $d = 100$ Å. The incident wave is on the upper wire right side. T_1 is the transmission on the upper wire right side, T_2 is the transmission on the bottom wire right side, T_3 in the transmission on the bottom wire left side, and R is the reflection.

Figure 5.4 shows the transmission and reflection probabilities versus L and d for a fixed value of energy, $\mathcal{E} = 50$ meV, with one incident wave at the upper wire on the left side. In this case, we notice that, as we separate the wires from each other, by increasing

the distance d, the transmission T_1 (Figure 5.4 (a)) results almost the unit. In other words, the proposed solution reached the isolated wire limit.
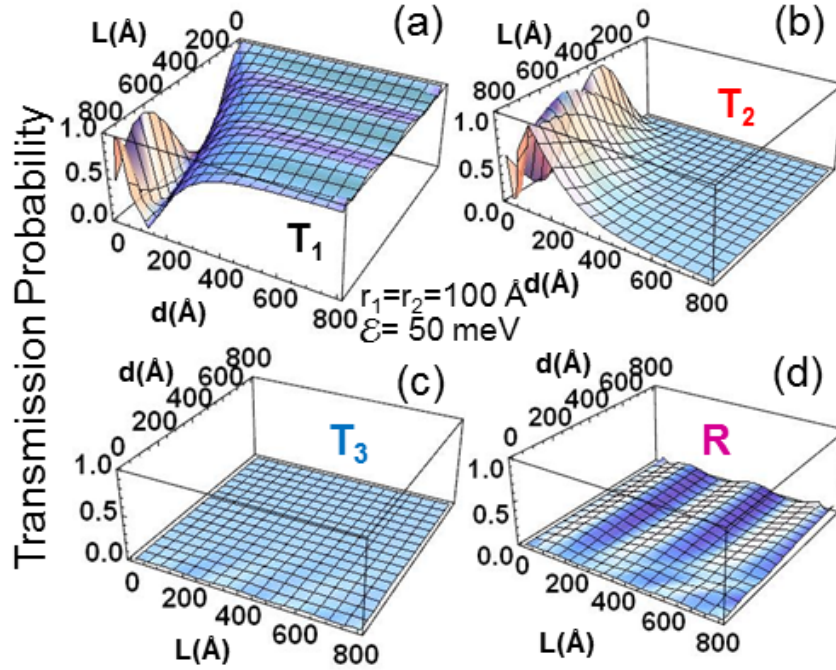
Fig. 5.4: Transmission probability versus L and d for wires with same radius $r_1 = r_2 = 100$ Åand energy $\mathcal{E} = 50$ meV, where the incident wave is on the upper wire, right side. (a) Transmission on the upper wire right side, T_1. (b) Transmission on the bottom wire right side, T_2. (c) Transmission on the bottom wire left side, T_3, and Reflection, R,

Considering values of d where the coupling between the wires is strong, one can see in Fig. 5.4 (a) and (b) that the maximum transmission alternates between T_1 and T_2, depending on the distance L. The transmissions and reflection oscillations with respect to L are periodic and correspond to the wavelength related to the middle region.

The reflection, R, and transmission, T_3, (bottom wire at the left side) have features related to reflected waves, as one can see on the oscillations due to L, but they do not attain expressive values in any possible configuration obtained by varying distances. In order to change this picture, one can think in the following way: applying a gate voltage in one of the wires, avoiding transmission in this one, one can force these waves to assume higher amplitudes, promoting R and T_3. Thus, Fig. 5.5 shows the transmissions and reflection coefficients versus the gate voltage (Vg_2) applied at the bottom wire on the left side (inset Figure 5.5 (a)).

In the chosen configuration, where $r_1 = r_2 = 100$ Å, $L = 400$ Å, $d = 100$ Å, and $\mathcal{E} = 50$ meV, the transmission probability is almost equally split between T_1 and T_2

whenever $Vg_2 = 0$. For small values of Vg_2, a slight decrease of T_2 and an increase of the other coefficients is noticed. At the moment when T_2 is totaly suppressed, with $Vg_2 = \mathcal{E} = 50$ meV, meaning that the channel is completed closed, an expressive increase of R and T_3 (Fig. 5.5 (a)) occurs. Likewise, Fig. 5.5 (b) shows the transmission probability versus Vg_2 for $\mathcal{E} = 10$meV. In this energy configuration, T_2 is predominant for $Vg_2 = 0$. By suppressing the transmission T_2, using the same mechanism described above, R enhances.
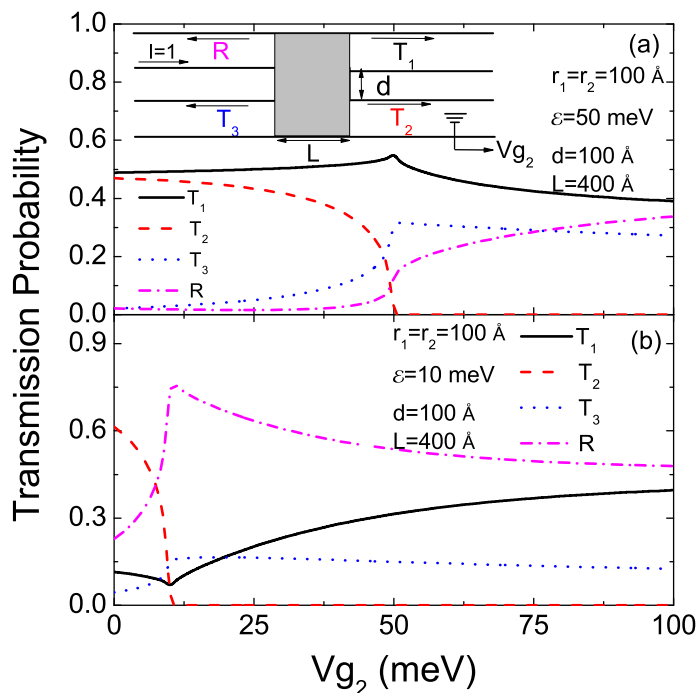
Fig. 5.5: Transmission probability versus the gate voltage at the bottom wire, left side, Vg_2. $r_1 = r_2 = 100$ Å, $L = 400$ Å, and $d = 100$ Å. (a) $\mathcal{E} = 50$ meV. (b) $\mathcal{E} = 10$ meV. Inset: Configuration scheme.

The results described till now belong to the no SOI case. It has been presented as a way to prove the validity of the model, since the directional coupler has been realized previously. [46, 47] Therefore, the next section will present the case with SOI, where an electric field on the z-direction, **E**, is applied in the middle region (Fig. 5.1).

5.4.2 Spin orbit interaction effects

The quantum transport properties of interconnected parallel wires through a potential barrier [46, 48, 99, 98] can be controlled by changing the barrier height and length. Similarly, one can modulate the carrier and spin transport by varying the length L of the middle mixing region and the separation d between wires. This formalism enables the study of different spin polarization configurations for the incident waves and we shall

present results for an incident wave in one of the wires with up or down spin-polarization along the z-direction.

Figure 5.6 shows the transmission and reflection coefficients vs. the length of the mixing region, L, for an incident spin-down polarized wave (inset Fig. 5.6), where $d = 100$ Å, and $r_1 = r_2 = 100$ Å. We can see, in Fig. 5.6(d), that the spin-preserving transport coefficient $T_2^{\downarrow\downarrow}$ can be suppressed or enhanced with a characteristic periodicity $\simeq L_{\Delta k} = 2\pi/\Delta k$. For a given incident energy $\mathcal{E}$, the corresponding wave vectors $k_n^{\pm}$ along each given channel, $n = 1, 2$, are given through Eq. (5.18). The momentum difference $\Delta k = k_1^{\sigma} - k_2^{\sigma}$, is responsible for the long period oscillations as the two $(\pm)$ channels interfere with one another. For $\mathcal{E} = 50$ meV, one finds $L_{\Delta k} = 2\pi/\Delta k \simeq 120$ nm, a value that coincides with the oscillation period. Moreover, whenever $T_2^{\sigma'\sigma}$ is enhanced, $T_1^{\sigma'\sigma}$ is suppressed as displayed in Fig. 5.6(b) and (d)–i.e, they oscillate out of phase, illustrating their competition. Opposite phase oscillations between the NWs result for a symmetric system such as the one characterized here, with an initial condition corresponding to an incident wave in only one of the NW's branches as represented in the inset of Fig. 5.6. The coefficients also show fast oscillations characterized by $L_{\mathcal{E}} = \sqrt{\pi^2\hbar^2/2m\mathcal{E}}$, in analogy with the transmission above a quantum well. For $\mathcal{E} = 50$ meV, these fast oscillations have the corresponding length scale $L_{\mathcal{E}} \simeq 10$ nm. Thus, one is able to adjust the transmission by changing sizes, widths, and lengths of mixing regions, as expected from the directional coupler geometry of the system.[46, 47, 99]

The introduction of SOI provides an additional control on the overall transmission amplitudes, as well as on the spin polarized transmission. The SOI length scale, given by the period over which the spin precesses from $\uparrow$ to $\downarrow$ (and vice versa) due to the effective Rashba field, is $L_{SO} = \pi\hbar^2/\alpha m$ ($\simeq 230$ nm, in Fig. 5.6). One can clearly see the effect of this precession in Fig. 5.6(b), where the incident spin down is fully transmitted in the up-projection at $L \simeq L_{SO}$, $T_1^{\downarrow\uparrow}$, while the spin-preserving channel is nearly fully blocked, $T_1^{\downarrow\downarrow} \simeq 0$. Figure 5.6(a) and (c) show the reflection, $R^{\downarrow\sigma}$, and transmission in the bottom left NW, $T_3^{\downarrow\sigma}$, respectively. These coefficients are characterized by oscillations with shorter periods due to the fact that the wave travels twice the distance L. Moreover, in this configuration, the length scale L_{SO} becomes comparable to $2L_{\Delta k}$, resulting in a more complex interference pattern such as the beating behavior evident on $R^{\downarrow\downarrow}$. These results correspond to a spin-polarized incident wave; reversing the incident spin produces

the spin reversal of the transmitted and reflected amplitudes, as expected from the time-reversal invariance of the Hamiltonian, as well as from the spatial symmetries of the system.[54, 17]
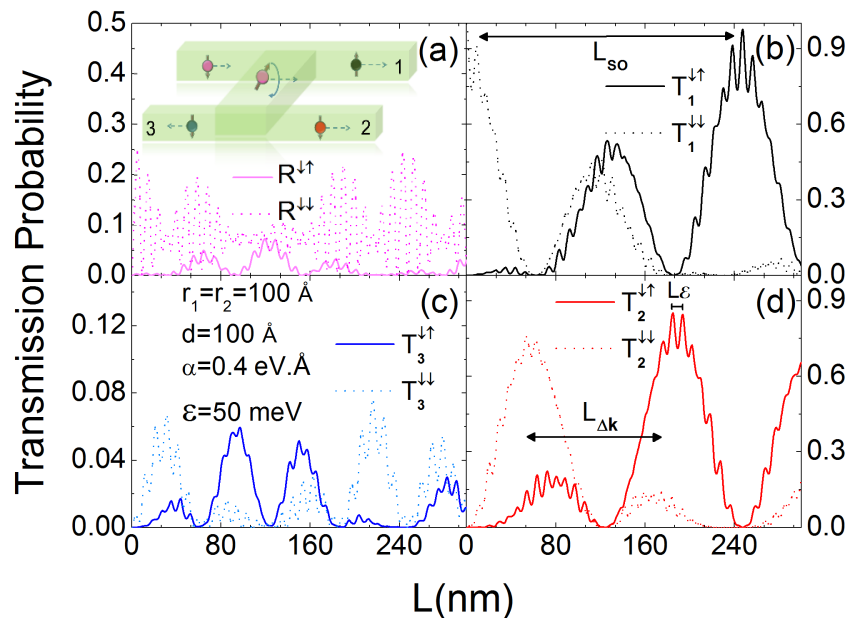
Fig. 5.6: Transmission probabilities vs length of the mixing region L for incident spin-down polarized flux ($I^{\downarrow}$), where $r_1 = r_2 = 100$ Å, $d = 100$ Å, $\mathcal{E} = 50$ meV, $\alpha = 0.4$ eV·Å, and $m = 0.026m_0$. (a) Reflection on the left top wire ($R^{\downarrow\sigma}$). (b) Transmission on the right top wire ($T_1^{\downarrow\sigma}$). (c) Transmission on the left bottom wire ($T_3^{\downarrow\sigma}$). (d) Transmission on the right bottom wire ($T_2^{\downarrow\sigma}$). Notice that reflection values in (a) and (c) are much smaller than the transmission in (b) and (d).

To better characterize how the system responds to the injection of an unpolarized superposition of spin-up and spin-down fluxes, we calculate the spin persistence ratio $C_j \equiv \left[T_j^{\uparrow\uparrow} + T_j^{\downarrow\downarrow} - (T_j^{\downarrow\uparrow} + T_j^{\uparrow\downarrow}) \right] / T$, where $T = T_j^{\uparrow\uparrow} + T_j^{\downarrow\downarrow} + T_j^{\downarrow\uparrow} + T_j^{\uparrow\downarrow}$, for each NW branch, j. Note that, if $T_j^{\uparrow\uparrow} = T_j^{\uparrow\downarrow}$ and $T_j^{\downarrow\downarrow} = T_j^{\downarrow\uparrow}$, then $C_j = 0$, a signature of a "memoryless" channel. On the other hand, $C_j = 1$ (-1), for a full spin-preserving (or reversing) channel. Figure 5.8 shows the color map of characteristic C_j vs α and L for each wire branch, j. The spin reversing regions are identified by the dark (blue) color and evolve with both α and length L, such that $\alpha L \simeq L/L_{SO} = $ constant, as expected from the Rashba precession length. Alternatively, pale gray regions indicate spin-preserving characteristics. One can also identify nearly α-independent oscillations, more visible in Fig. 5.8(a) and (c) within this area, associated with $L/L_{\Delta k} = $ constant.

One cannot expect a net spin polarization for the current, even when the system symmetry is broken by applying a gate voltage difference between the wires or making the
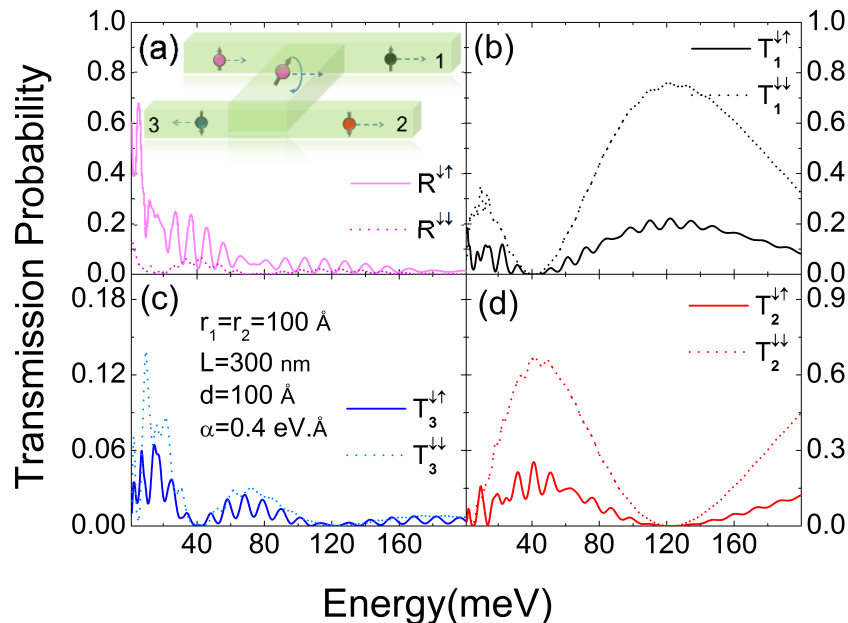
Fig. 5.7: Transmission probability versus the incident spin polarized particle $(I^\uparrow)$ energy for wires with same radius $(r_1 = r_2 = 100$ Å$)$, $L = 400$ Å, and $d = 100$ Å. $I^\uparrow$ is on the upper wire right side. $T_1^{\uparrow,\downarrow}$ are the spin up and down transmissions on the upper wire right side, respectively, $T_2^{\uparrow,\downarrow}$ are the transmissions on the bottom wire right side, $T_3^{\uparrow,\downarrow}$ are in the transmissions on the bottom wire left side, and $R^{\uparrow,\downarrow}$ are the reflections. (b) Transmission probability versus the Rashba strength parameter (α)

device asymmetric in other ways. This is due to the fact that for transport along the x-direction, the electric field on the z-direction, and the corresponding Rashba SOI, will produce spin precession of the z-spin for both spin components in a symmetric fashion. [101, 17] The degree of spin polarization is defined by $P_j \equiv \left[T_j^{\uparrow\uparrow} + T_j^{\downarrow\uparrow} - (T_j^{\downarrow\downarrow} + T_j^{\uparrow\downarrow}) \right] / T$. As expected, there is no net polarization in the z-direction. However, the effective Rashba magnetic field is along the y-direction, which suggests one to explore the possibility of tuning this quantity along that axis, P_j^y. The application of a gate voltage in one of the branches to raise the local energy of the subbands, as well as the strength of the Rashba SOI, can further help to tune the polarization in the remaining output wires. Figure 5.9 shows P_j^y as a function of the Rashba SOI strength, α, and an applied gate voltage on the bottom right wire, Vg_2. Panels (a) and (c) correspond to the incident energy $\mathcal{E} = 50$ meV, and panels (b) and (d), to $\mathcal{E} = 100$ meV. One can see that Fig. 5.9(a) displays two regions where the y-polarization is well defined. Around $\alpha = 0.12$ eV·Å and $Vg_2 = 0.14$ eV we notice full spin-down polarization, while for the same Vg_2 but at $\alpha = 0.48$ eV·Å, one has the opposite polarization. These features change location and sign as the incident energy varies. These results demonstrate the possibility of spin-inversion of the current flux by
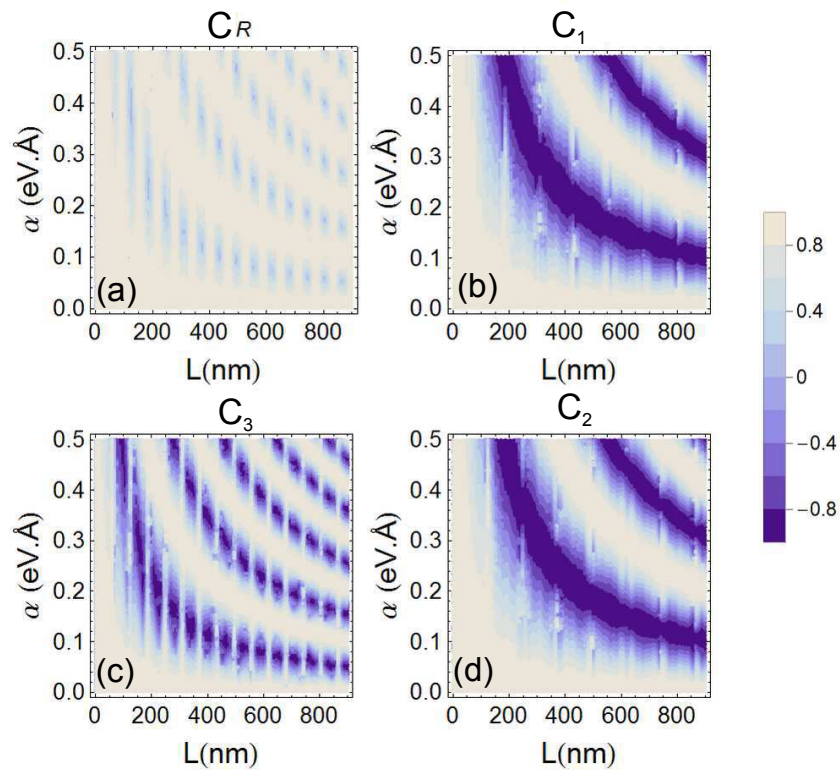
Fig. 5.8: Map of spin persistence ratio C_j vs α and L, where $r_1 = r_2 = 100$ Å, $d = 100$ Å, and $\mathcal{E} = 50$ meV. Panels show results for different NWs: (a) top left reflection, (b) top right, (c) bottom left, and (d) bottom right transmissions. Spin-reversal regions (dark blue) occur for $\alpha L \simeq L/L_{SO} = $ constant.

controlling α (via **E**) or Vg_2 (via applied gates). Figure 5.9(c) and (d) correspond to T_3, and one may note that they present similar behavior, but the features have a smoother (not as sudden) variations with α or Vg_2.

5.5   Conclusion

In conclusion, we have studied the spin transport properties of a NW directional coupler implemented by parallel wires joined by a mixing region which generates Rashba spin-orbit interaction. Using the Transfer Matrix approach allowed us to understand the modulation of electronic and spin transport arising from the combination of SOI and the system geometrical features. Likewise, SOI and applied gate voltages give rise to a modulation of the polarization when the spin is projected in the same direction as the effective Rashba magnetic field. The versatility of this device may be useful in all-electrical spintronic devices.
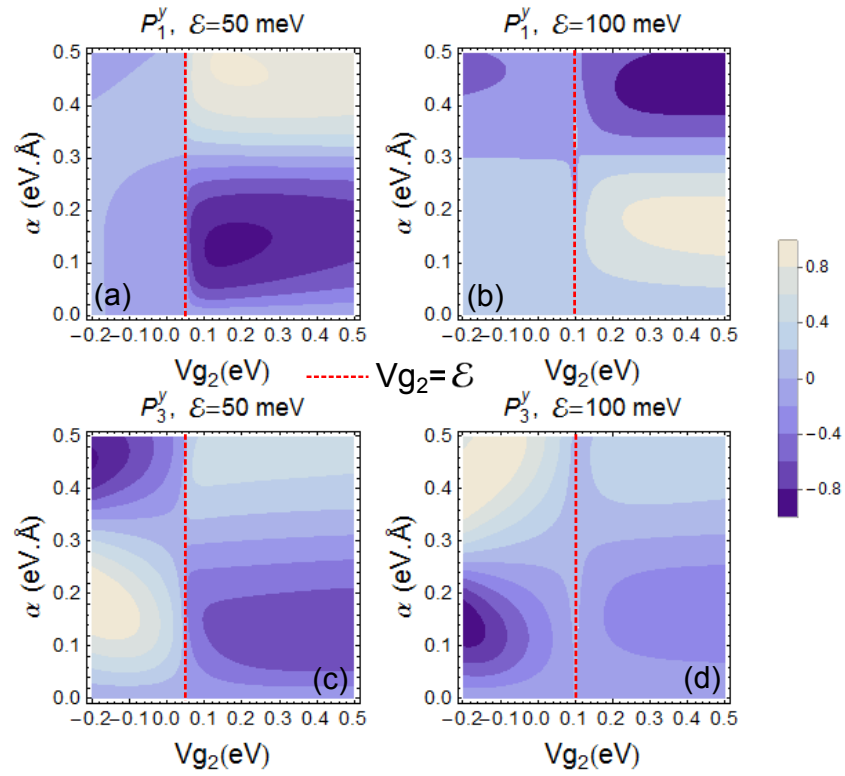
Fig. 5.9: Polarization in the y-direction vs α and applied gate voltage on the bottom right wire, (Vg_2), where $r_1 = r_2 = 100$ Å, $d = 100$ Å, and $L = 300$ nm. (a) Polarization for the top right wire (P_1^y) with $\mathcal{E} = 50$ meV. (b) Polarization for the top right wire (P_1^y) with $\mathcal{E} = 100$ meV. (c) Polarization for the bottom left wire (P_3^y) with $\mathcal{E} = 50$ meV. (d) Polarization for the bottom left wire (P_3^y) with $\mathcal{E} = 100$ meV. Red dashed lines indicate $Vg_2 = \mathcal{E}$ in each panel.

6. 1D TRANSPORT THROUGH HETEROSTRUCTURED SYSTEMS

Exploring functional nanotechnology has become a central task in recent research endeavors given the advances attained in the synthesis of nanomaterials. The technological advantage of heterostructured systems is related to the ability of engineering and controlling their quantum properties which can be achieved, for instance, through the modification of NW geometry and strain fields, giving rise to twin-plane NW, and by exploiting the effect of new materials. In what follows two main heterostructured objects will be presented. First we shall discuss the double barrier, as resonant tunneling diodes, which is a basic conceptual milestone for 1D quantum transport. In this case, we will demonstrate how the transport properties can be tuned by external factors such as temperature and charge accumulation. Then, the results obtained for Twin-Plane superlatices will be presented.

6.1 Double barrier - Resonant tunneling diodes

Describing the 1D transport in resonant tunneling diodes (RTDs) requires the use of some of the main concepts condensed within this thesis. Additionally, it has been demonstrated the relevance of such structures as sensors with characteristics such as high internal gain and aptitude for single photon detection. [55, 56, 57]. The basic principle of these detectors is the local and sensitive variation of the electric field, caused by accumulated carriers at the intrinsic tunneling structure. [58, 59, 60]. Effectively, the transmission probability of majority carriers is altered by accumulation of photo-generated ones. In particular, the process of modulation of the transport response of RTDs due to charge accumulation has become a problem to be tackled within an ongoing collaboration with experimental groups with relevant technological implications.

To exploit the RTDs full potential, the best working point has to be identified, which is a highly complex matter that requires knowledge of each quantity and the correlation between efficiency, carrier accumulation dynamics, and system gain. Recently, Al-
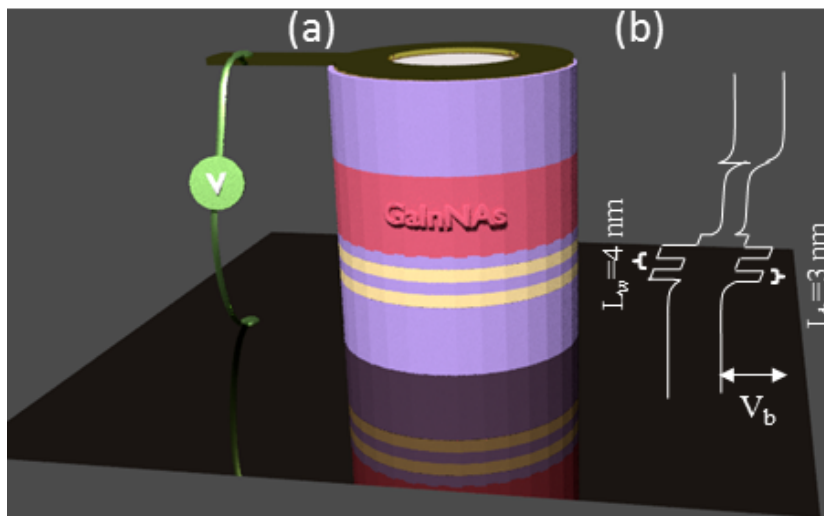
Fig. 6.1: Design and working principle of the resonant tunneling diode (RTD) photosensor. (a) Schematic layer sequence of the RTD with an electron microscopy image of the top ring contact. (b) Schematic conduction ($\mathcal{E}_{cb}$) band profile for a bias voltage V_b.

GaAs/GaAs based double barrier structure (DBS) with a nearby and lattice matched GaInNAs absorption layer was proposed for high sensitive photo detection at the telecommunication wavelength $\lambda = 1.30$ μm [61, 62]. These devices are the inspiration of the studied subject presented here, as well as its experimental results provided by the group of Prof. Lukas Worschech from UW. First, the transport properties of a DBS, like Al-GaAs/GaAs, is going to be explored (Fig. 6.1). Later, we will discuss the effect of a nearby GaInNAs layer in this system (Fig. 6.4).

Figure 6.1, left side, shows the layer sequence of the RTD structure. The samples were grown by molecular beam epitaxy on an n-doped GaAs substrate with doping concentration $n = 3 \cdot 10^{18} \text{cm}^{-3}$. First, 300 nm GaAs with decreasing doping concentration from $n = 1 \cdot 10^{18} \text{cm}^{-3}$ to $1 \cdot 10^{17} \text{cm}^{-3}$ is deposited and is followed by the undoped double barrier structure, which consists of 15 nm GaAs, two 3 nm $\text{Al}_{0.6}\text{Ga}_{0.4}\text{As}$ barriers and a 4 nm wide GaAs quantum well. The structure is completed with a 556 nm thick GaAs contact cap with $n = 1 \cdot 10^{18} \text{cm}^{-3}$. RTD mesas with a diameter $d = 5$ μm are fabricated by dry chemical etching and the top contact of each mesa is formed by a ring shaped Au contact (see electron microscopy image in Fig. 6.1). The bottom Ni/Au-Ge/Au contact is evaporated at the substrate.

The schematic conduction band profile ($\mathcal{E}_{cb}$) of the RTD for a applied bias voltage V_b is shown in Fig. 6.1, right side. Using this 1D profile, one can calculate the transport properties applying the transfer matrix method described in Chapter 3. Therefore,
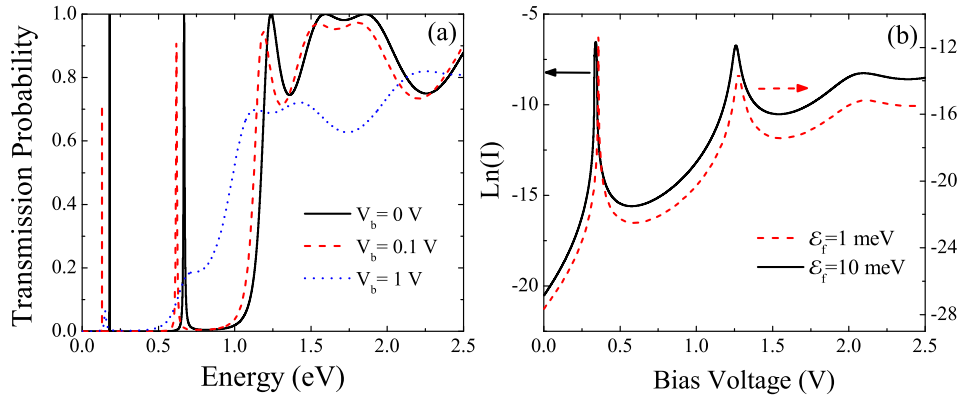
Fig. 6.2: Double barrier system. (a) Transmission coeficientes (T) vs. the electron energy in eV for the case where the applied bias voltage, V_b is: 0 V (solid black curve), 0.1 V (dashed red curve), and 1 V (dotted blue curve). (b) Natural log of the current density in units of $\left(\frac{em^*}{2\pi^2\hbar^3}\right)^{-1}$ vs. V_b for two different fermi energies, $\mathcal{E}_f$: 1 meV (dashed red curve), and 10 meV (solid black curve).

Fig. 6.2 (a) shows the transmission coeficientes, T, vs. the electron energy for different applied V_b ($V_b = 0$ V, solid black curve, $V_b = 0.1$ V, dashed red curve, and $V_b = 1$ V, dotted blue curve). As one can see, there are two bound states inside the well for a system in equilibrium ($V_b = 0$ V) but increasing the bias voltage these levels red shift and their transmission probability decreases, Fig. 6.2 (a). Figure 6.2 (b) shows the natural log of the current density in units of $\left(\frac{em^*}{2\pi^2\hbar^3}\right)^{-1}$ vs. V_b for two different fermi energies, $\mathcal{E}_f$, where a shift towards small bias voltages is seen while increasing $\mathcal{E}_f$.

The experimental $I-V$-characteristics are shown in Fig. 6.3 (a). The RTD is bistable with a resonance peak current I_{peak}, a valley current I_{valley}, and threshold voltages $V_{up,down}$ for the up and down sweep, respectively. The $I-V$ characteristics in the low temperature regime, black curve, and under room temperature, red curve (Fig. 6.3 (a)), show that while increasing the temperature the bistable area decreases. In order to probe this effect, one must include in the result obtained in Fig. 6.3 (b) the effect of a resistance in series, $V = V_b + I(V_b)R$. Thus, Fig. 6.3 shows the current density vs. the applied voltage, V for three different resistances, R, given in units of $\left(\frac{em^*}{2\pi^2\hbar^3V}\right)$. As onde can see, increasing the resistance the bistable area enhances.

Thus, the theoretical model indicates that the sheet resistance across the drain and source regions must increase by lowering the temperature while the voltage drop at the double barrier that defines the resonance condition in the $I-V$ curve should be independent on its variation. This is observed in the experimental results in Fig. 6.3 (a) for which the resonant position is almost unaffected by the temperature change. However, a
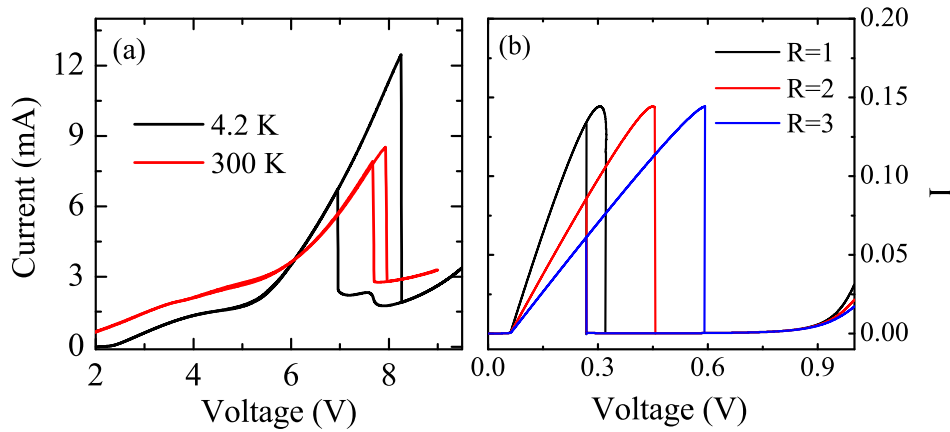
Fig. 6.3: (a) Experimental results. $I - V$ characteristics for two different temperatures: 4.2 K (black curve), and 300 K (red curve). (b) Theoretical simulation. Current density $\left[I \left(\frac{em^*}{2\pi^2\hbar^3} \right)^{-1} \right]$ vs applied voltage for three different resistances $\left[R \left(\frac{em^*}{2\pi^2\hbar^3 V} \right) \right]$.

small contribution of the sheet resistance is expected by the load line effect. If the total resistance of the RTD increases drastically, the voltage drop across the contact regions is enhanced and only a fraction of the applied bias effectively modulates the band profile at the DBS (Fig. 6.3 (b)). Herby, the resonance condition shifts to larger bias voltages but one would observe also a significant enlargement of the width of this hysteretic-like region, $Vup - V_{down}$.

Let us discuss what happens if an additional layer of InGaNAs is included. This has been achived experimentally integrating the GaAs/AlGaAs double barrier resonant tunneling diode with a 160 nm thick InGaNAs layer. At the GaInNAs/GaAs interface, a temperature dependent sheet charge is formed which induces changes in the internal voltage resulting in a threshold voltage shift of the bistable transition.

The top panel of Fig. 6.4 shows a scheme of the conduction (cb) and valence (vb) band profile for the biased RTD. As depicted in Fig. 6.4, electrons are injected from the source and tunnel resonantly through the DBS when their energy are equal to the quantum well layer subband energy. Additionally, a sheet charge with density n_i is formed at the GaInNAs/GaAs interface, as displayed in the bottom of Fig. 6.4. Under this configuration,
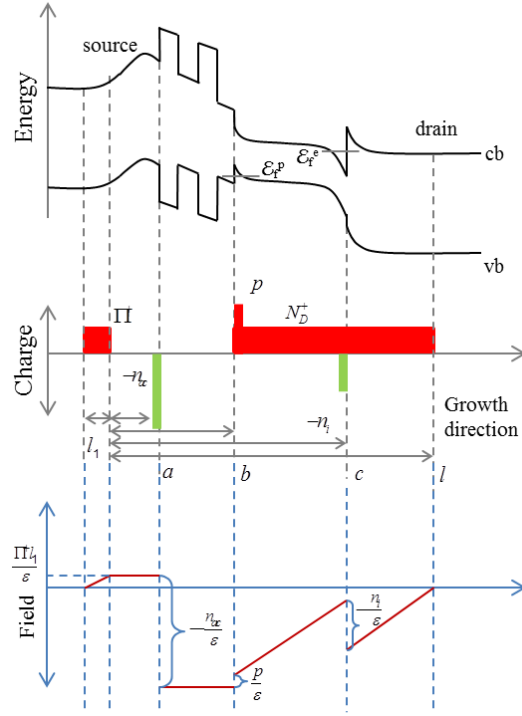
Fig. 6.4: Sample band profile, the corresponding diagram with the charge distribution along the growth direction, and the corresponding electric field profile.

the electric field within the structure follows the equation

$$
E(x) = \left[
\begin{array}{l}
\dfrac{\Pi^+}{\varepsilon}x; \quad 0 \le x < l_1 \\[2mm]
\dfrac{\Pi^+}{\varepsilon}l_1; \quad l_1 \le x < a + l_1 \\[2mm]
\dfrac{\Pi^+}{\varepsilon}l_1 - \dfrac{n_{ac}}{\varepsilon}; \quad a + l_1 \le x < b + l_1 \\[2mm]
\dfrac{\Pi^+}{\varepsilon}l_1 - \dfrac{n_{ac}}{\varepsilon} + \dfrac{p}{\varepsilon} + \dfrac{N_D^+}{\varepsilon}(x - (b + l_1)); \quad b + l_1 \le x < c + l_1 \\[2mm]
\dfrac{\Pi^+}{\varepsilon}l_1 - \dfrac{n_{ac}}{\varepsilon} + \dfrac{p}{\varepsilon} + \dfrac{N_D^+}{\varepsilon}(x - (b + l_1)) - \dfrac{n_i}{\varepsilon}; \quad c + l_1 \le x < l + l_1
\end{array}
\right. , \qquad (6.1)
$$

where Π^+ is the 3D ionized donor concentration at the source, N_D^+ is the 3D donor impurities concentration at the drain, n_{ac} is the 2D charge density accumulated at the DB, n_i is the 2D charge density accumulated ate the GaInNAs/GaAs interface, and p is charge density in the valence band. If $n_{ac} > N_D^+(c - b) + \Pi^+ l_1$, with the condition for neutrality yielding $E(0) = E(l + l_1) = 0$. This function has been represented in Fig. 6.4. Thus, the total voltage drop of the RTD, V_T, is given by

$$
V_T = \Delta V_{ab} - \frac{n_{ac}}{\varepsilon}(l - b) + \frac{N_D^+}{2\varepsilon}(l - b)^2 - \frac{\Pi^+}{\varepsilon}l_1(b - a) +
$$
$$
+ \frac{n_i}{\varepsilon}(c + l_1) - \frac{n_i - \Pi^+ l_1}{\varepsilon}(l + l_1) - \frac{\Pi^+}{2\varepsilon}l_1^2 + \frac{p}{\varepsilon}(l - b), \qquad (6.2)
$$

with the neutrality condition

$$\Pi^+ l_1 - (n_{ac} + n_i) + p + N_D^+(l - b) = 0 \qquad (6.3)$$

and the voltage drop at the DBS, between a and b, being

$$\Delta V_{ab} = -\frac{n_{ac} - \Pi^+ l_1}{\varepsilon}(b - a). \qquad (6.4)$$

Combining all the effects, as depicted in Fig. 6.4, with the charge balance provided by $n_{ac} - p = N_D^+(l - b)$ and $n_i = \Pi^+ l_1$, we obtain a total voltage drop as

$$V_T = \Delta V_{ab} + \frac{n_i^2}{2\varepsilon\Pi^+} + \frac{n_i[c - (b - a)]}{\varepsilon} - \frac{(n_{ac} - p)^2}{2\varepsilon N_D^+}. \qquad (6.5)$$

Using Eq. (6.4), one can write

$$V_T = -|\Delta V_{ab}| + \frac{n_i^2}{2\varepsilon}\left(\frac{1}{\Pi^+} - \frac{1}{N_D^+}\right) + \frac{n_i}{\varepsilon}\left[c - (b - a) - \frac{|\Delta V_{ab}|}{N_D^+(b - a)}\right] -$$
$$- \frac{1}{2\varepsilon N_D^+}\left[\frac{|\Delta V_{ab}| \cdot \varepsilon}{(b - a)} - p\right]^2 + \frac{p \cdot n_i}{\varepsilon N_D^+}. \qquad (6.6)$$

The experimental results, displayed in Fig. 6.5 (a), shows the RTD $I-V$ characteristics plotted for different temperatures ranging from $T = 10$ K up to $T = 300$ K. The room temperature $I - V$ curve, in Fig. 6.5 (a), shows a clear resonance with a peak current $I_{peak} = 0.86$ mA and a valley current $I_{valley} = 0.23$ mA. The RTD is bistable with a threshold voltage for the up-sweep $V_{up} = 5.085$ V and $V_{down} = 4.790$ V for the down-sweep. The peak-to-valley current ratio $PVR = I_{peak} = I_{valley}$ is 3.7 mA. As seen in Fig. 6.4 (a), the threshold voltages $V_{up,down}$ shift to greater values when the temperature is lowered. For $T = 10$ K, the up- and down-sweep thresholds are $V_{up} = 8.820$ V and $V_{down} = 7.850$ V, respectively. The threshold voltage shift also holds in the temperature range where the peak and valley currents remain constant, i.e. below $T = 100$ K.

Figure 6.5 (b) shows the calculated current density vs. applied voltage for three different values of charge accumulation, according to Eq. (6.6). One may see that both an increase of n_i or p will lead to the desired shift of the absolute voltage drop towards lower values.
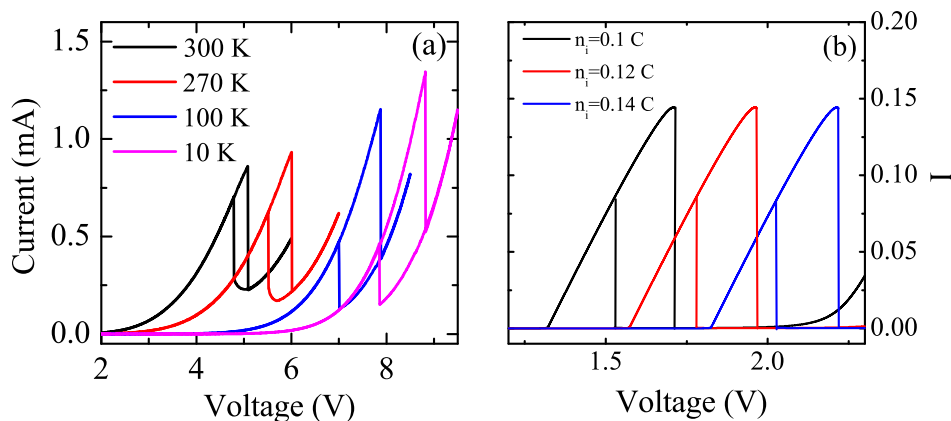
Fig. 6.5: (a) Experimental results for the sample with GaInNAs layer. $I - V$ characteristics for various temperatures from 10 K (pink curve) to 300 K (black curve). (b) Theoretical simulation. Current density in units of $\left(\frac{em^*}{2\pi^2\hbar^3}\right)^{-1}$ vs. applied voltage for three different values of charge accumulation.

6.1.1   Conclusion

In conclusion, modeling the 1D charge flow through hetherostructured systems may present unexpected challenges once experimental observations are involved. At this point, we are dealing with sequential studies based on the samples described above and several intriguing problems continue to appear. As being ongoing efforts we were not able to present them in the final version of this thesis.

In the particular problem described here we proved that also a resistance variation could lead to some threshold shift, it can be neglected as the dominant effect observed in the experiments on the sample with the InGaNAs layer. We thus demonstrated that the pronounced threshold voltage shift with temperature was caused by a variation of the sheet charge density n_i at the GaInNAs/GaAs interface. In the next section, we will show that the modulation of strain fields can also become an additional important effect in the 1D transport through an hetherostructure.

6.2   Twin-plane superlatice

The plausibility of building inhomogeneous heterostructures of a single semiconductor material was long ago theoretically predicted when stacking faults and the creation of layered systems of semiconductor segments between twin-planes were simulated. [21] There is however a major shortcoming in the effective use of twin-planes for quantum effects in zincblende heterostructures: the mere presence of a twin stacking fault would not
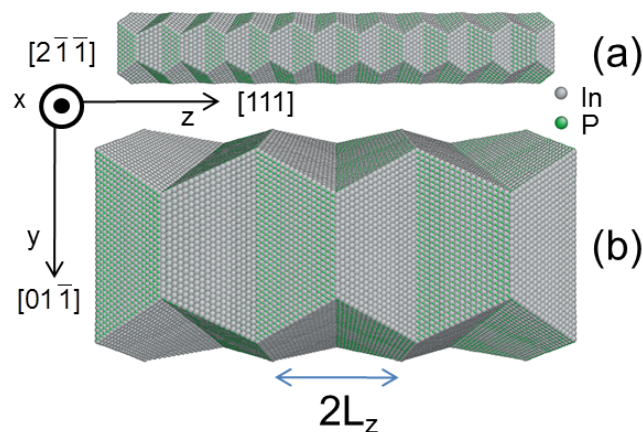
Fig. 6.6: Molecular dynamics simulation of NWs after undergoing relaxation and thermalization processes. The results for the NW1 (NW2) is shown in the upper (lower) panel. The cross section area of the NW1 and NW2 are 3189.5 Å^2 and 30973.4 Å^2, respectively. These NWs have periodic segments of size $2L_z$, where $L_z = 20.435$Å for NW1 and $L_z = 61.067$Å for NW2. Gray (green) dots represent Indium (Phosphorous) atoms. Notice that the twin-planes are composed by alternate layers of different atoms.

practically affect the transmission of Γ-electrons and these interfaces would remain mostly transparent. [63, 64] Just recently, the controlled synthesis of stacking fault heterostructures of III-V compound semiconductor NWs has been reported. [3, 4] It was shown that by controlling either the growth temperature and diameter of InAs NWs [3] or the amount of impurity dopants in analogous InP systems [4], a twin-plane superlattice can be experimentally realized. Such a microscopic control of the crystalline structure during the NW synthesis would open up opportunities for a thorough modulation of their electronic structure, thus increasing the potential use of these NWs as quantum heterodevices. In this section, we report a systematic study about the microscopic structure of NWs, the formation of their peculiar strain fields affected by the surface and twin-plane interfaces, and how they influence the electronic structure and transport properties of Γ-electrons and holes.

There is a vast literature about simulations of InP NWs. For instance, *ab initio* calculations were performed to study the stability of the NWs grown along [111] direction as a function of the diameter [104], the change on the total energy due to defects [105], the influence of hydrogen and oxygen on the surface of InP NWs [106], and the stability of InP NWs with zincblende and wurtzite structures [107]. Furthermore, Monte Carlo calculations were used by Sano *et al.* [108] to understand the formation of the twin-planes and the tight-binding model was applied by Persson and Xu [109] to study InP NWs with

orientation [100]. More recently, the band structure of twin-plane NWs was theoretically obtained within the framework of density functional theory. [110, 111] These calculations also show that there is indeed a possibility of band engineering on polytypic superlattices with alternate zincblende and wurtzite crystalline phases, with band-offsets up to 90 meV.

Once again, the partnership with the theoretical group of Prof. Jose P. Rino, experts in MD simulations, allowed the study of the properties of InP zincblende type NWs. By employing MD simulations combined with a multiband electronic structure calculation, we analyzed the electronic transport within the envelope function approximation. The advantage of using MD is related to the capacity to simulate real size NWs and to extract mechanical properties, which are used as input data to the multiband calculation. Interestingly, the variation of the band structure in this work is only due to strain fields caused by the formation of the twin-planes and the peculiar surface, differently from the case where polytypic phases are present. [110, 111] Based on the band structure results, we are able to calculate the transport properties of the twin-plane superlattice through the transfer matrix method [83]. Furthermore, we analyze the transport of both type of carriers: electrons and holes. This consideration is important because the transparency or opaqueness of a twin-plane superlattice is directly associated to the carrier character (controlled by the strain conditions), as it will be demonstrated by our results.

In this way, two InP NWs with different cross sections and with the same shape as reported in Refs. [3, 4] are simulated by the MD group. From the computationally simulated atomic structure of these NWs, the values of the elastic properties (elastic constants at T=0 K) and strain profiles (with and without external stress) are extracted. Such results were used as input parameters for the electronic structure calculation and the subsequent simulation of the electronic transport within the conduction and valence bands. In the following subsections, we describe how molecular dynamics is used to simulate InP NWs and how the interface effects is extract, which cannot be obtained through empirical methods (*e.g.* tight-binding and $\mathbf{k} \cdot \mathbf{p}$). Also, we show how the strain fields are included in the $\mathbf{k} \cdot \mathbf{p}$ Hamiltonian along [111] direction. After that, the electronic structure of the twin-planed InP NWs is calculated, which is the basis to determine the transport properties. Along with the description of the methods employed in this work, we also present and discuss the results in the subsections.

6.2.1 Molecular dynamics

Indium phosphide, as several other III-V semiconductors, crystallizes in a cubic zincblende structure, where each atom is tetrahedrally bonded to their nearest neighbor through different percentages of covalent and ionic bonds. In order to simulate a twin-planed nanowire, the atomic positions for a given number of atoms were generated considering the x, y and z axis parallel to the crystallographic directions [$2\bar{1}\bar{1}$], [$01\bar{1}$], and [111], respectively. To make an atomistic simulation of the NWs, an effective interatomic potential that considers two- and three-body interactions having the same functional form was assumed, as proposed by Ebbsjo *et al.* [113]. By using this interaction potential, Branicio *et al.* [88] were able to describe the thermodynamical properties, structural phase transformation induced by pressure, elastic constants, stacking faults and surface energies for bulk InP. However, to reproduce the experimental elastic constants and bulk modulus at 300 K (the only experimental value available in the literature) by keeping other thermodynamical and structural properties for InP adequately reported before, it was necessary to perform a small modification in a few parameters used in Ref. [88]. Otherwise, the simulations would lead to an underestimation of the elastic constants for bulk InP. Periodic boundary conditions were applied in z-direction with a vacuum region of 60Å created in the perpendicular directions. The whole system was allowed to relax in order to eliminate stress and was led to a thermal equilibrium at temperatures close to 0 K.

Figure 6.6 (a) shows the NW1 simulated by molecular dynamics, which has a cross section area of 3189.5 Å^2, a total length of 408.7 Å, totalizing 51320 atoms (25660 *In* + 25660 *P*). In Fig. 6.6 (b) we display the results for NW2, which was simulated by considering a cross section area of 30973.4 Å^2, a total length of 366.4 Å, and totalizing 449244 atoms (224622 In + 224622 P). Both NWs consist of periodic segments of size $2L_z$, as depicted in Fig. 6.6, where $L_z = 20.435$ Å for NW1 and $L_z = 61.067$ Å for NW2. One can notice, in Fig. 6.6, that the twin-plane structure remains after undergoing the thermalization and relaxation processes, what confirms the stability of this configuration. Due to the finite cross section size and the twin-plane, the positions of the atoms at these interfaces will be modified. The size of the cross section has a strong influence on this deformation and, depending on surface size, the mere presence of the surface may lead to a distribution of strain over the whole structure. However, in the range of parameters used to simulate the two NWs, the relative strain variation between consecutive core

segments and the interfaces near the twin-planes remains practically unaltered. For this reason, we present the results of strain distribution only for NW2, which has a size more compatible with typical experiments. [3, 4] The local stress distribution was calculated using the algorithm supplied in Ref. 21. Because the NW is not uniform, the local stress at the center of the NW2 was obtained by averaging the computed local stress for 70 atoms within the same plane around each point.

Figure 6.7 shows the distribution of the diagonal components σ_{11}, σ_{22} and σ_{33} of the stress tensor for a longitudinal cut taken in the middle region of the NW2, where the color coding stress threshold is saturated at the surface for a better contrast in the central region. The right panels (Fig. 6.7 (a)) correspond to $[2\bar{1}\bar{1}]$ cut plane view, whereas the left panels (Fig. 6.7 (b)) correspond to the $[01\bar{1}]$ cut plane view. Note that only σ_{11}, σ_{22}, and σ_{33} diagonal stress tensor components reveal the interface influence along the wire once the off-diagonal stress components have negligible values. Figure 6.8 shows the stress distribution for the same components, but for cross section cuts in the NW2 taken along [111] direction. The top panels display the stress distributions for the cut plane taken at the twin-plane interface and the bottom panels, for cuts taken in the middle of the segment between two consecutive twin-planes. The stress distribution in the region between two twin-planes depends on the NW cross section size. By increasing the cross
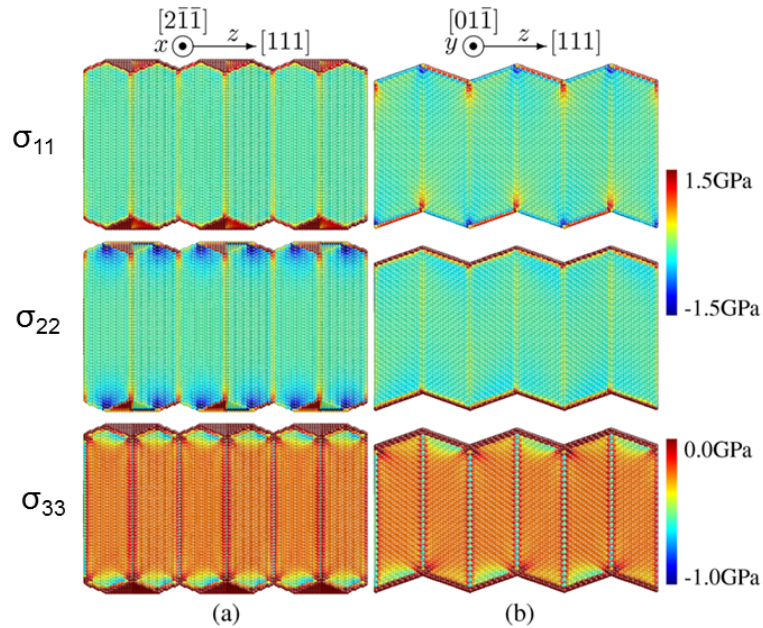
Fig. 6.7: Visualization of the local stress tensor components of the NW2. The left panels correspond to longitudinal cut view in the middle region of the NW2 at the plane $[2\bar{1}\bar{1}]$. The right panels are distributions for cut at the plane $[01\bar{1}]$. Color coding of stress threshold was saturated at the surface in order to get a better contrast in the central region.
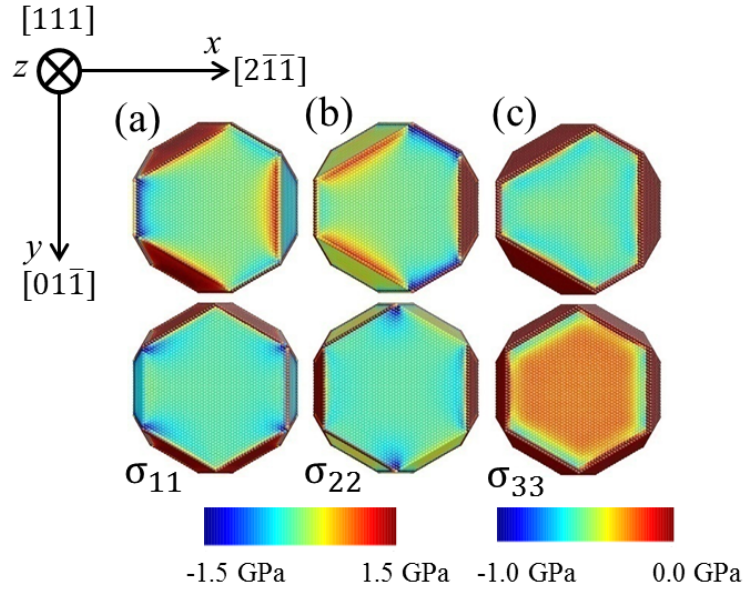
Fig. 6.8: Visualization of the local stress tensor components of the NW2. Upper panels show distribution of stress components for a transversal cut taken at the twin-plane interface. Lower panels show the stress distribution for a transversal cut taken at the middle of the segment. Columns (a), (b), and (c) show the distribution of the diagonal components of the stress tensor σ_{11}, σ_{22}, and σ_{33}, respectively.

section, the influence of the surface on the twin-plane strain field becomes less effective and the stress distribution becomes flat and goes to zero in these regions.

The linear approximation is adequate to characterize the correlation between stress and strain fields in a NW, which is given by Hooke's law: $\sigma'_{ij} = -\mathcal{C}'_{ijkl}\varepsilon'_{kl}$, where σ'_{ij} labels a stress tensor component, $\mathcal{C}'_{ijkl}$ is a component of the fourth order elastic stiffness tensor, and ε'_{kl} is the strain tensor component.

In order to determine the strain tensor components for wires grown as shown in Fig. 6.6, a rotation from $([100],[010],[001])$ to $([2\bar{1}\bar{1}],[01\bar{1}],[111])$ crystalline directions is required. The general relations between new and old coordinate systems are [115] $\sigma_{\alpha\beta} = \mathcal{U}_{i\alpha}\mathcal{U}_{j\beta}\sigma'_{ij}$, $\varepsilon_{\alpha\beta} = \mathcal{U}_{i\alpha}\mathcal{U}_{j\beta}\varepsilon'_{ij}$, $\mathcal{C}_{\gamma\delta kl} = \mathcal{U}_{\alpha\gamma}\mathcal{U}_{\beta\delta}\mathcal{U}_{ik}\mathcal{U}_{jl}\mathcal{C}'_{\alpha\beta ij}$, where the summation over repeated indices is assumed and the elements of the rotational matrix $\mathcal{U}_{mn}$ are given by

$$\mathcal{U} = \begin{pmatrix} \cos\alpha\cos\beta & -\sin\alpha & \cos\alpha\sin\beta \\ \sin\alpha\cos\beta & \cos\alpha & \sin\alpha\sin\beta \\ -\sin\beta & 0 & \cos\beta \end{pmatrix}, \tag{6.7}$$

where $\beta = \arccos\left(l/\sqrt{h^2+k^2+l^2}\right)$, $\alpha = \arccos\left(h/\sqrt{h^2+k^2}\right)$, and h, k and l designate

the Miller indexes. In the new axis, the Hooke's law, can be rewritten as

$$\sigma_{\gamma\delta} = -\mathcal{C}_{\gamma\delta kl}\varepsilon_{kl} \tag{6.8}$$

that is given in terms of the 36 components of the elastic stiffness tensor, [116]

$$
\begin{aligned}
\mathcal{C}_{\gamma\delta kl} &= \mathcal{C}'_{11}\sum_{\alpha=1}^{3}\mathcal{U}_{\alpha\gamma}\mathcal{U}_{\alpha\delta}\mathcal{U}_{\alpha k}\mathcal{U}_{\alpha l} + \mathcal{C}'_{12}\sum_{\beta=2}^{3}\sum_{\alpha=1}^{\beta-1}\left(\mathcal{U}_{\alpha\gamma}\mathcal{U}_{\alpha\delta}\mathcal{U}_{\beta k}\mathcal{U}_{\beta l} + \mathcal{U}_{\beta\gamma}\mathcal{U}_{\beta\delta}\mathcal{U}_{\alpha k}\mathcal{U}_{\alpha l}\right) \\
&+ \mathcal{C}'_{44}\sum_{\beta=2}^{3}\sum_{\alpha=1}^{\beta-1}\left(\mathcal{U}_{\alpha\gamma}\mathcal{U}_{\beta\delta} + \mathcal{U}_{\beta\gamma}\mathcal{U}_{\alpha\delta}\right)\left(\mathcal{U}_{\alpha k}\mathcal{U}_{\beta l} + \mathcal{U}_{\beta k}\mathcal{U}_{\alpha l}\right),
\end{aligned} \tag{6.9}
$$

For materials which crystallize in cubic symmetry, such as the zincblende structure, the stiffness tensor can be reduced from 36 to only three nonzero components labeled as $\mathcal{C}_{11}$, $\mathcal{C}_{12}$, and $\mathcal{C}_{44}$ elastic constants.

The electronic structure calculation that will be presented below simulates the system behavior at $T = 0$ K. However, only room temperature values of the elastic constants are found in the literature [77]. Thus, besides the strain field mapping, the MD simulations was used to deliver the elastic constants at zero temperature: $\mathcal{C}'_{11} = 107.68$ GPa, $\mathcal{C}'_{12} = 60.65$ GPa and $\mathcal{C}'_{44} = 41.10$ Gpa. The six components of the stress tensor along [111] direction as a function of the position was also obtained from the MD calculations. Thus, Eq. (6.8) was used to calculate the strain potential profile along this direction. Figures 6.9 (a) and (b)shows the calculated strain distribution for the relaxed NW2 displayed along its longitudinal direction (by relaxed, we mean a wire not subjected to any external deformation). Two main characteristics can be observed in Fig. 6.9(a) and (b): (i) the NW core (plateau regions) appears positively strained in all directions; (ii) drastic fluctuations of strain take place at the twin-plane interfaces. In order to probe the effects of an external deformation, tension and compression were applied on the NW2 along the z-direction, to obtain deformations ranging from -1.0% to +1.0% in their longitudinal length at $T \sim 0$ K. The resulting diagonal strain components for the externally strained wires are displayed in Fig. 6.9 (c) and (d). Notice that the diagonal strain components perpendicular to the longitudinal direction (ε_{11} and ε_{22}) are shifted to positive (negative) values due to positive (negative) uniaxial strain applied in the nanowire. Nevertheless, the diagonal strain components ε_{33} has an opposite behavior and is shifted to negative (positive) values under positive (negative) uniaxial applied stress.
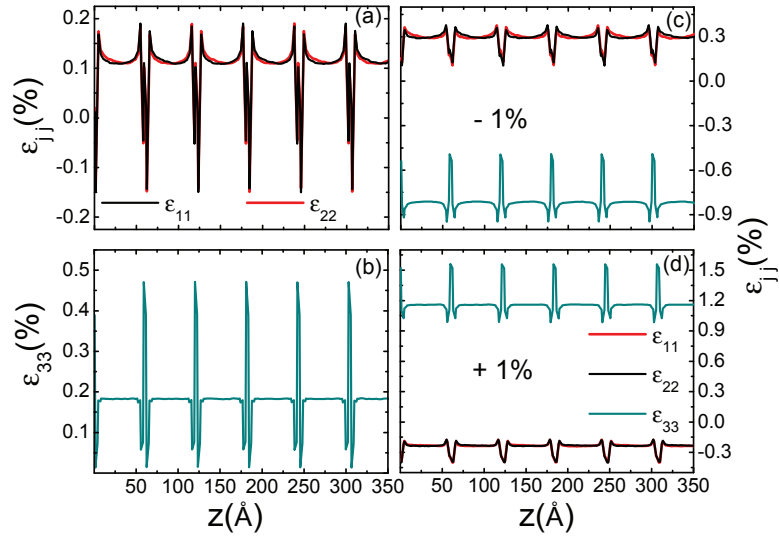
Fig. 6.9: Average values of the central strain distributions along longitudinal direction [111] of the NW2 showing the possible types of twin-plane superlattice structures. Panels (a) and (b) are for relaxed NW; Panels (c) and (d) are for externally strained NW. In panel (c) the wire is under compression and in panel (d) the wire is under tension. In panels (c) and (d), the black solid line represents ε_{11}, the red line is ε_{22} and the dark cyan line is ε_{33}.

6.2.2 Electronic properties

The most common superlattices [117] are formed by alternating layers of two different semiconductors. Because different materials have a distinct band gap, there will be a discontinuity in the potential profile at the interfaces. As a result, the electronic structure of a superlattice behaves as a sequence of quantum wells separated by barriers. This periodic sequence of quantum wells and barriers creates a miniband structure, which is constituted of alternated regions of allowed and forbidden energies. The regions of allowed energies correspond to hybridization of quasi-bound states that are localized between the barriers. Therefore, carriers can efficiently tunnel through the superlattice when their energy reaches these allowed regions and the structure becomes transparent for the electronic transport. Obviously, these phenomena are observed if the quantum wells have a minimum size and height capable of forming quasi-bound states. In addition, the heavier the effective mass of the carrier, the easier the formation of a quasi-bound state.

In this section, we use the calculated intrinsic strain fields of NWs, which appear due to the arrangement of atoms during the formation of the wired structure, together with external deformations to show that twin-planes NWs behave as 1D superlattices. Mainly, the impact of strain fields on the band structure will be given by a shift in the
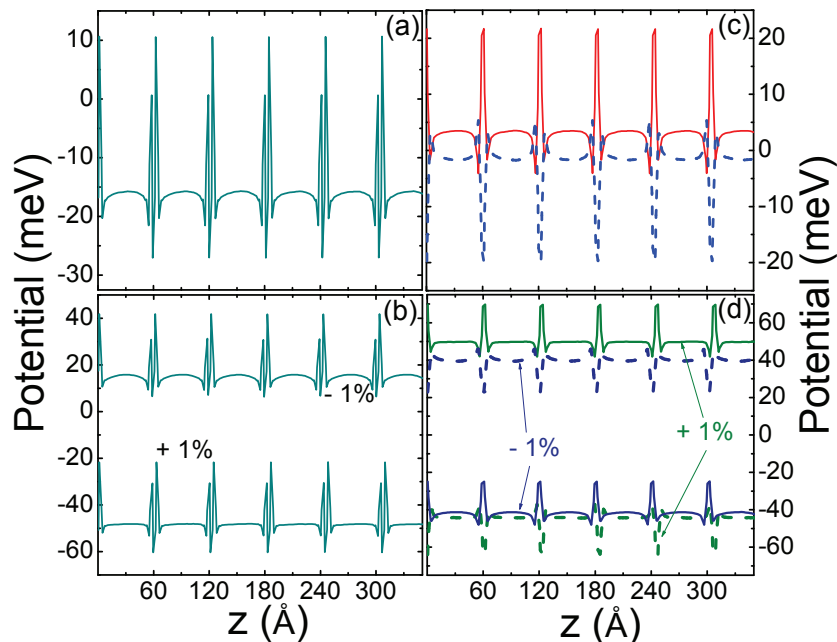
Fig. 6.10: Calculated effective superlattice potential along [111] direction at the NW2 core. Panel (a) is the conduction band profile for the relaxed NW2. Panel (b) is the conduction band profile for the externally strained NW2, considering the wire subjected to +1% tension (upper trace) and subjected to −1% compression (lower trace). Panel (c) is the valence band profiles for the relaxed NW2. The solid red lines describe the heavy-hole profile and the dashed blue line the light-hole profile. Panel (d) is the valence band profiles for the externally strained NW2 under +1% tension (upper traces) and for −1% compression (lower traces). In all panels we adopted the point of view of a valence band electron as the reference to describe the potential profile.

conduction and valence-band edges and a split of the degeneracy of the heavy- and light-hole subbands.

The change on the effective potential profile for conduction and valence bands can be ascribed to the influence of the deformation potentials: a, b, and d, for a given strain field configuration. [103] In particular, the effect on the conduction band is isotropic [118] $\mathcal{H}_{cond} = a_c\left(\varepsilon_{11} + \varepsilon_{22} + \varepsilon_{33}\right)$, where a_c is the conduction band deformation potential. In turn, the potential profile for the valence band is anisotropic, and a rotation in the Bir-Pikus Hamiltonian [119] should be performed. [120] For [111] direction, the energy shifts for heavy- and light-hole subbands are respectively $\mathcal{H}_h = -a_v\left(\varepsilon_{11} + \varepsilon_{22} + \varepsilon_{33}\right) - \frac{d_v}{\sqrt{3}}\left(\varepsilon_{11} + \varepsilon_{22} - \varepsilon_{33}\right)$ and $\mathcal{H}_l = -a_v\left(\varepsilon_{11} + \varepsilon_{22} + \varepsilon_{33}\right) + \frac{d_v}{\sqrt{3}}\left(\varepsilon_{11} + \varepsilon_{22} - \varepsilon_{33}\right)$, where the valence band deformation potentials are labeled by a_v and d_v.

The calculated potential profile induced by strain for electrons along [111] direction for the relaxed and for the externally strained NW2 are displayed in Fig. 6.10 (a) and (b), respectively. It can be noted in both cases that there are fluctuating potentials at

the positions where an interface between the twin-planes occurs. Such fluctuations act as potential barriers for electrons alternated by quantum wells, thus constituting a 1D superlattice. The difference provided by external strain is a shift in the bottom of the conduction band, which is positive (negative) for the compressive (tensile) case. For NW2, the thickness of the quantum wells is approximately 45 Å separated by barriers of thickness approximately 15 Å. The potential profiles for NW1 (results not shown here) and NW2 are very similar and the only difference between them is related to the size of the barriers and wells. For NW1, the thickness of the barriers is approximately 5 Å and the thickness of the quantum wells is close to 15 Å. For both NW1 and NW2, the average height of the barriers have the same value, which is approximately 15 meV (see Fig. 6.10).

For the valence band, we have two distinct situations to consider according to the heavy- or light-hole subband character of the carrier. Here, the profile corresponds to the potential from the point of view of a valence band electron. According to Fig. 6.10 (c) and (d), we can observe that the heavy-hole and conduction subbands have similar profiles and follow a sequence of quantum wells separated by barriers (positive fluctuating potentials). On the other hand, the light-hole subband profile presents an inverted sequence of quantum wells (negative fluctuating potentials) and barriers. Therefore, depending on the characteristic of the valence band ground-state, the holes can be confined into different layers of the structure when compared to electrons at the conduction band. Such a tuning of the ground-state can be performed by applying an external strain (Fig. 6.10 (d)). Furthermore, one can notice, in Fig. 6.10 (c) and (d), that the valence band ground-state has a heavy-hole character for both relaxed and under tension (+1%) wires while the light-hole character dominates for NWs under compression (-1%). As we will see bellow, this alternation will also affect the transport properties of the NWs.

6.2.3 Transport properties

To characterize carrier transport properties in the 1D superlattice described by the calculated potential profiles, we use the formalism based on the transfer matrix method [83]. The transmission probability was calculated for different combinations of wire sizes and strain configurations. In this work, we consider the transport of both type of carriers: electrons at the bottom of the conduction band and holes at the top of the valence band. Figure 6.11 shows the transmission probability for electrons at the conduction band of
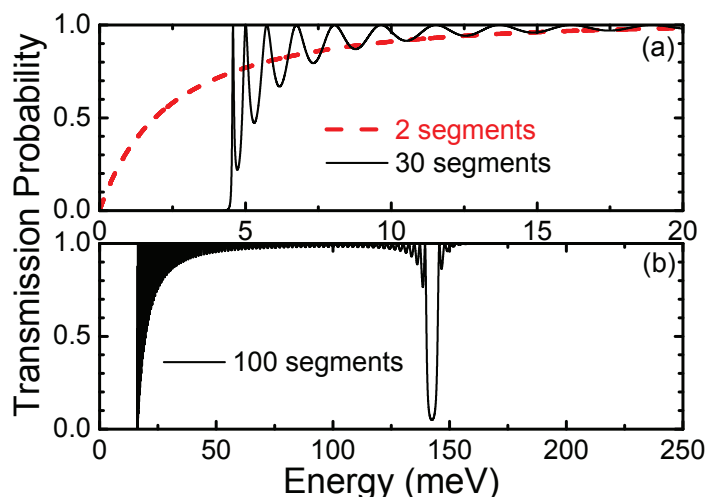
Fig. 6.11: Transmission probability for carriers at the conduction band as a function of the electron energy for NW2, which forms a twin-planed superlattice constituted of (a) 2 (dashed line) and 30 segments (solid line) and (b) 100 segments. The full transparency condition for the system is achieved when the transmission probability reaches 1. In all cases the energy has been measured from the corresponding band minimum.

the NW2 considering different number of superlattice segments. Also, one can observe in Fig. 6.11 (a) and (b) that the transmission probability is very close to 1 when electron energy is higher than 15 meV. Such a result indicates that the twin-plane superlattice is almost fully transparent for electrons. Because the external strain only shifts the conduction band edge (see Eq. (6.8)), we can affirm that the transmission probability for electrons does not depends on the external deformation. The effects of the potential profile are stronger when the electron energy is smaller than 20 meV. In this case, we can observe quantum interference features (see Fig. 6.10) depending on the number of segments, but there is no observation of a resonant peak due to the small electron effective mass. The qualitative picture for electron transmission probability for both NW1 (results are not shown here) and NW2 is practically the same. This conclusion comes from the fact that electronic structure of both NWs only differs from each other by the thickness of the quantum wells and barriers. Therefore, if there is no quasi-bound state for wider quantum wells (NW2), there will not be one for narrower wells (NW1).

In contrast, the transmission probability for holes at the valence band can be effectively modified by applying an external strain, as depicted in Fig. 6.12 and Fig. 6.13. In both figures, NW1 and NW2 were probed by increasing the number of twin-plane segments. When the NW is subjected to compression (Fig. 6.12), the light-hole is the preferential type of carrier and the transparency of the superlattice is evident since the transmission

probability is close to 1 and there is no observation of a resonant peak. Again, this effect is a characteristic of the small mass of this type of carrier. The transmission probability is also quite similar for NW1 (results are not shown here) and NW2, when the NWs are under compression. On the other hand, clear resonant transmission conditions are achieved for either relaxed NWs or under tensile stress at some energy values, because now the heavy-hole is the preferential carrier type. For the NW1, we observe only one sharp peak at the energy $\sim$ 20 meV (Fig. 6.13 (a)). Alternatively, for the NW2, two very sharp peaks in Fig. 6.13 (b) can be noticed, with energies at $\sim$ 15.5 meV and $\sim$ 22 meV, respectively. In these both cases, the states with the heaviest mass along the [111] direction are promoted to the top of the valence band (ground-state) and the full transparency of the twin-plane superlattice is no longer observed. Thus, transparent energy bands are alternated between opaque energy gaps. According to the number of twin-plane segments, the transparency contrast can be enhanced as shown in Figs. 6.11-6.13.

6.2.4   Conclusion

In summary, the transport properties can be tuned in twin-plane superlattices within semiconductor NWs even in the case of the Γ-electrons of zincblende like systems in contrast to the apparent transparency expected for 2D heterostructures. [21] The application of external stress or any other mechanism that induces strain, such as temperature, [67]
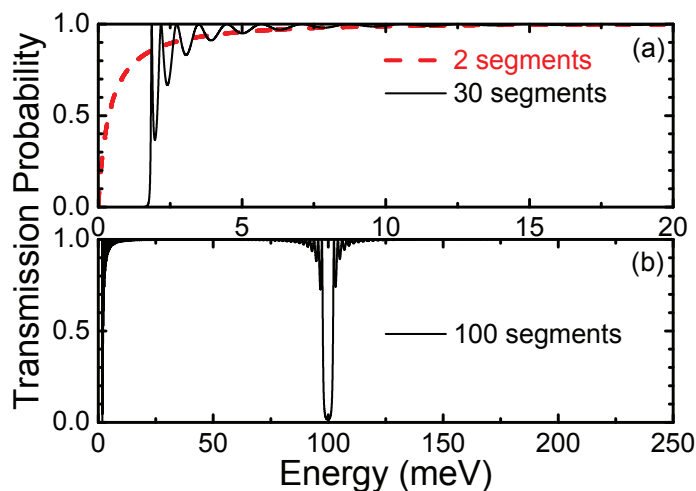
Fig. 6.12: Transmission probability for carriers at the top of the valence band as a function of the hole energy for the NW2 under compression. The twin-plane superlattice is constituted of (a) 2 (dashed line) and 30 segments (solid line) and (b) 100 segments. The full transparency condition occurs when the transmission probability is equal to 1. In all cases the energy has been measured from the corresponding band minimum.
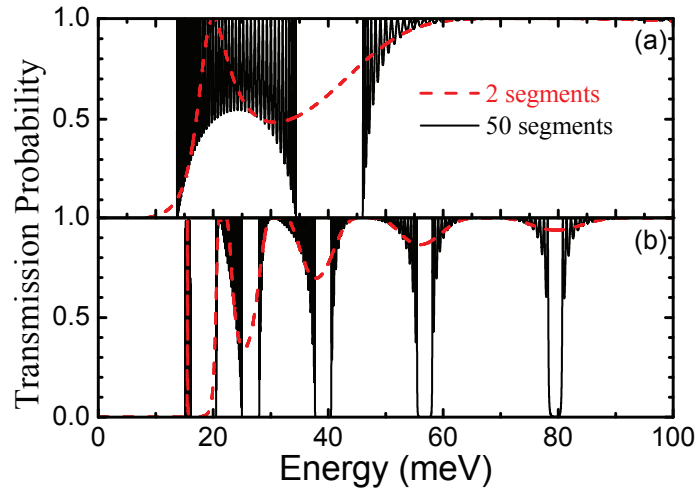
Fig. 6.13: Transmission probability for carriers at the top of the valence band as a function of the hole energy for relaxed NWs or under tension: (a) for the NW1 and (b) for the NW2. The dashed (solid) line is the transmission for a NW composed of 2 (50) segments. The full transparency condition occurs when the transmission probability is equal to 1. In all cases the energy has been measured from the corresponding band minimum.

can be an effective tool to reach alternate conditions between almost full transparency and opaqueness. The increment of twin-plane segments is definitively a way of increasing the contrast between these situations. To conclude, we have shown that to explore twin-plane superlattices as active part of nanocircuits can be successfully achieved if the external control of such strain dependency is mastered.

7. QUANTUM DOT CHAINS

Progress in nano-scale electronics architectures and the continuous search for ultra-small circuit components have resulted in increased interest in the unique properties of low-dimensional systems such as quantum wires (QWRs) and coupled quantum dots (QDs). Recently, using molecular-beam epitaxy and strain engineering, a unique system of aligned quantum dots, i.e., quantum dot chains (QDCs), were successfully synthesized [1, 2]. In previous reports, using structural and optical characterization techniques, it was shown that the QDC systems have a complex band structure caused by the combination of two-dimensional (2D), one-dimensional (1D) and zero-dimensional (0D) densities of states [65, 66]. In this regard, systems of 1D coupled QDs have attracted much attention both in order to understand the underlying physics [67] and to develop novel devices. The co-existence of 2D and 1D states, that are important for enhanced electrical conductivity, as well as 1D and 0D states, that can play a role in the suppression of thermal conductivity, also makes this system a potential target for development of thermoelectric applications [68].

In collaboration with the experimental group of Prof. Greg Salamo from University of Arkansas, where electron transport in a system of QDCs was investigated, we developed a 1D hopping model in order to characterize the transport in this kind of system. The presence of 0D states on top of a 1D wetting layer (WL) makes the electron transport in QDCs different from a system of continuous wires. This results in a different anisotropic response as well as enhanced hopping at low temperatures. Also, the transport was probed with respect to band filling phenomena by supplying various concentrations of free carriers through remote doping in the GaAs barriers. Thus, the effect of changing the relative position of the Fermi level can be determined.

Figure 7.1 presents representative atomic force microscope (AFM) images of the QDCs in the samples. The long chains of InGaAs QDs are well organized parallel ($\parallel$) to the [$\bar{1}$10] crystallographic direction over long distances and perpendicular ($\perp$) to the [110] direction
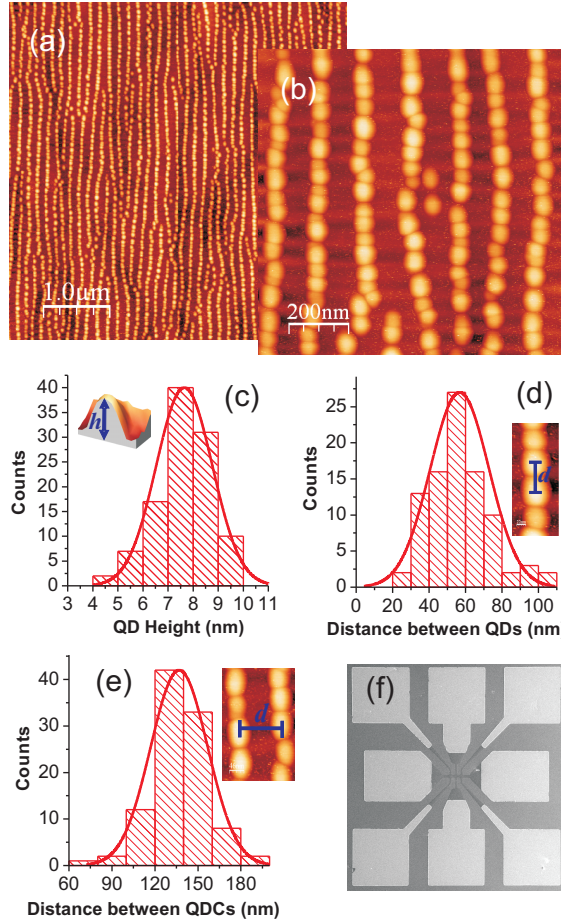
Fig. 7.1: (a) $5 \times 5~\mu\text{m}^2$ AFM topography image of QDC sample C. The chains are aligned along the $[\bar{1}10]$ crystallographic direction; (b) $1 \times 1~\mu\text{m}^2$ AFM image of the same sample; Statistical distribution with Gaussian fits of the: (c) QD height; (d) Distance between QDs, d_{in}, within the chains (peak-to-peak) measured along $[\bar{1}10]$ direction; and (e) Distance between neighboring chains, d_{bc}, measured peak-to-peak; (f) Hall bar structure used for electrical characterization with a channel width of $25~\mu\text{m}$. [123]

which runs across the chains. AFM analysis of the surface QDCs, Figs. 7.1c-e, has revealed the average height of the QDs, the average radius of the QDs, the average spacing of the QDs within a chain, and the average chain to chain spacing to be: $h \sim 7.6$ nm, $r \sim 27$ nm, $d_{ic} \sim 57$ nm, and $d_{bc} \sim 137$ nm respectively. These dimensions are important for understanding the electronic structure of the system and the underlying anisotropy. All of these structural parameters of the QDC systems have a normal distribution and are well fit by Gaussians.

The conductance in this system is governed by two main factors: (i) available states of different dimensionality and (ii) the position of the Fermi surface across the entire structure. In order to understand the role of these factors, let us first discuss possible conduction mechanisms through the states of different dimensionalities that lead to chan-

nels with different transmission probabilities. The total conductivity in the system of QDCs can be written as

$$\sigma_\xi = \sigma^{3DGaAs} + \sigma^{2DWL} + \sigma_\xi^{1DWL} + \sigma_\xi^{0D}, \tag{7.1}$$

where ξ denotes the $[\bar{1}10]$ and $[110]$ directions. The conductivity in bulk GaAs, σ^{3DGaAs}, and in the 2D InGaAs wetting layer, σ^{2DWL}, are considered to be isotropic. The main source of anisotropy will be that due to the 1D wetting layer, $\sigma_{ij}^{1D,WL}$, formed due to the strain fields developed in-plane and along the growth direction [65, 66]. The difference, $\Delta\sigma^{1DWL} = \sigma_{[\bar{1}10]}^{1DWL} - \sigma_{[110]}^{1DWL} > 0$, is determined not only by the lateral confinement in the $[110]$ direction but also by lateral chain spacing in the $[110]$ direction, d_{bc}. Indeed, due to the high lateral spacing, $d_{bc} = 137$ nm, transport through 1D states in the $[110]$ direction is only possible with the participation of the 2D states of the InGaAs WL and the 3D states of GaAs [122].

To study the conductance in the samples, conduction was forced through different dimensionality of the systems by moving the Fermi surface across it. Experimentally, they used temperature dependent Hall effect measurements. Figures 7.2 (a) and (b) present the Hall mobility and electron sheet density, respectively. These measurements were performed for each sample using Hall bars (see Fig. 7.1 (f)) aligned along the $[110]$ or $[\bar{1}10]$ crystallographic directions, i.e., across the QDCs or along them. Here, several distinct, noteworthy features were found: (i) the absolute value of the mobility is strongly dependent on remote doping concentration; (ii) the anisotropy ($\eta = \sigma_{[\bar{1}10]}/\sigma_{[110]}$) is dependent on the temperature (Fig.7.2 (c)); and (iii) the low temperature mobility ($T < 90$ K) progressively decreases with doping. At high temperatures, mobility along the chains shows only a slight variation with doping. At the same time, the high-temperature mobility across the QDC is obviously affected by the doping levels. This observed difference is small but is the result of the anisotropy in the conductivity of the 1D WL and of the QD chains. This is only observable due to the lowering of the Fermi energy with the decreasing doping level into the states of the lower dimensional systems. In other words, if the doping level was very high, into the GaAs conduction band, no anisotropy in the conductivity was expected to be seen.

At higher temperatures, they found that the mobilities decrease as the temperature rises. There are two effects which contribute to this decrease: the modulation of QD
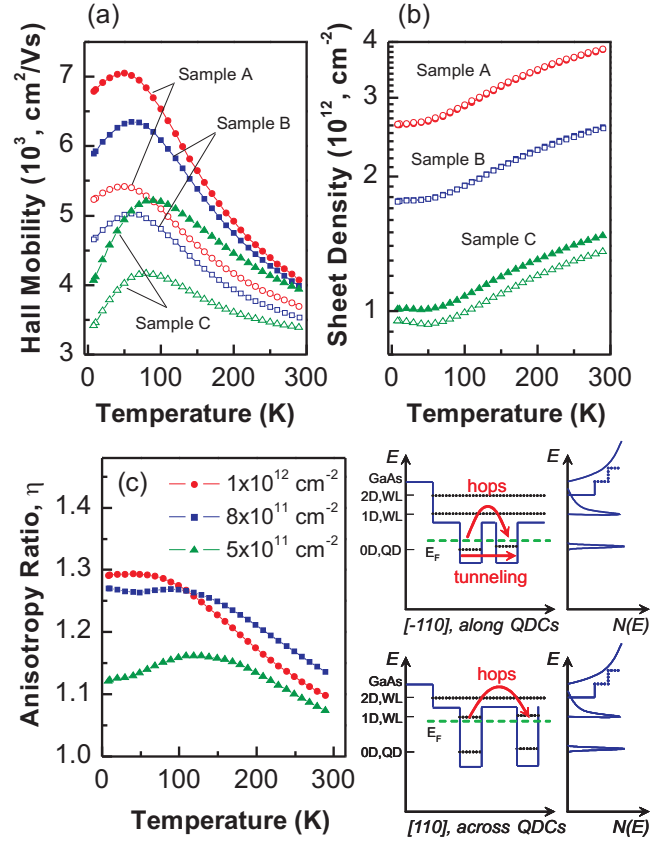
Fig. 7.2: (a) The Hall mobilities and (b) the electron sheet densities measured as a function of temperature for samples A, B, and C along the QDCs ($[\bar{1}10]$ direction, solid symbols) and across the QDCs ($[110]$ direction, open symbols); (c) Anisotropy as function of temperature and remote doping for samples A, B, and C. The inset shows a schematic band diagram in the (100) plane for $[\bar{1}10]$ (along QDCs) and $[110]$ (across QDCs) crystallographic directions as well as the density of states diagrams.

occupancy which inhibits hopping, as described before, and the increase in scattering rate by phonon interaction [124]. At temperatures below 100 K, the electron mobility reaches the maximum and starts to decrease again towards lower T. This decrease of mobility cannot be associated with enhanced scattering on ionized impurities at low temperatures because the thick spacer layers at 17.5 nm prevent it [124]. Instead, the mobility decrease here is due to the cross-over between 1D states in the InGaAs WL [122] and 0D states in the QDs. The decrease of doping and temperature makes these states dominant in charge transport. Hopping conduction becomes a dominant mechanism at lower temperatures which results in the observed drastic mobility decrease as T decreases.

Figure 7.2 (c) presents the experimental results of the anisotropy, η, as functions of temperature and doping level. Notably the QDCs behave differently with temperature and doping than a QWR system [122]. For QDCs, an interference of channels of a different

nature may occur. The presence of QDs with 0D states effectively localizes carriers, reduces the charge transport in both [$\bar{1}$10] and [110] directions, and leads to the peculiar behavior displayed in Figure 7.2 (c). At room temperature, for the highest remote doping of 1×10^{12} cm^{-2}, Sample A, the anisotropy is less than for the moderately doped Sample B, $N_{2D} = 7.5 \times 10^{11}$ cm^{-2}. This is an indication that the isotropic 2D states of the InGaAs WL and even the GaAs contribute to the conductance in Sample A, while for sample B the lower Fermi energy enhances conduction in the anisotropic 1D states. However, for Sample C, the Fermi level is lowered further into the 0D states of the QDs where hopping conduction dominates. This leads to lower anisotropy.

For all samples, decreasing the temperature leads to an increase in anisotropy as expected due to pinning of the Fermi energy in the 1D states. However, for Samples B and C at ~ 110 K, the anisotropy reaches its maximum and decreases slightly.

7.1 Hopping transport

In order to assess the anisotropy and the temperature dependence of the mobility of carriers through the QDs, we will consider a model based on hopping transport [32, 33, 34, 35, 36] that will take into account the structural parameters of the real samples. Using the QDs as localization centers for charge carriers, the dot-to-dot transport along the chain or from chain-to-chain occur when an electron gains enough energy to escape into the barrier by absorbing phonons. Here, we consider a system of 10 chains with 1724 QDs each, in other words, we have calculated the mobility of a system of 10 by 1724 confining sites (QDs) by considering hoping between them. Labeling the QDs with an index, k, their occupation density is given by the Fermi-Dirac distribution

$$n_k = \frac{1}{1 + e^{\beta(\Delta + (k-1)V)}}, \tag{7.2}$$

where $\beta = (k_b T)^{-1}$, k_B is Boltzmann's constant, V is the drop in energy of each site due to an applied voltage, and $\Delta = \mathcal{E} - \mathcal{E}_\mathrm{f}$ is the energy difference between the hopping energy state and the Fermi energy.

According to Miller and Abrahams [32], the transition rate for hops from one site to

another with relative position vector $\mathbf{r}_{kl}$ is given by

$$R_{kl} = \begin{cases} \nu_0 e^{-a|\mathbf{r}_{kl}| - \beta(\mathcal{E}_l - \mathcal{E}_k)}, \mathcal{E}_l > \mathcal{E}_k \\ \nu_0 e^{-a|\mathbf{r}_{kl}|}, \qquad\quad \mathcal{E}_l < \mathcal{E}_k \end{cases} \tag{7.3}$$

where ν_0 is an intrinsic transition rate, $a = 2/\alpha$ with α being the localization radius, and ϵ is the energy which includes the contribution of V. Therefore, the mobility can be calculated as

$$\mu_\xi = \frac{r_0}{\mathbf{E} < n_k^0 >} \sum_k \sum_l \left[\mathbf{r}_{kl} R_{kl}^{(\xi)} n_k (1 - n_l) + \mathbf{r}_{kl} R_{kl}^{(\xi)} n_l (1 - n_k) \right], \tag{7.4}$$

where $\mathbf{E}$ is an applied electric field, r_0 is the lattice constant, and n_k^0 is the equilibrium Fermi-Dirac distribution (r_{kl} and α are given in units of r_0).

Within a strictly hopping formalism using a uniform 1D chain, there are only two mechanisms which can cause the transport properties to vary with direction resulting in anisotropy: the anisotropic effects of the electron-phonon interaction and the effective number of parallel sites contributing to the hoping mobility in each direction. The effect of increasing the number of distant hops is displayed in Figs. 7.3 (a) and (b) using the sample parameters as measured in Fig. 7.1. We calculated the mobility for both directions, across and along the chains, Figs. 7.3 (a) and (b) respectively, with different numbers of neighbors contributing to the hopping mechanism. The index l, in Eq. (7.4), runs through the values 1 to l_{max} as indicated along each curve in Fig. 7.3, and where l_{max} is the maximum number of neighbors considered in the calculations. As we can see, the mobility increases as we include more nearest neighbor hopping sites in the calculations. By fixing the number of neighbors involved in the hopping, the role of the parameter Δ, i.e., the Fermi level, in the mobility is assessed in Figs. 7.3 (c) and (d), across and along the chains, respectively. The farther the Fermi level is from the energy level of state which is being considered for hopping, the higher the temperature where the maximum mobility is attained. Such a behavior is attributed to the temperature dependence of the relative occupancy of the sites.

As predicted by the 1D model, the change in the Fermi level position by varying the doping density leads to the systematic shift of the mobility maximum, Fig. 7.2. This non-monotonic behavior is a signature which is expected for hopping (see Fig. 7.4). This
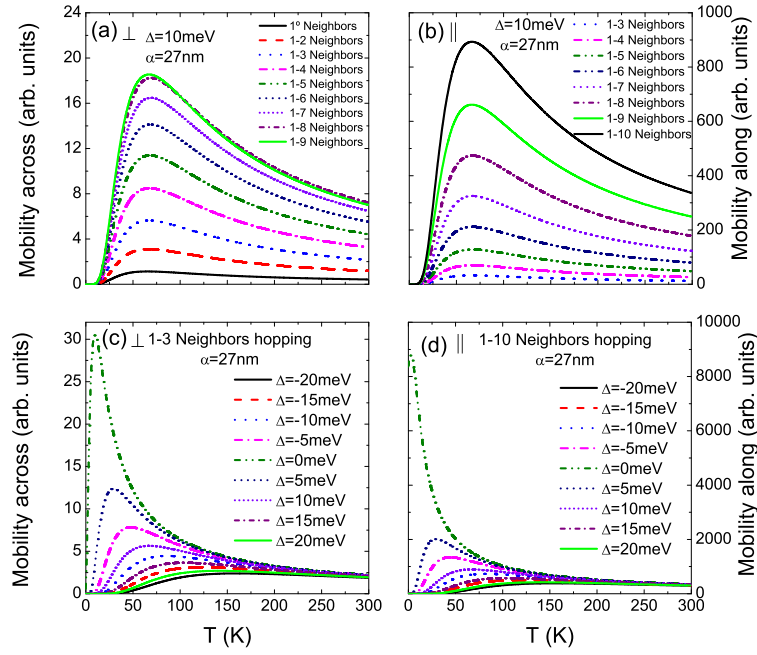
Fig. 7.3: Mobility versus temperature for $\alpha = 27$ nm. (a) Across the chains and (b) along the chains, both showing the effects of changing the number of neighbors involved in hopping. (c) Across the chain, for hops between the 3rd closest neighbors, varying Δ. (d) Along the chain, for hops between the 10th closest neighbors, varying Δ.

behavior is enhanced in the lightly doped sample C, $N_{2D} = 5 \times 10^{11}$ cm^{-2}. This sample shows the smallest conductance anisotropy between the three samples, however its temperature dependence is completely different than the one obtained for QWRs, [122] where the highest η was measured for the sample with the lowest doping level. This suggests that for conduction in the QDC system the 0D states dominate over the 1D and 2D states. In sample C, at $T \sim 110$ K the anisotropy rapidly starts to decrease with temperature, similarly to sample B. This decrease of anisotropy with temperature as well as the sharp drop in mobility at low temperatures indicates that QDs dominate the transport. As shown by the schematic diagram in the *inset* of Fig. 7.2, when the Fermi energy is low enough and is in the 0D states of QDs, the transport will be governed by electron hopping in both the [110] and [$\bar{1}$10] directions.

Now, we will demonstrate that this relative position of the Fermi energy impacts the anisotropic transport response in a system of 1D QDCs. We can calculate the conductance by considering just the first neighbor hopping [33]. The conductance in a 1D system of confining sites, the QDs, is equivalent to a model of conductors connected in series. The
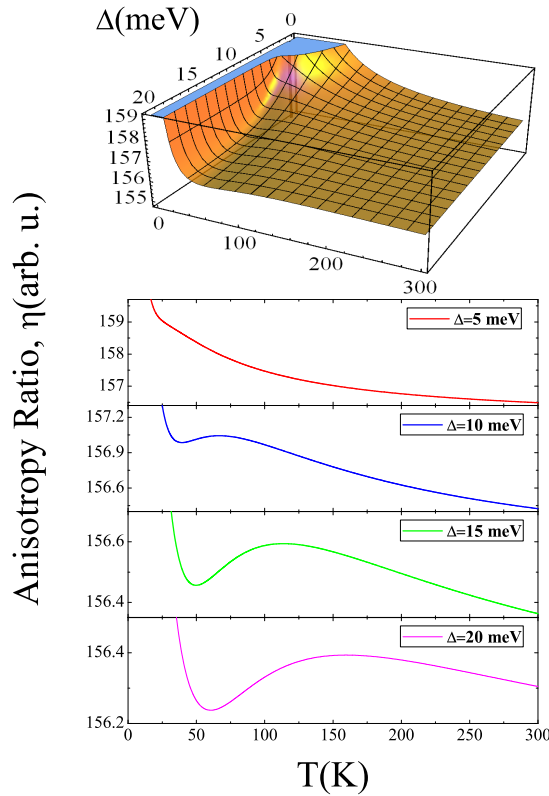
Fig. 7.4: Anisotropy ratio as a function of both temperature and Δ. The upper panel shows the complete 3D plot of this surface. The lower panel shows temperature profiles at different values of Δ. With the narrow vertical scale here, it is easy to see the evolution of the maxima of the anisotropy ratio as Δ increases.

conductivity would then be:

$$\sigma_\xi = N\alpha e^2 \beta \left[\sum_k \left(n_k(1-n_k) R^{(\xi)}_{k,k+1} \right)^{-1} \right]^{-1}, \tag{7.5}$$

where N is the number of sites. The anisotropic behavior will be assessed through the anisotropy ratio defined as $\eta = \sigma_{[\bar{1}10]}/\sigma_{[110]}$, using Eq.(7.5) for the σ. Figure 7.4 shows the anisotropy ratio as a function of temperature and the relative position of the hopping state with respect to the Fermi energy, Δ. Note that this result is merely qualitative, since no attempt was made to include realistic values of the constants that enter Eqs. (7.3) and (7.5). A continuous increase of Δ produces qualitative changes on the anisotropy as a function of temperature. For lower values of Δ, the anisotropy ratio with temperature decreases monotonically while for higher values, the behavior becomes non-monotonic with a definite maximum. In the model, the Fermi energy and temperature appear combined within the Fermi-Dirac distribution. Thus, as expected for high temperatures, the carrier

distribution is smeared and no essential differences can be observed in the occupation of neighboring sites, leading to a thermalized picture.

Even though, the response of the samples matches qualitatively with the model of electron hopping, we would like to investigate the possibility of finding evidence of variable-range hopping [125] in our conductivity data. Ideally, this would obey Mott's law, which is given by

$$\sigma_\xi^{0D}(T) = \sigma_0^{(\xi)} e^{-\left(\frac{T_0^{(\xi)}}{T}\right)^x}. \tag{7.6}$$

Here, $T_0^{(\xi)} = 13.8/k_B N(\mathcal{E}_f)\alpha^2$, is determined by material properties, $N(\mathcal{E}_f)$ is the density of states at the Fermi level, and $x = 1/3$ for phonon assisted hopping conductivity. The parameter $\sigma_0^{(\xi)} = \gamma^{(\xi)} T^m$, with $\gamma^{(\xi)}$ - the temperature independent parameter reflecting the characteristic frequency of hopping "attempts" and $m = -1$ [125, 126, 127]. To characterize the temperature dependence of this variable-range hopping component of the conductivity $\sigma_\xi^{0D}(T)$, we followed the differential method proposed in [128, 129], in which $\sigma_0^{(\xi)}$ is allowed to vary. In order to analyze the data, we consider the function [128]

$$W_\xi(T) = \frac{\partial \log \sigma_\xi(T)}{\partial \log T} = m + \left(\frac{T_0^{(\xi)}}{T}\right)^x. \tag{7.7}$$

For $m \ll x(T_0^{(\xi)}/T)^x$, we can write $\log W_\xi(T) = A_\xi - x \log T$, where $A_\xi = x \log T_0^{(\xi)}$. The plots of $\log W_\xi(T)$ vs. $\log T$ are shown in Fig. 7.5, for conduction both along and across the QDCs.

Certainly, a uniform 1D chain, as modeled before, cannot be fitted into the random picture of a disordered system where the variable-range hopping takes place. Thus, it is not surprising that the calculated values of $\log W_\xi(T)$ vs. $\log T$ differ from the Mott law already at low temperatures, as depicted in Figs. 7.5(a)-(d). The behavior does not depend on the number of distant hops involved in the calculations, Figs. 7.5 (a) and (b). Also, by varying Δ, the uniform chain response still deviates from the Mott law, as depicted in Figs. 7.5 (c) and (d), and the curves shift for each value of the relative hopping state position with respect to the Fermi energy.
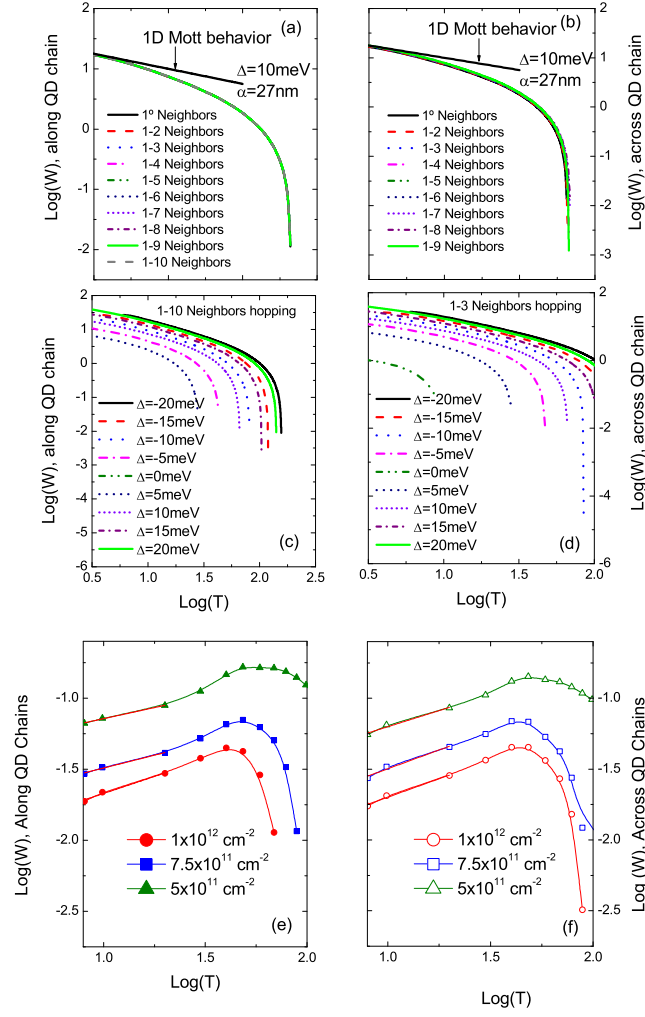
Fig. 7.5: $\log(W_\xi)$ versus $\log(T)$. (a) and (b) along and across QD chain, respectively, with different number of hopping neighbors. The 1D Mott behavior ($x = 1/2$) is shown by solid line. (c) and (d) along and across QD chain, respectively, where Δ is varying. (e) and (f) are experimental data.

7.2   Conclusions

In summary, detailed studies of the mechanisms of conductance in a system of quantum dot chains as a function of temperature and remote doping level have been performed. We demonstrated that the behavior of the conductance is complicated due to the availability of states of different dimensionalities. We found that the presence of 0D states plays a key role in the anisotropic behavior of the conductance in this system and compared the experimental response to a 1D hopping model. At low temperatures, the experimental response of all samples deviates from Mott's law of conduction.

Figures 7.5 (e) and (f) show the experimental values of the mobility analyzed using Eq. (7.7). Deviations from the Mott behavior are predicted for variable-range hopping at

low temperatures and obtained where a 1D ordering of sites in the chain creates a system size that is comparable to the typical length of a hop [130, 131, 132, 133]. However, in our case, the divergence at lower temperatures does not fit into these predictions. Yet, as the carrier concentration varies, the curves in Figs. 7.5 (e) and (f), are shifted analogously to the prediction of the theoretical calculations in Figs. 7.5 (c) and (d). Thus, one may conclude that the qualitative discrepancy between experiments at low temperature with the Mott law and the 1D hopping model does not depend on the position of the Fermi energy. We were not able to determine the reason for such a behavior and this has opened an intensive search for a more systematic study of the conductivity in these QDCs. Certainly, the combination of various channels masks each other and assessing the nature of the main transport mechanisms within the whole temperature range is a task that requires further work.

For high doping levels, the conduction through energy states of 1D and 2D systems may interfere. However, even for this case, the conductivity, σ_ξ, is modulated by a hopping component of σ_ξ^{0D} through localized levels in the QDs. For low doping, when the Fermi surface is mainly located in these 0D states, the hopping conductance is dominant and conduction through the 1D and 2D states is only possible through electrons scattered into higher energy states. Further decrease of sample temperature could bring our system into the regime of long-range Coulomb interaction, where hopping conduction is possible without phonon assistance. This will be a subject of our further studies.

8. FINAL CONSIDERATIONS

In this thesis, we have studied the transport properties in quasi-one-dimensional heterostructures. Specifically, we have characterized the transport of semiconductor NWs, coupled NWs, twin-plane NWs, heterolayered systems, and quantum dot chains and studied the theoretical grounds, both semiclassical and quantum, to support these analyzes. Initially, through the $\mathbf{k} \cdot \mathbf{p}$ approach, we have studied the electronic structure of NWs and their quantization effects for different geometries. The structure of the valence band was calculated from the diagonalization of the Luttinger Hamiltonian [72]. The calculation of its matrix elements was obtained analytically, which provided well determined selection rules that enabled us to split the Hilbert space into orthogonal subspaces. All these mathematical results facilitated the numerical diagonalization and the subsequent qualitative discussions. Adding strain effects to the model, allowed tuning the character of the valence band ground state. This became a very important result since we were able to promote light-holes to the ground state and make this carrier as important as the electron in terms of mobility. Then, by tuning adequate structural parameters, the heavy-holes may attain the valence band top and were able to obtain transport opaqueness in structures where full transparency was predicted. [63, 64]

The hole mobility, affected by the hole-phonon interaction in InP semiconductor NWs, for different geometries, and under various strain and temperature conditions, was systematically studied. We showed that the mobility changes according to the NW width, strain fields, and temperature in a non-monotonic fashion for certain parameters. This is explained by the fact that the electronic structure changes drastically with strain and/or size, with the ground state switching character between heavy- and light-hole, while the temperature changes of the LO peak position and size, supported by the molecular dynamics calculations, are also important. Furthermore, we have characterized the resonant behavior of the mobility when the energy separation between the two valence subbands equals the optical phonon energy. These conditions can be tuned by size variation or strain

fields and are also affected by temperature, and should be taken into careful consideration when designing possible NW-based device.

Inspired on the idea of designing new devices, we revisited a well developed concept: the waveguide directional coupler, [46, 47]. We proposed and developed the study of the spin transport properties of a nanowire directional coupler ("H-shap" geometry) implemented by parallel wires joined by a mixing region, locally gated, which generates Rashba spin-orbit interaction. Moreover, various configurations of gate voltages applied on the wire structure were considered. Under this configuration, we were able to analyze the modulation of the spin transport through the combination of SOI and system dimensions. The combination of SOI and gate voltages allows a modulation of the polarization, when the measured spin is projected along the direction of the Rashba spin-orbit field. The overall control of charge and even spin flux in this system appears promising for spintronics, as well as in hybrid devices that include nearby superconducting or magnetic materials.

The amazing recently advances in growing nanostructures technics allowed the controlled synthesis of stacking fault heterostructures of III-V compound semiconductors NW. [3, 4] Such microscopic control of the crystalline structure, during the nanowire synthesis, open up opportunities for a thorough modulation of their electronic structure and thus their potential use as quantum heterodevices. We systematically analyzed the structural properties of twin-plane superlattices in InP NWs by join efforts. Through molecular dynamics, a NW in [111] direction was simulated to determine the strain fields produced by the formation of twin-planes and surface effects. Changes on the electronic structure of these NWs due to the stress tensor obtained from molecular dynamics simulations were described. Based on these results, we have confirmed that a one-dimensional superlattice is indeed formed in quantum level. The application of external stress or any other mechanism that tunes the strain, such as temperature, can be an effective tool to reach alternate transport conditions between almost full transparency and opaqueness. In this way, we have describe the transport properties of both electrons and holes in theses structures. In contrast to the predicted transparency of Γ-electrons in heterolayered III-V semiconductor superlattices, we verified that transport properties can be effectively tuned in twin-plane superlattices within semiconductor NWs even in the case of Γ-electrons of zincblende systems. The increment of the number of twin-plane segments is definitively

a way of increasing the contrast between these situation and open up possibilities of electronic structure engineering and the modulation of transport and optical responses.

Following the trend of the field, collaborators brought to our attention some interests results on quantum dot chains (QDCs), where electron transport was investigated. In this systems, the presence of 0D states on top of a 1D wetting layer (WL) makes the electron transport different from the case of continuous wires. This results in a different anisotropic response as well as enhanced hopping at low temperatures. Moreover, the transport was probed with respect to band filling phenomena by supplying various concentrations of free carriers through remote doping in the GaAs barriers. Thus, the effect of changing the relative position of the Fermi level can be determined. With this background, we have performed detailed studies of the mechanisms of conductance in a system of quantum dot chains as a function of temperature and remote doping level. We have developed a 1D hopping model in order to characterize the transport in this system. In this way, we have demonstrated that the behavior of the conductance is complex due to the availability of states of different dimensionalities. We have found that the presence of 0D states plays a key role in the anisotropic behavior of the conductance in this system and compared the experimental response to a 1D hopping model. At low temperatures, the experimental response of all samples deviates from Mott's law of conduction.

This proposal, to characterize the transport properties of semiconductor nanostructures, will continue in conjunction with experimental collaborations (both in transport characterization as in the synthesis and growth of these structures). We intend to develop methods for the characterization of the electro-optical transport phenomena as light sensitive photo-detectors and light emitting diodes, as well as low dimensional ballistic electron waveguides integrated with site-controlled quantum dots as state dependent information transmission and storage devices. The combination of both, a strong experimental and theoretical expertise of our partners, offered the possibility for a roadmap strategy starting from basic fundamental properties of quantum transport phenomena of these structures towards the realization and applications of nano-scaled devices. We are grateful that this thesis, the published, and still unpublished results relayed on the strong collaboration between experimental growth, electro-optical spectroscopy, and theoretical groups with an expertise on the fabrication and modeling of low dimensional structures and devices.

BIBLIOGRAPHY

[1] WANG, Zh. M. et al. Fabrication of (In,Ga)As quantum-dot chains on GaAs(100). *Applied Physics Letters*, v. 84, p. 1931, 2004.

[2] LEE, J. H. et al. Selective growth of InGaAs/GaAs quantum dot chains on pre-patterned GaAs(100). *Nanotechnology*, v. 17, p. 2275, 2006.

[3] CAROFF, P. et al. Controlled polytypic and twin-plane superlattices in III-V nanowires. *Nature Nanotechnology*, v. 4, p. 50, 2009.

[4] ALGRA, R. E. et al. Twinning superlattices in indium phosphide nanowires. *Nature*, v. 456, p. 369, 2008.

[5] MORALES, A. M.; LIEBER,C. M. A Laser Ablation Method for the Synthesis of Crystalline Semiconductor Nanowires. *Science*, v. 279, p. 208-211, 1998.

[6] DUAN, X.; LIEBER C. M. General Synthesis of Compound Semiconductor Nanowires. *Advanced Materials*, v. 12, p. 298-302, 2000.

[7] GUDIKSEN, M. S.; LIEBER, C. M. Diameter-selective synthesis of semiconductor nanowires. *Journal of the American Chemical Society*, v. 122, p. 8801-8802, 2000.

[8] BJORK, M. T. et al. One-dimensional Steeplechase for Electrons Realized. *Nano Letters*, v. 2, p. 87, 2002.

[9] LOPEZ-RICHARD, V. Markovian and Non-Markovian Light-Emission Channels in Strained Quantum Wires. *Nano Letters*, v. 9, p. 3129, 2009.

[10] DUAN, X. et al. Single-nanowire electrically driven lasers. *Nature*, v. 421, p. 241, 2003.

[11] NILSSON, H. A. et al. Nanowire-based multiple quantum dot memory. *Applied Physics Letters*, v. 89, p. 163101, 2006.

[12] DUAN, X. et al. Single-nanowire electrically driven lasers. *Nature*, v. 421, p. 241-245, 2003.

[13] GRAY, G. R. *Semiconductor Laser: Past, Present and Future*, New York: American Intitute of Physics, 1995.

[14] DEBRAY, P. et al. All-electric quantum point contact spin-polarizer. *Nature Nanotechnology*, v. 4, p. 759, 2009.

[15] BRÜNE, C. et al. Evidence for the ballistic intrinsic spin Hall effect in HgTe nanostructures. *Nature Physics*, v. 6, p. 448, 2010.

[16] CHEN, T.-M. et al. All-Electrical Injection and Detection of a Spin-Polarized Current Using 1D Conductors. *Physical Review Letters*, v. 109, p. 177202, 2012.

[17] BRUSHEIM, P. et al. Multiterminal multimode spin-dependent scattering matrix formalism: Electron and hole quantum spin transport in multiterminal junctions. *Physical Review B*, v. 78, p. 085301, 2008.

[18] AHARONOY, A. et al. Filtering and analyzing mobile qubit information via Rashba-Dresselhaus-Aharonov-Bohm interferometers. *Physical Review B*, v. 84, p. 035323, 2011.

[19] NADJ-PERGE, S. et al. Spin-orbit qubit in a semiconductor nanowire. *Nature*, v. 468, p. 1084, 2010.

[20] VILLEGAS-LELOVSKY, L. et al. Spin polarization in quantum wires: Influence of Dresselhaus spin-orbit interaction and cross-section effects. *Physical Review B*, v. 79, p. 155306, 2009.

[21] STILES, M. D.; HAMANN, D. R. Ballistic electron transmission through interfaces. *Physical Review B*, v. 38, p. 2021, 2008.

[22] OREG, Y.; RAFAEL, G.; VON OPPEN, F. Helical Liquids and Majorana Bound States in Quantum Wires. *Applied Physics Letters*, v. 105, p. 177002, 2010.

[23] STANESCEUT, T. D.; LUTCHYN, R. M.; DAS SARMA S. Dimensional crossover in spin-orbit-coupled semiconductor nanowires with induced superconducting pairing. *Physical Review B*, v. 87, p. 094518, 2013.

[24] MOURICK, V. et al. Signatures of Majorana Fermions in Hybrid Superconductor-Semiconductor Nanowire Devices. *Science*, v. 336, p. 1003, 2012.

[25] ROKHINSON, L. P.; LIU, X.; FURDYNA, J. K. The fractional a.c. Josephson effect in a semiconductor-superconductor nanowire as a signature of Majorana particles. *Nature Physics*, v. 8, p. 795, 2012.

[26] GONZÁLES, J. C. et al. Structural and Optical Characterization of Strained Free-Standing InP Nanowires. *Journal of Nanoscience and Nanotechnology*, v. 6, p. 2182, 2006.

[27] SOUSA-DIAS, M. R. *Estudo de efeitos quânticos nas propriedades eletrônicas de nanoffios semicondutores*. 2010. MSc thesis - Departamento de Física, Universidade Federal de São Carlos.

[28] SHOUBERT, E. F. *Quantum Mechanics Applied to Semicondutor Device*.

[29] LANDAUER, R. Conductance from transmission: common sense points. *Physica Scripta* v. T42, p. 110, 1992.

[30] DATTA, S. *Transport in Mesoscopic Systems*, Cambridge: Cambridge University Press, 1995.

[31] ESAKI, L. New Phenomenon in Narrow Germanium p-n Junctions. *Physical Review*, v. 109, p. 603, 1958.

[32] MILLER, A.; ABRAHAMS, E. Impurity Conduction at Low Concentrations. *Physical Review*, v. 120, p. 745, 1960.

[33] BUCHER, P. N. *Linear and Nonlinear Electronic Transport in Solids*, edited by J. T. Devreese and V. E. Van Doren, New York: Plenum, 1976, p. 341–381.

[34] SHKLOVSKII, B. I.; EFROS, A. L. *Electronic Properties of Doped Semiconductors* 45 (Springer Series in Solid-State Science 45), Springer-Verlag, 1984.

[35] PASVEER, W. F.; BOBBERT, P. A.; MICHELS, M. A. Temperature and field dependence of the mobility in 1D for a Gaussian density of states. *Physica Status Solidi (C)*, v. 1, p. 164, 2003.

[36] PASCHOAL JR., W. et al. Hopping Conduction in Mn Ion-Implanted GaAs Nanowires. *Nano Letters*, v. 12, p. 4838, 2012.

[37] MORI, N.; MOMOSE, H.; HAMAGUCHI, C. Magnetophonon resonances in quantum wires. *Physical Review B*, v. 45, p. 4536, 1992.

[38] SONE, J. Electron transport in quantum wires and its device applications. *Semiconductor Science and Technology*, v. 7, p. B210, 1992.

[39] HUANG, D.; GUMBS, G. Comparison of inelastic and quasielastic scattering effects on nonlinear electron transport in quantum wires. *Journal of Applied Physics*, v. 107, p. 103710, 2010.

[40] FANG, T. et al. Mobility in semiconducting graphene nanoribbons: Phonon, impurity, and edge roughness scattering. *Physical Review B*, v. 78, p. 205403, 2008.

[41] HAUSER, M. et al. Investigation of the mobility and the drift velocity in a one-dimensional quantum wire. *Semiconductor Science and Technology*, v. 9, p. 951, 1994.

[42] TSETSERE, M.; TRIBERIS, G. P. Mobility in V-shaped quantum wires due to interface roughness and alloy scattering. *Physical Review B*, v. 69, p. 075313, 2004.

[43] LYO, S. K.; HUANG, D. Multisublevel magnetoquantum conductance in single and coupled double quantum wires. *Physical Review B*, v. 64, p. 115320, 2001.

[44] MURPHY-ARMANDO, F.; FAGAS, G.; GREER, J. C. Deformation Potentials and Electron-Phonon Coupling in Silicon Nanowires. *Nano Letters*, v. 10, p. 869-873, 2010.

[45] LOPEZ, V. et al. Magnetoresonant Raman scattering in zinc-blende-type semiconductors: Electron-phonon interaction mediated by a deformation potential. *Physical Review B*, v. 56, p. 15691, 1997.

[46] DEL ALAMO, J. A.; EUGSTER, C.C. Quantum Field-Effect Directional Coupler. *Applied Physics Letters*, v. 56, p. 78, 1990.

[47] EUGSTER, C. C. et al. Split-Gate Dual Electron Waveguide Device. *Applied Physics Letters*, v. 60, p. 642, 1992.

[48] BERTONI, A. et al. Quantum Logic Gates based on Coherent Electron Transport in Quantum Wires. *Physical Review Letters*, v. 84, p. 5912, 2000.

[49] DATTA, S.; DAS, B. Electronic analog of the electro-optic modulator. *Applied Physics Letters*, v. 56, p. 665, 1990.

[50] AUSLAENDER, O. M. et al. Tunneling Spectroscopy of the Elementary Excitations in a One-Dimensional Wire. *Science*, v. 295, p. 825, 2002.

[51] AUSLAENDER, O. M. et al. Spin-Charge Separation and Localization in One Dimension. *Science*, v. 308, p. 88, 2005.

[52] QUAY, C. H. L. et al. Observation of a one-dimensional spin-orbit gap in a quantum wire. *Nature Physics*, v. 6, p. 336, 2010.

[53] EGUES, J. C.; BURKARD, G.; LOSS, D. Datta-Das transistor with enhanced spin control. *Applied Physics Letters*, v. 82, p. 2658, 2003.

[54] ZHANG, L.; BRUSHEIN, P.; XU, H. Q. Multimode electron transport through quantum waveguides with spin-orbit interaction modulation: Applications of the scattering matrix formalism. *Physical Review B*, v. 72, p. 045347, 2005.

[55] ABAZOV, V. M. et al. The upgraded DO detector. *Nuclear Instruments and Methods in Physics Research Section A*, v. 565, p. 463, 2006.

[56] ANDEEN, T. et al. The D0 experiment's integrated luminosity for Tevatron Run IIa, *FERMILAB-TM-2365*, 2007.

[57] YAO, W. M. et al. Review of Particle Physics. *Journal of Physics G*, v. 33, p. 1, 2006.

[58] BRUN, R.; CARMINATI, F.; GIANI, S. GEANT Detector Description and Simulation Tool, *CERN Program Library Long Writeup W5013*, 1994.

[59] SJÖSTRAND, T. et al. High-energy-physics event generation with Pythia 6.1. *Computer Physics Communications*, v. 135, p. 238, 2001.

[60] PUMPLIN, J. et al. New Generation of Parton Distributions with Uncertainties from Global QCD Analysis. *Journal of High Energy Physics*, v. 0207, p. 012, 2002;

D. Stump, et al., Inclusive jet production, parton distributions, and the search for new physics. *Journal of High Energy Physics*, v. 0310, p. 046, 2003.

[61] JUNK, T. Confidence level computation for combining searches with small statistics. *Nuclear Instruments and Methods in Physics Research Section A*, v. 434, p. 435, 1999.

[62] BERTRAM, I. et al. A Recipe for the Construction of Confidence Limits, *FERMILAB-TM-2104*, 2000.

[63] IKONIĆ, Z.; SRIVASTAVA, G. P.; INKSON, J. C. Electronic structure of twinning superlattices. *Surface Science*, v. 307-309, p. 880, 1994.

[64] IKONIĆ, Z.; SRIVASTAVA, G. P.; INKSON, J. C. Electronic properties of twin boundaries and twinning superlattices in diamond-type and zinc-blende-type semiconductors. *Physical Review B*, v. 48, p. 17181, 1993.

[65] MAZUR, Yu. I. et al. InGaAs/GaAs three-dimensionally-ordered array of quantum dots. *Applied Physics Letters*, v. 83, p. 987, 2003.

[66] WANG, Zh. M. et al. One-dimensional postwetting layer in InGaAs/GaAs(100) quantum-dot chains. *Journal of Applied Physics*, v. 99, p. 033705, 2006.

[67] CESAR, D. F. et al. Carrier transfer in the optical recombination of quantum dots. *Physical Review B*, v. 83, p. 195307, 2011.

[68] HICKS, L. D.; DRESSELHAUS, M. S. Thermoelectric figure of merit of a one-dimensional conductor. *Physical Review B*, v. 47, p. 16631, 1993.

[69] BASTARD, G. *Wave Mechanics Applied to Semicondutor Heterostructures*, Les éditions de Physique, 1991.

[70] DATTA, S. *Modular Series on Solid States Devices (Quantum Phenomena): Volume VIII*, 1989.

[71] WINKLER, R. *Springer Tracts in modern Physics (Spin-orbit Coupling Effects in two-Dimensional Electron and Hole Systems): Volume 191*, 2003.

[72] LUTTINGER, J. M. Quantum Theory of Cyclotron Resonance in Semiconductors: General Theory. *Physical Review*, v. 102, p. 1030, 1956.

[73] LÖWDIN, Per-Olov. A Note on the Quantum-Mechanical Perturbation Theory. *Journal of Chemical Physics*, v. 19, p. 1396, 1951.

[74] LOPEZ-RICHARD, V. *Magneto-Optical Properties of Zinc-Blende Type Semiconductors and Semiconductor-Nanostructures*. 2001. PhD Thesis - Departamento de Física, Universidade Federal de São Carlos.

[75] BIMBERG, D. Free excitons in InP in high magnetic fields. *Physica B+C*, V. 89, p. 139, 1977.

[76] POLLAK, F. H; CARDONA, M. Piezo-Electroreflectance in Ge, GaAs, and Si. *Physical Review*, v. 172, p. 816, 1968.

[77] Landolt-Börnstein Comprehensive Index, ed. O. Madelung and W. Martienssen, Berlin: Springer, 1996.

[78] NOLTE, D. D.; WALUKIEWICZ, W.; HALLER, E. E. Band-edge hydrostatic deformation potentials in III-V semiconductors. *Physical Review Letters*, v. 59, p. 501, 1987.

[79] STOTTER, A. C. *Efecto Raman resonante con Campos Magnéticos Intensos en Heteroestructuras Semiconductoras*. 1993. PhD Thesis - Departamento de Física Aplicada, Universidad de Valencia.

[80] YU, P. Y.; CARDONA, M. *Fundamentals of Semiconductors: Physics and Materials Properties*, Springer-Verlag, 1996.

[81] CANTARERO, A.; TRALLERO-GINGER, C.; CARDONA, M. Excitons in one-phonon resonant Raman scattering: Deformation-potential interaction. *Physical Review B*, v. 39, p. 8388, 1989.

[82] MITIN, V. V.; KOCHELAP, V. A.; STROSCIO, M. A. *Quantum Heterostructures: microelectronics and optoelectronics*, Cambridge: Cambrigde University Press, 1999.

[83] TSU, R.; ESAKI, L. Tunneling in a finite superlattice. *Applied Physics Letters*, v. 22, p. 11, 1973.

[84] VILLEGAS-LELOVSKY, L. et al. Spin polarization in quantum wires: Influence of Dresselhaus spin-orbit interaction and cross-section effects. *Physical Review B*, v. 79, p. 155306, 2009.

[85] MAHAN, G. G. *Many-Particle Physics*, 3rd ed., New York: Kluwer, 2000.

[86] LOPEZ-RICHARD, V. et al. Resonant Raman scattering in a magnetic field assisted by Fröhlich interaction in zinc-blende-type semiconductors. *Physical Review B*, v. 58, p. 16136, 1998.

[87] BRANICIO, P. S.; RINO, J. P.; SHIMOJO, F. High-pressure phases of InP: An ab initio and molecular-dynamics study. *Applied Physics Letters*, v. 88, 161919, 2006.

[88] BRANICIO, P. S. et al. Interaction potential for indium phosphide: a molecular dynamics and first-principles study of the elastic constants, generalized stacking fault and surface energies. *Journal of Physics: Condensed Matter*, v. 21, p. 095002, 2009.

[89] RINO, J. P.; BRANICIO, P. S. You have full text access to this contentStructural phase transformations in InP under pressure: A molecular-dynamics study. *Physica Status Solidi (B)*, v. 244, p. 239 2007.

[90] BRANICIO, P. S.; RINO, J. P. Vibrational properties of InP under pressure: a molecular-dynamics study. *Physica Status Solidi (B)*, v. 244, p. 331, 2007.

[91] TSUZUKI, H. et al. Tailoring Electronic Transparency of Twin-Plane 1D Superlattices. *ACS Nano*, v. 5, p. 5519, 2011.

[92] RINO, J. P. et al. Structural and dynamical correlations in Ag2Se: A molecular dynamics study of superionic and molten phases. *Journal of Chemical Physics*, v. 89, p. 7542, 1988.

[93] BORCHERDS, P. H. et al. Phonon dispersion curves in indium phosphide. *Journal of Physics C: Solid State Physics*, v. 8, p. 2022, 1975.

[94] BLIZ, H.; KRESS, W. *Phonon dispersion relations in insulators 107* (Springer series in solid-state sciences), Springer-Verlag, 1979.

[95] RASHBA, E. Svoistva poluprovodnikov s petlei ekstremumov. I. Tsiklotronnyi i kombinirovannyi rezonans v magnitnom pole, perpendikulyarnom ploskosti petli. *Fiz. Tverd. Tela (Leningrad)*, v. 2, p. 1224, 1960; [Properties of semiconductors with an extremum loop .1. Cyclotron and combinational resonance in a magnetic field perpendicular to the plane of the loop. *Soviet physics, Solid state* v. 2, p. 1109, 1960].

[96] ZHAI, F.; XU, H. Q. Symmetry of Spin Transport in Two-Terminal Waveguides with a Spin-Orbital Interaction and Magnetic Field Modulations. *Physical Review Letters*, v. 94, p. 246601, 2005.

[97] PFEIFFER, L. N. et al. Ballistic hole transport in a quantum wire. *Applied Physics Letters*, v. 87, p. 073111, 2005.

[98] BIELEJEC, E. et al. Tunneling and nonlinear transport in a vertically coupled GaAs/AlGaAs double quantum wire system. *Applied Physics Letters*, v. 86, p. 083101, 2005.

[99] BOESE, D. et al. Mesoscopic effects in tunneling between parallel quantum wires. *Physical Review B*, v. 64, p. 085315, 2001.

[100] ZÜLICKE, U.; SCHROLL, C. Interface Conductance of Ballistic Ferromagnetic-Metal-2DEG Hybrid Systems with Rashba Spin-Orbit Coupling. *Physical Review Letters*, v. 88, p. 029701 2002.

[101] NIKOLIĆ, B. K.; SOUMA, S. Decoherence of transported spin in multichannel spin-orbit-coupled spintronic devices: Scattering approach to spin-density matrix from the ballistic to the localized regime. *Physical Review B*, v. 71, p. 195328, 2005.

[102] BLAZEY, G. C. et al. Run II Jet Physics, *Proceedings of the Run II QCD and Weak Boson Physics Workshop*, edited by U. Baur, R.K. Ellis and D. Zeppenfeld, *Fermilab-Pub-00/297*, 2000.

[103] CESAR, D. F. et al. Contrasting LH-HH subband splitting of strained quantum wells grown along [001] and [113] directions. *Physical Review B*, v. 81, p. 233301, 2010.

[104] SCHMIDT, T. M. et al. Stability and electronic confinement of free-standing InP nanowires: Ab initio calculations. *Physical Review B*, v. 72, p. 193404, 2005.

[105] MIWA, R. H.; SCHMIDT, T. M.; FAZZIO, A. EL2-like defects in InP nanowires: An ab initio total energy investigation. *Physical Review B*, v. 75, p. 165324, 2007.

[106] SCHMIDT, T. M. Hydrogen and oxygen on InP nanowire surfaces. *Applied Physics Letters*, v. 89, p. 123117, 2006.

[107] AKIYAMA, T.; NAKAMURA, K.; ITO, T. Structural stability and electronic structures of InP nanowires: Role of surface dangling bonds on nanowire facets. *Physical Review B*, v. 73, p. 235308, 2006.

[108] SANO, K. et al. A Monte-Carlo simulation study of twinning formation in InP nanowires. *Journal of Crystal Growth*, v. 301-302, p. 862-865, 2007.

[109] PERSSON, M. P.; XU, H. Q. Electronic structure of [100]-oriented free-standing InAs and InP nanowires with square and rectangular cross sections. *Physical Review B*, v. 73, p. 125346, 2006.

[110] AKIYAMA, T. et al. Band Alignment Tuning in Twin-Plane Superlattices of Semiconductor Nanowires. *Nano Letters*, v. 10, p. 4614, 2010.

[111] LI, D.; WANG, Z.; GAO, F. First-principles study of the electronic properties of wurtzite, zinc-blende, and twinned InP nanowires.*Nanotechnology*, v. 21, p. 505709, 2010.

[112] BITTENCOURT, A. C.; COHEN, A. M.; MARQUES, G. E. Strain-induced enhancement of resonant current of holes in multilayered heterostructures. *Physical Review B*, v. 57, p. 4525, 1998.

[113] EBBSJÖ, I. et al. Topology of amorphous gallium arsenide on intermediate length scales: A molecular dynamics study. *Journal of Applied Physics*, v. 87, p. 7708, 2000.

[114] BRANICIO, P. S.; SROLOVITZ, D. J. Local stress calculation in simulations of multicomponent systems. *Journal of Computational Physics*, v. 228, p. 8467, 2009.

[115] NYE, F. *Physical properties of crystals*. Clarendon, Oxford, 1985.

[116] HINCKLEY, J. M.; SINGH, J. Influence of substrate composition and crystallo-graphic orientation on the band structure of pseudomorphic Si-Ge alloy films. *Physical Review B*, v. 42, p. 3546, 1990.

[117] TSU, R. *Superllatice to Nanoelectronics*, Elsevier: Oxford, 2005.

[118] JANSSENS, K. L.; PARTOENS, B.; PEETERS, F. M. Effect of strain on the magnetoexciton ground state in $InP/Ga_xIn_{1-x}P$ quantum disks. *Physical Review B*, v. 67, p. 235325, 2003.

[119] PIKUS, G. E.; BIR, G. L. *Soviet Physics Solid-state*, v. 1, p. 136, 1959.

[120] FISHMAN, G. Hole subbands in strained quantum-well semiconductors in [hhk] directions. *Physical Review B*, v. 52, p. 11132, 1995.

[121] VURGAFTMAN, I.; MEYER, J. R.; RAM-MOHAN, L. R. Band parameters for III-V compound semiconductors and their alloys. *Journal of Applied Physics*, v. 89, p. 5815, 2001.

[122] KUNETS, Vas. P. et al. Isotropic Hall effect and "freeze-in" of carriers in the InGaAs self-assembled quantum wires. *Journal of Applied Physics*, v. 110, p. 083714, 2011.

[123] KUNETS, Vas. P. et al. Electron transport in quantum dot chains: Dimensionality effects and hopping conductance. *Journal of Applied Physics*, v. 113, p. 183709, 2013.

[124] LOOK, D. C. *Electrical characterization of GaAs Materials and Devices*, New York: John Wiley and Sons, 1989.

[125] MOTT, N. Conduction in glasses containing transition metal ions. *Journal of Non-Crystalline Solids*, v. 1, p. 1, 1968.

[126] TSIGANKOV, D. N.; EFROS, A. L. Variable Range Hopping in Two-Dimensional Systems of Interacting Electrons. *Physical Review Letters*, v. 88, p. 176602, 2002.

[127] VAN KEULS, F. W. et al. Screening of the Coulomb interaction in two-dimensional variable-range hopping. *Physical Review B*, v. 56, p. 1161, 1997.

[128] YAKIMOV, A. I. et al. Phononless hopping conduction in two-dimensional layers of quantum dots. *Journal of Experimental and Theoretical Physics Letters*, v. 77, p. 376, 2003.

[129] ZABRODSKII, A. G.; ZINOV'EVA, K. N. *Soviet Physics - Journal of Experimental and Theoretical Physics*, v. 59, p. 425, 1984.

[130] ZAITSEV-ZOTOV, S. V. et al. Luttinger-liquid-like transport in long InSb nanowires, *Journal of Physics: Condensed Matter*, v. 12, p. 303, 2000.

[131] SLOT, E. et al. One-Dimensional Conduction in Charge-Density-Wave Nanowires, *Physical Review Letters*, v. 93, p. 176602, 2004.

[132] VENKATARAMAN, L.; HONG, Y. S.; KIM, P. Electron Transport in a Multi-channel One-Dimensional Conductor: Molybdenum Selenide Nanowires, *Physical Review Letters*, v. 96, p. 076601, 2006.

[133] ZHOU, Z. et al. One-dimensional electron transport in Cu-tetracyanoquinodimethane organic nanowires, *Applied Physics Letters*, v. 90, p. 193115, 2007.